TUNABLE ABSORPTIVE BANDSTOP-TO-ALL-PASS FILTER SYNTHESIS,

CONTROL, APPLICATIONS, AND OPTIMIZATIONS

A Dissertation

Submitted to the Faculty

of

Purdue University

by

Wei Yang

In Partial Fulfillment of the

Requirements for the Degree

of

Doctor of Philosophy

August 2019

Purdue University

West Lafayette, Indiana

THE PURDUE UNIVERSITY GRADUATE SCHOOL
STATEMENT OF DISSERTATION APPROVAL

Dr. Dimitrios Peroulis, Co-Chair

    School of Electrical and Computer Engineering

Dr. Dimitra Psychogiou, Co-Chair

    School of Electrical and Computer Engineering

Dr. Jeffrey F. Rhoads

    School of Mechanical Engineering

Dr. Sunil A. Bhave

    School of Electrical and Computer Engineering

Approved by:

    Dr. Dimitrios Peroulis

        Head of the School Graduate Program

TABLE OF CONTENTS

LIST OF TABLES

LIST OF FIGURES

Figure   Page

ABSTRACT

Yang, Wei PhD, Purdue University, August 2019. Tunable Absorptive Bandstop-to-All-Pass Filter Synthesis, Control, Applications, and Optimizations. Major Professors: Dimitrios Peroulis, Dimitra Psychogiou.

In this dissertation, the synthesis of the triplet absorptive topology is presented in detail. The coupling matrix of this topology is derived. The synthesis theory extends to arbitrary phase of the transmission line used in the topology. A new FSL that yields the state-of-the-art performance is proposed. It employs the triplet absorptive filter topology, which enables absorptive response in a wider tuning range, to achieve high isolation (70 dB) everywhere in its octave tuning range. This was not possible with any existing FSLs. This triplet filter topology also gives bandstop-to-all-pass response, which enables controlled attenuation, or variable-attenuation control. The filter is implemented in high-Q evanescent-mode cavity technology, which yields low insertion loss in all-pass response. The proposed FSL is integrated with feedback control loops to enable in-field operations. For one step further, the FSL system is redesigned for optimization of robustness and reliability without compromising the state-of-the-art RF performance.

1. INTRODUCTION

1.1 Background

Radio frequency (RF) spectrum, which ranges from 3 KHz to 300 GHz, is divided into bands and channels to accommodate various commercial and military communications [1]. As the demand in wireless communication overgrows, the RF spectrum gets crowded. Filters are utilized to separate desired signal information from adjacent bands and transceivers. Bandpass filters, which are designed to minimize the signal attenuation in the band of interest and to achieve the desired attenuation in other bands, are the traditional solution. A bandpass-filter-based receiver architecture can result in significant insertion loss. For a given resonator quality-factor (Q-factor), there is a trade-off between bandwidth, selectivity, and insertion loss [2]. This means the greater the protection, the higher the in-band insertion loss. Therefore, filters remain a design bottleneck in 4G-LTE and upcoming 5G communication systems.

While the common types of bandpass filters meet the requirement for most applications, they suffer from some disadvantages in some situations. A signal interferer can be particularly strong, and the out-of-band attenuation of the bandpass filters are not significant enough, or that signal interferer is very close to the passband, and the selectivity of the bandpass filters are not good enough. In both cases, a bandpass filter will not be as efficient as one or more bandstop filters, which is designed against the unwanted frequencies [3].

A software-defined radio (SDR) or cognitive radio (CR) system that can observe the RF environment and select frequency bands in real time will not need fear-based bandpass filtering [4]. The SDR and CR are proposed based on the fact that while most of the cellular bands are crowded, their nearby spectrum is seldom used. The usage within the cellular bands can also be further optimized with the help of SDR

and CR. In the situation that interference presents and becomes a concern, bandstop filtering can be used to attenuate it. The usage of bandstop filters in the spectrum aware systems rather than bandpass filters minimize the in-band insertion loss and maximize the attenuation of unwanted signals. Lower insertion loss also corresponds to a lower noise figure.

In satellite and other wide-band communications, limiters are widely utilized to protect the front-end circuitry from interfering signals of excessive power [5]. A high-power interfering signal may either saturate the receiver thus compromising its sensitivity, or result in permanent damage of sensitive devices. An ideal limiter can be characterized as a linear device below a power threshold level, and a constant output device above this threshold, as illustrated in Fig. 1.1. The attenuation level increases in direct proportion to the input power level above the threshold.
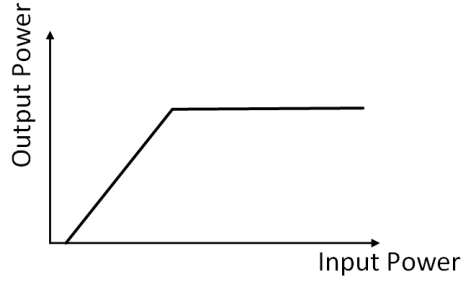
Fig. 1.1. Ideal characteristic of a limiter [5].

One type of limiters is based on non-linear effects in ferromagnetic material [6]. This type of limiters can have low threshold levels (-10 dBm) with the coincidence mode of limiting. Low insertion of less than 1 dB can be achieved with thin linewidth material such as single-crystal yttrium iron garnet (YIG) or lithium ferrite. An attenuation of more than 20 dB is reported. Another type of limiters is solid-state limiters based on PIN diodes, FETs, etc [7–15]. These devices are implemented in shunt with a transmission line. The diode becomes a short circuit with high-power signals present, and act as a capacitance otherwise.

1.2   Review of Absorptive Bandstop Filters

Bandstop filters are proved to be useful in SDR, CR, satellite and other wide-band systems. Also, they are necessary for extreme RF environment. A conventional bandstop filter rejects and reflects the signal at the desired center frequency. However, the attenuation and selectivity are limited by the resonator Q-factor. Since Q-factor is proportional to the resonator size, the desire for large attenuation and miniaturization cannot be achieved together. Fig. 1.2 plots the simulated maximum attenuation of a second-order quarter-wavelength bandstop filter of Butterworth type versus resonator Q-factor. To achieve a 40-dB attenuation, Q-factor needs to be larger than 300, which is challenging for several common filter technologies including microstrip and stripline filters.
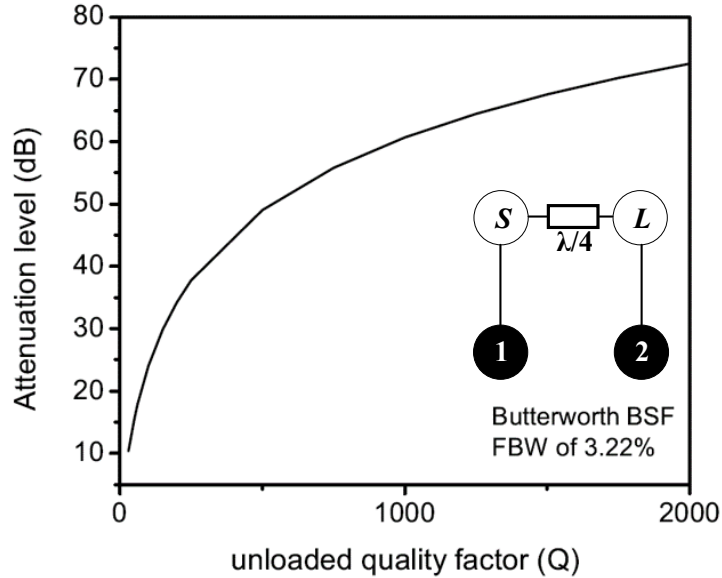
Fig. 1.2. Simulated attenuation of a second-order quarter-wavelength bandstop filter of Butterworth type versus resonator Q-factor [16]. The introduction of coupling diagram is in Appendix A.

Absorptive concepts were first developed in 1931 by Hendrik Bode from Nokia Bell Labs, which provides a way to break the trade-off between size and performance

4
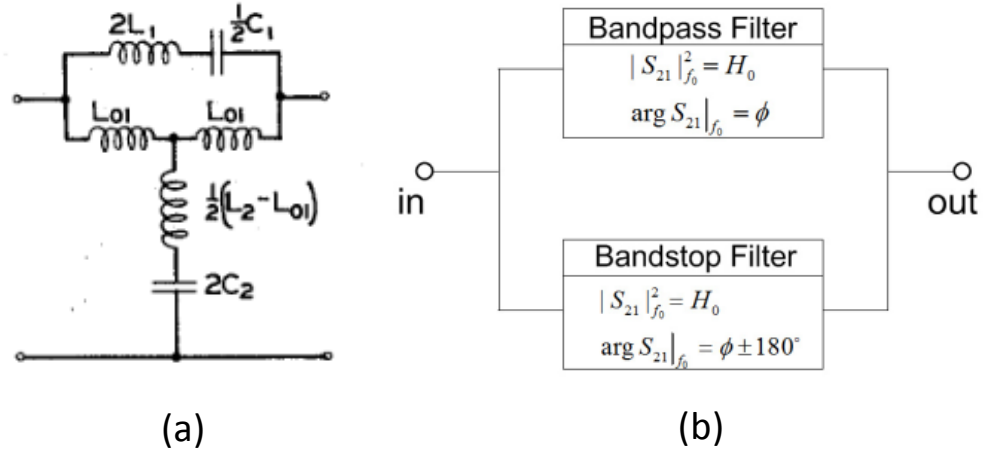
Fig. 1.3. (a) Patented lumped-element bridge-T notch filter by Bode and (b) Concept of enhanced-Q notch filter [19].

[17,18]. D. R. Jachowski summarized and developed the absorptive filter theories and typologies systematically in 2004 [19,20]. As shown in Fig. 1.3, the input signal is split between the bandpass branch and the bandstop branch. If at a certain frequency, the two signals have the same magnitude but an odd multiple of 180° out of phase with each other, the two will cancel, and infinite attenuation will result. This means that the attenuation depends on phase matching, not on the Q-factor anymore. Based on this concept, several designs are proposed.

1.2.1   Design I

The most studied design is shown in Fig. 1.4. This design comprises a phase shift in the upper branch, and a second-order bandpass configuration in the lower branch. The coupling diagram is shown in Fig. 1.4(b).
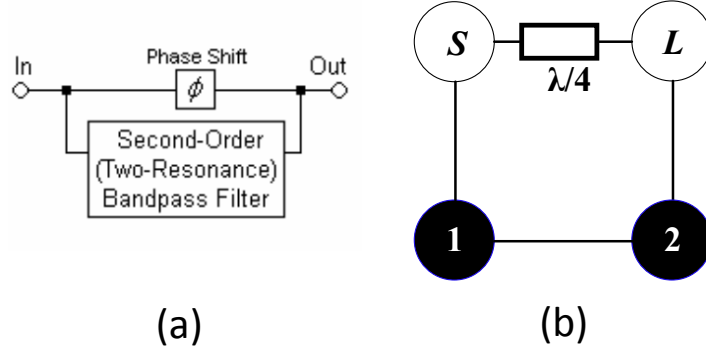
Fig. 1.4. (a) Concept of absorptive bandstop filter based on a single second-order bandpass filter and (b) Coupling diagram of the two-pole absorptive bandstop filter [20].

Two types of absorptive response, namely fully absorptive and quasi-absorptive can be achieved. The full-absorptive response is defined that the signal power at the center frequency is fully absorbed and dissipated in the lossy resonators. The quasi-absorptive response is defined that the signal power at the center frequency is partially absorbed/dissipated and partially reflected. The coupling matrix to achieve fully-absorptive response is given by

$$
M = \begin{bmatrix} 0 & M_{S,1} & 0 & M_{S,L} \\ M_{S,1} & -jM_{1,1} & M_{1,2} & 0 \\ 0 & M_{1,2} & -jM_{2,2} & M_{2,L} \\ M_{S,L} & 0 & M_{2,L} & 0 \end{bmatrix} \tag{1.1}
$$

where

$$
M_{ii} = \frac{1}{Q\Delta}. \tag{1.2}
$$

Q is the resonator Q-factor and Δ is the fractional bandwidth. The coupling matrix is explained in detail in Appendix B. For symmetry, $M_{S,1}=M_{2,L}$ and $M_{1,1}=M_{2,2}$. $M_{S,L} = 1$ for a quarter-wavelength inverter. The reflection and transmission coefficients for the low-pass prototype at the center frequency are given by

$$
S_{21} = \frac{2j(M_{1,2}M_{2,L}^2 - M_{1,2}^2 - M_{1,1})}{2M_{1,2}^2 - 2M_{1,2}M_{2,L}^2 + M_{2,L}^4 + 2M_{2,L}^2 M_{1,1} + 2M_{1,1}^2}, \tag{1.3}
$$
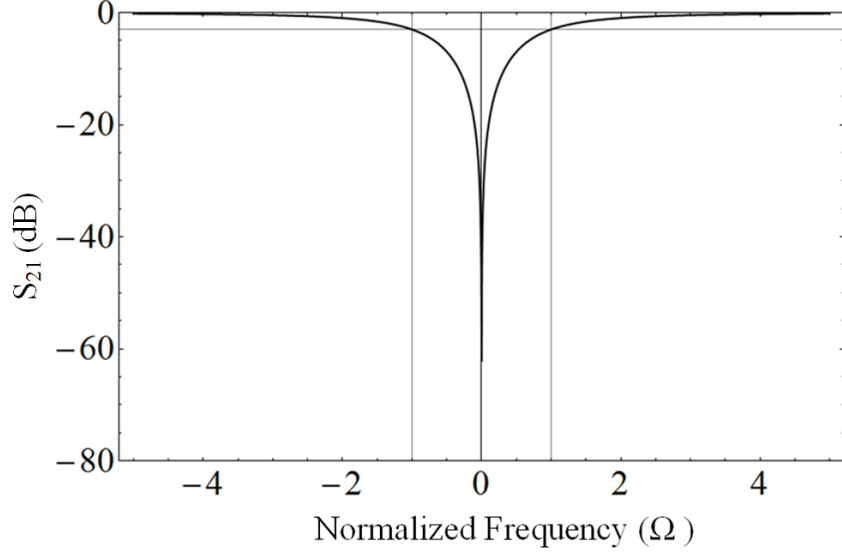
Fig. 1.5. Normalized fully-absorptive bandstop filter response.

and

$$S_{11} = \frac{-2M_{1,2}M_{2,L}^2 + M_{2,L}^4}{2M_{1,2}^2 - 2M_{1,2}M_{2,L}^2 + M_{2,L}^4 + 2M_{2,L}^2 M_{1,1} + 2M_{1,1}^2}. \tag{1.4}$$

An infinite attenuation at center frequency can be achieved when

$$M_{2,L} = \pm\sqrt{2M_{1,1}}, M_{1,2} = M_{1,1}. \tag{1.5}$$

The mathematical response is plotted in Fig. 1.5.

Table 1.1.
Demonstrations of Fully-Absorptive Bandstop Filters

Ref.	Tech.	Tuning Tech.	Tuning Range	Max. Attn. [dB]	Q-factor
[20]	Microstrip	Varactor	1.8−2.5 GHz	53	N/A
[21]	Lumped	Varactor	55−133 MHz	70	62
[22]	Lumped	SAW	418 MHz	62	10,000
[23]	Cavity	Piezo	3−6 GHz	60	N/A
[24]	Microstrip	Varactor	1.6−2.3 GHz	60	50

The fully-absorptive bandstop filters are demonstrated in several frequency bands and filter technologies [20–25]. Table. 1.1 summarized the literature. With a matched design, a more than 50-dB attenuation is easily achievable at the design center frequency. The return loss is less than 20 dB, which is good for some applications when reflections are not preferred.
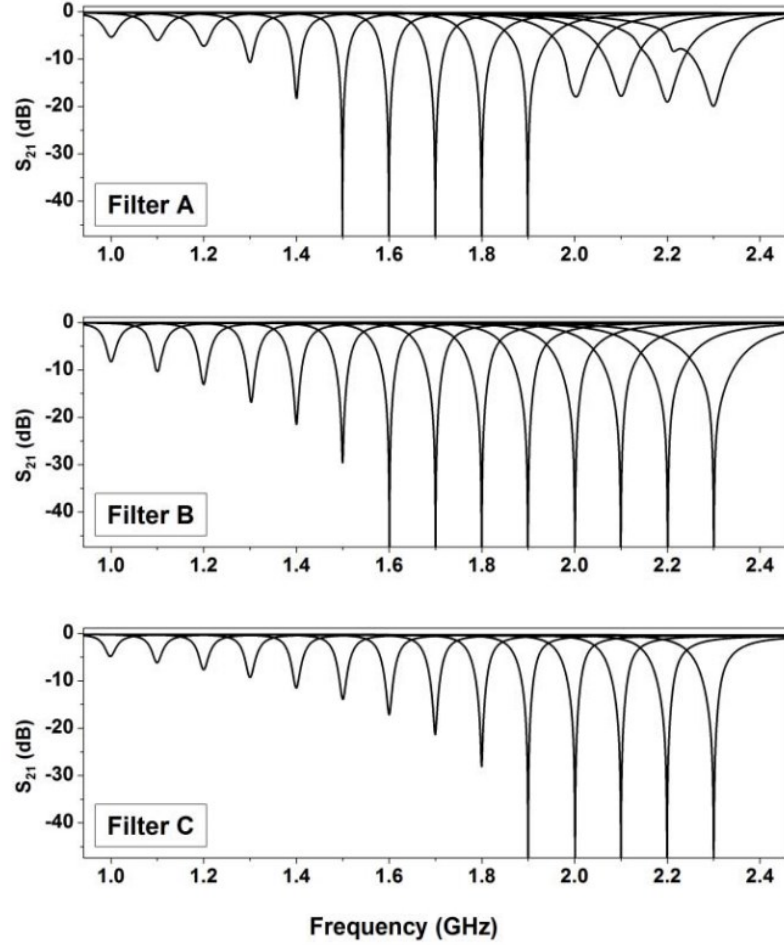
Fig. 1.6. Example measured response of the fully-absorptive bandstop filter response when tuned away from the design center frequency [24].

Several drawbacks for the fully-absorptive bandstop topology are identified. The bandwidth is $2/Q$, which depends on resonator Q-factor. The matched condition occurs when the transmission line as an impedance inverter is 90°. When tuning

away from design center frequency, it is not 90° anymore. The attenuation level decreases as shown in Fig. 1.6.

The coupling matrix to achieve quasi-absorptive response is given by

$$
M = \begin{bmatrix} 0 & M_{S,1} & 0 & M_{S,L} \\ M_{S,1} & M_{1,1} & M_{1,2} & 0 \\ 0 & M_{1,2} & -M_{1,1} & M_{2,L} \\ M_{S,L} & 0 & M_{2,L} & 0 \end{bmatrix} \tag{1.6}
$$

where $M_{1,1}$ is the resonator detuning away from the design center frequency. For symmetry, $M_{S,1}=M_{2,L}$ and $M_{1,1}=M_{2,2}$. $M_{S,L} = 1$ for a quarter-wavelength inverter. The transmission coefficients for the low-pass prototype at the center frequency are given by

$$
S_{21} = \frac{s^2 + M_{1,1}^2 + M_{1,2}^2 - M_{S,1}^2 M_{1,2}}{s^2 + M_{S,1}^2 s + 0.5 M_{S,1}^4 + M_{1,1}^2 + M_{1,2}^2 - M_{S,1}^2 M_{1,2}} \tag{1.7}
$$

An infinite attenuation at center frequency can be achieved when

$$
M_{S,1} = 1.189, M_{1,1} = M_{1,2} = \frac{M_{S,1}^2}{2}. \tag{1.8}
$$

The mathematical response is a Butterworth bandstop filter response shown in Fig. 1.7. The quasi-absorptive bandstop filters are demonstrated [25,26,28]. Table. 1.2 summarized the literature. The quasi-absorptive response looks similar to the second-order Butterworth bandstop response as the coupling coefficients are solved to match the ideal Butterworth response. Unlike fully-absorptive response, the bandwidth of quasi-absorptive response is not fixed, or not dependent on Q-factor.

The quasi-absorptive bandstop topology requires the same matching condition as the fully-absorptive topology, an inverter of 90°. When tuning away from design center frequency, it is not 90° any more. The attenuation level decreases as shown in Fig. 1.8.

To extend the range within tuning range where absorptive response forms, one method is to transform the topology into an equivalent one in Fig. 1.9(a). The two external couplings are implemented with magnetic and electrical couplings. The equivalent circuit, as shown in Fig. 1.9(b), generates excess degrees transmission line
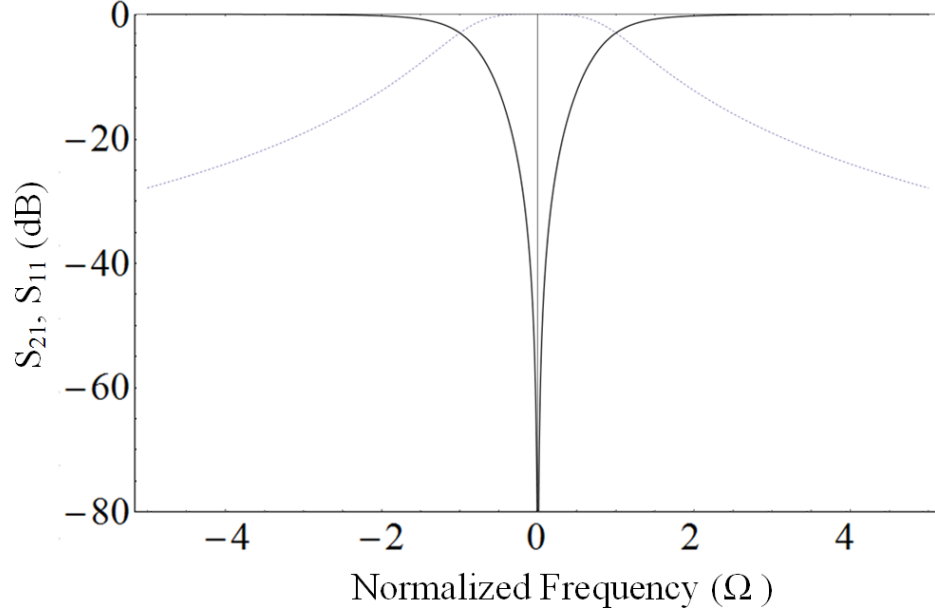
Fig. 1.7. Normalized quasi-absorptive bandstop filter response.

Table 1.2.
Demonstrations of Quasi-Absorptive Bandstop Filters

Ref.	Tech.	Tuning Tech.	Tuning Range	Max. Attn. [dB]	Q-factor
[25]	Cavity	Piezo	2.75−3.1 GHz	70	400
[26]	Cavity	MEMS	6.3−11.4 GHz	74	497
[27]	Silicon	MEMS	22−43 GHz	60	400
[28]	Silicon	MEMS	75−103 GHz	60	290

θ_1, which will compensate the degree variation of the transmission line θ_3 [29]. This way, an octave tuning range with the absorptive response can be achieved. The drawback of this design is that there are no equations to predict the behavior analytically. Also, this coupling compensation is only applicable to the cavity technologies.

It should be mentioned that this filter topology has been demonstrated in all the major tunable technologies. At frequency bands lower than 1 GHz, the filter
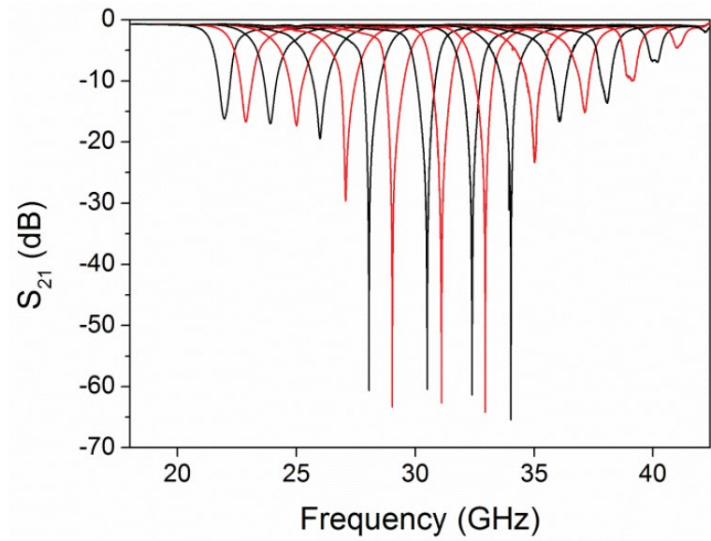
Fig. 1.8. Example measured response of the fully-absorptive bandstop filter response when tuned away from the design center frequency [27].
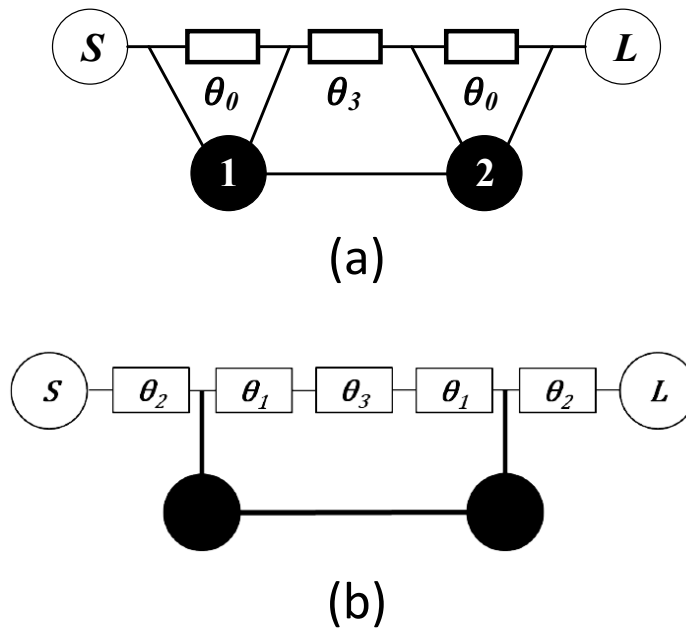
Fig. 1.9. Coupling diagrams of (a) deformed two-pole absorptive bandstop topology and (b) its equivalent circuit [29].

is implemented with lumped-element technology tuned by varactors. At frequency bands between 1 and 3 GHz, the filters are implemented with microstrip technology tuned by varactors. At frequency bands between 3 and 20 GHz, the filters are implemented with loaded cavity technology tuned by piezo-actuators or MEMS-actuators. At frequency bands between 20 and 100 GHz, the filters are implemented with silicon technology tuned by MEMS-actuators. The fabricated filters are shown in Fig. 1.10.
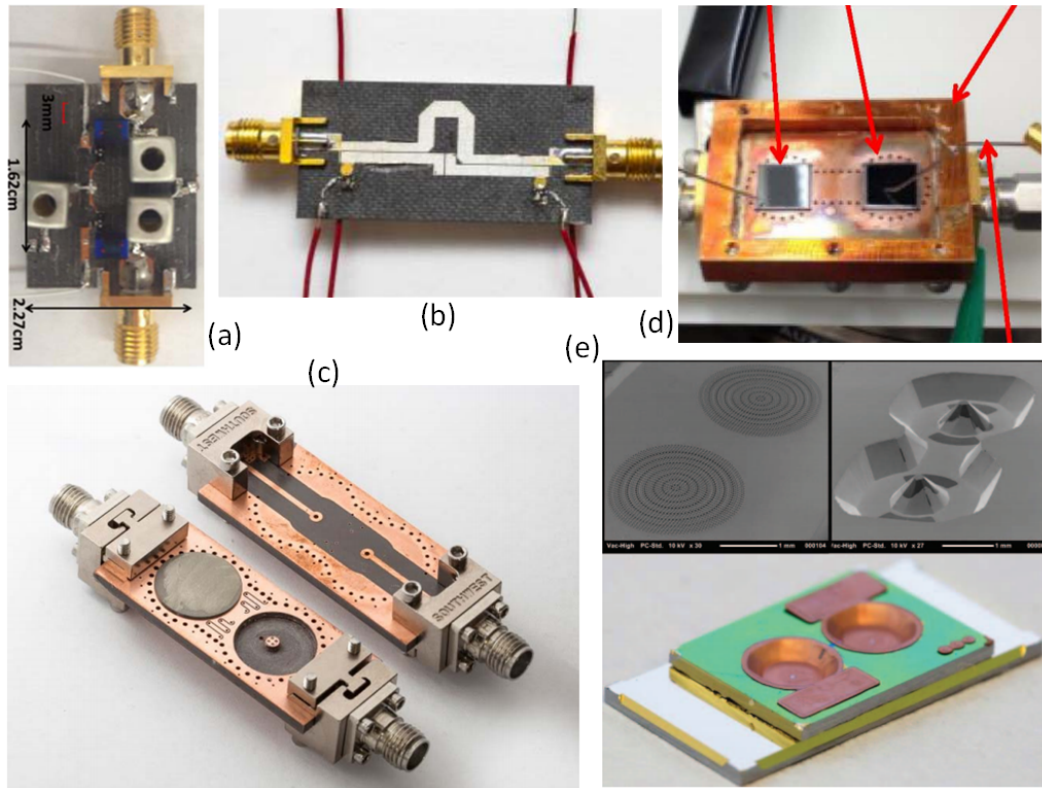
Fig. 1.10. Fabricated absorptive bandstop filters with (a) lumped-element technology tuned by varactors [21], (b) microstrip technology tuned by varactors [23], (c) loaded-cavity technology tuned by piezo-actuators [24], (d) loaded-cavity technology tuned by MEMS-actuators, and (e) silicon technology tuned by MEMS-actuators.

1.2.2 Design II

Another design, which was proposed at the same time is the triplet absorptive topology as shown in Fig. 1.11(a). This design comprises a bandpass in the upper branch and a bandstop with two quarter-wavelength inverters in the lower branch. The coupling diagram is shown in Fig. 1.11(b). This topology is demonstrated in microstrip technology as a static notch filter with fully-absorptive response [19], and as a tunable notch filter with quasi-absorptive response [30]. Even though a small tuning range is shown in [30], the potential of this topology to achieve an absorptive response in wide tuning range is promising and yet to investigate. The theory to synthesize non-90 degrees is not systematically derived. Furthermore, the coupling matrix, which is commonly used to quickly synthesize a topology to the desired center frequency and desired bandwidth is not available. This dissertation presents a detailed study of this topology, complete the theory for synthesis and coupling matrix, and demonstrates state-of-the-art RF performance.
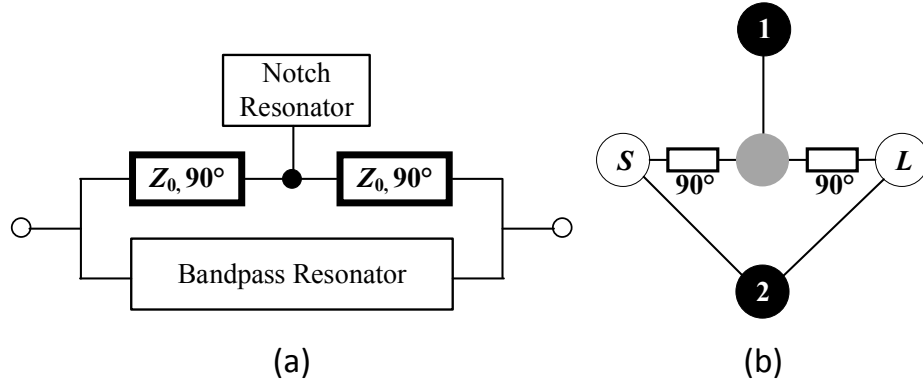
Fig. 1.11. (a) Concept of the absorptive bandstop filter based on a single second-order bandpass filter and (b) Coupling diagram of the two-pole absorptive bandstop filter [20].

1.3 Review of Frequency-Selective Limiters

The characteristic of limiters is a variation of attenuation with input power level. If two signals are applied, one smaller signal and one large signal above the limiting threshold, both the signals will be attenuated. Limiters protect the circuitry in the receiver but do not improve the dynamic range. What is worse is that small signals, which may be the desired ones, are attenuated. Frequency-selective limiters (FSLs), on the other hand, operate independently on each signal within the passband [5]. As long as the signals are separated a certain amount in frequency, those that are below limiting threshold are minimally affected. An ideal FSL has the following characteristics as shown in Fig. 1.12: 1) The small signals are not attenuated when saturating signals are present; 2) The saturated power output in the presence of N saturating signals equal to N times the threshold power output in the presence of a single frequency; 3) No harmonics are generated from multiple saturating signals. In
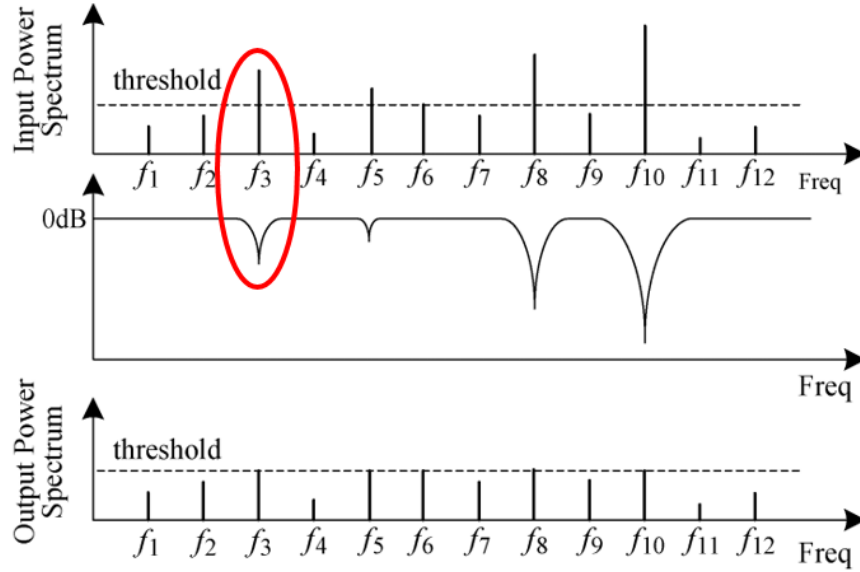
Fig. 1.12. The basic operation of a wide-band Frequency-selective limiter [48].

general two types of FSLs have been reported in the open literature: ferrite-based and diode-based. Significant research has focused on the former since Kotzebue's

discovery of nonlinear frequency-selective property in spin-wave limiters [36,37]. FSLs employing different technologies such as nuclear or electron magnetic resonance [38], magnetoelastic resonance (YIG, EUIG) [39–44], and paramagnetic [45] have been developed. These technologies result in FSLs with deep notches in the range of 40 dB for frequencies that range from base-band to X-band. On the other hand, high insertion losses of more than 10 dB have been reported. Furthermore, it is also hard to reduce or tune the power threshold level to less than 0 dBm. Ferrite-based FSLs also tend to be high-cost and bulky structures.

Diode-based FSLs have been implemented in parametric [46, 47] and resonant circuits [37,48–52]. This is a low-cost technology resulting in small-form-factor devices at 2 GHz [47–50, 52], and 20 GHz [51]. Attenuation level up to 35 dB has been reported. However, frequency tunability has not been reported. In [53], an FSL implemented by a six-channel bandpass filter is presented covering the frequency range from 1 to 1.3 GHz with tunable power threshold level from 16 to 33 dBm. Nevertheless, it is also hard to reduce and/or tune the power threshold level to less than 0 dBm due to the nature of the diodes.

The FSL in literature is mostly implemented with a bandstop limiter, which is a passive bandstop resonator loaded with a nonlinear semiconductor device, or a Schottky diode. The resonator is designed to have a narrow-band bandstop response at the desired limiting frequency. The diode adds a series of resistance to the resonator and changes the equivalent unloaded Q-factor. When the RF input power is low, and the voltage is below the thermal voltage of the diode, the diode presents a high impedance. The equivalent Q-factor is low, and the attenuation is small. When the RF input power is high, and the voltage is higher than the thermal voltage of the diode, the diode presents low impedance. The equivalent Q-factor is high, and a notch is formed. The basic circuit of a bandstop limiter is shown in Fig. 1.13. The bandstop limiter is a low-cost technology with small form factors. However, the attenuation level is limited by the on-state resistance of the diode. It is also hard to reduce and tune the power threshold level to less than 0 dBm due to the nature of the diodes.
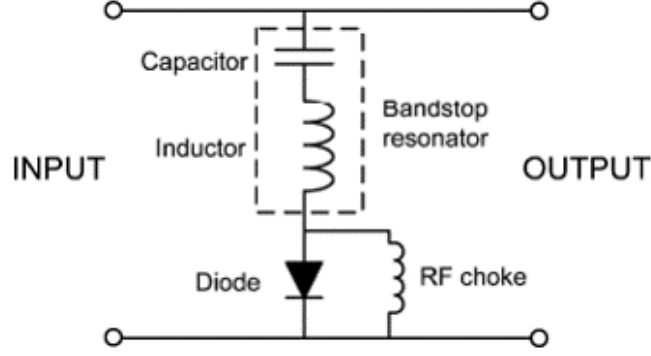
Fig. 1.13. The basic circuit of a bandstop limiter with a Schottky diode [48].

1.4   Motivation

In this dissertation, the synthesis of the triplet absorptive topology is presented in detail. The coupling matrix of this topology is derived. The synthesis theory extends to an arbitrary phase of the transmission line used in the topology. A new FSL that yields state-of-the-art performance is proposed. It employs the triplet absorptive filter topology, which enables absorptive response in a wider tuning range, to achieve high isolation (70 dB) everywhere in its octave tuning range. This was not possible with any existing FSLs. This triplet filter topology also gives a bandstop-to-all-pass response, which enables controlled attenuation, or variable-attenuation control. The filter is implemented in high-Q evanescent-mode cavity technology, which yields low insertion loss in all-pass response. The proposed FSL is integrated with feedback control loops to enable in-field operations. For one step further, the FSL system is redesigned for optimization of robustness and reliability without compromising the state-of-the-art RF performance.

1.5   Dissertation Overview

The dissertation is organized as follows.

Chapter 2 presents the coupling matrix synthesis of the triplet absorptive filter topology. Fully-absorptive, quasi-absorptive, and all-pass responses are discussed in detail. Lossy synthesis with Q-factor and bandwidth is performed, and effects on the performance are presented.

Chapter 3 demonstrates a quasi-absorptive bandstop-to-all-pass filter in 1.1 GHz to 2 GHz frequency range using the synthesis methodology described in Chapter 2. The filter can reconfigure its isolation level from all-pass to variable-attenuation absorptive bandstop response at the desired center frequency within its frequency range. The all-pass state insertion loss is minimally 2.3 dB occurring at 2 GHz and maximally 3.1 dB occurring at 1.1 GHz. The demonstration is fabricated with evanescent-mode cavity resonators and tuned by high-quality piezo-electric actuators. The extracted unloaded resonator Q-factor is 400.

Chapter 4 proposes an FSL using the tunable filter presented in Chapter 3. The filter is integrated with feedback control loops and a power detection scheme. The FSL can operate in three distinct modes: user-activated bandstop, power-activated bandstop, or all-pass mode. In a user-activated bandstop mode, the FSL can present a measured notch of $45-55$ dB in its $1.5-2$ GHz tuning range. The out-of-band insertion loss is less 0.8 dB. In the all-pass mode, the measured loss is less than 3.1 dB including the two SMA connectors and the associated connector-to-microstrip transitions. In the power-activated mode, the filter switches automatically between its bandstop and all-pass responses based on the incident power level at any user-defined frequency within the $1.5-2$ GHz range. The threshold power level is tunable in the -45 to $+8$ dBm range. The FSL demonstrates state-of-the-art performance.

Chapter 5 presents a novel design procedure to optimize the robustness of the evanescent-mode substrate-integrated cavity resonators and filters. The trade-offs among robustness, unloaded resonator Q-factor and volume are discussed in detail. Three implementations and five designs of resonators are comparatively studied. The filter, core of the FSL in Chapter 4, is redesigned as a demonstration. The robustness of the filter is characterized by long-term and repeatability tests. The filter has main-

tained a 45-dB notch throughout the 5-day measurement and without drift at the end of the measurement. RF power handling, vibration, and temperature sensitivity tests have been performed. The results demonstrate that careful design can significantly improve the robustness of the cavity filters and other cavity applications.

Chapter 6 summarizes the contributions of this dissertation and discusses future opportunities. A fourth-order bandpass-to-all-pass filter is proposed as an extension of the second-order triplet filter topology. A direct resonator monitoring architecture is proposed with frequency synthesizer. The advantages and disadvantages are discussed.

2. SYNTHESIS OF THE TRIPLET ABSORPTIVE FILTER TOPOLOGY

This chapter presents the filter synthesis of the triplet absorptive topology. There are three approaches to synthesize a filter topology: mixed-parameter analysis, even- and odd-mode analysis, and coupling matrix synthesis. The mixed-parameter analysis is used by the author to derive the conditions in the realization of the quasi-absorptive bandstop, fully-absorptive bandstop, and all-pass response. The even- and odd-mode analysis was described in [16] and is used in [30]. The coupling matrix synthesis is developed by the author to simplify the synthesis process and to optimize the filter response. The coupling matrix synthesis also enables synthesis of higher-order triplet filter topology, which is not possible with the mixed-parameter analysis and the even- and odd-mode analysis mainly due to mathematical complexity.

2.1 Mix-Parameter Analysis

The mix-parameter analysis, which combines ABCD, Y, and S parameters, is the most straightforward approach to obtain the transfer functions of a filter network. This approach is not limited to narrowband as coupling matrix.

The coupling diagram of the triplet absorptive filter is shown in Fig. 2.1(a). This filter consists of two resonators in two parallel networks. The upper branch is a first-order bandstop configuration, which includes two segments of the transmission line of electrical length θ_T, and resonator 1 with coupling coefficient k_1. The lower branch is a first-order bandpass configuration, which includes resonator 2 coupled to the source and the load with coupling coefficient k_2 and $-k_2$. In the bandstop state, the signals going through the upper and the lower branch have the same magnitude and opposite phase at the center frequency, so that the signals are canceled, resulting in a theoreti-

cally infinite notch. In the all-pass state, the off-band part of the signal passes through the bandstop branch and the in-band part of the signal passes through the bandstop branch. Figure 3(b) shows the equivalent circuit topology where the resonators are represented with their RLC equivalent circuit. The couplings are implemented using the admittance inverters J_n, which is related to the coupling coefficient k_n by the following equation as described in [31],

$$J_n = \frac{k_n}{\sqrt{Z_0 Z_R}}. \tag{2.1}$$

where Z_R is the characteristic impedance of an ideal resonator defined by $Z_R = \sqrt{L/C}$, and Z_0 is the characteristic impedance of the transmission line used.

The $ABCD$ representation of the triplet absorptive topology is shown in Fig. 2.1. Here, Y_{res} represent the admittance of the resonator. It can be modeled as

$$Y = \frac{j}{Z_R}(\frac{\omega}{\omega_0} - \frac{\omega_0}{\omega}) + \frac{j}{Z_R}B + \frac{1}{Z_R Q_u}, \tag{2.2}$$

where Z_R is the impedance of a resonator defined by $\sqrt{L/C}$. Q_u is the Q-factor and B is susceptance, or detuning of the resonator. Y_1 is the combination of the admittance of the resonator 1, Y_{res1}, and the inverter k_1, or

$$Y_1 = \frac{J_1^2}{Y_{res1}}. \tag{2.3}$$

The $ABCD$ matrix of the upper branch and the lower branch is calculated and converted to Y matrix. The Y matrices are combined and converted to S matrix. The flow is illustrated in Fig. 2.2. The S parameters of the triplet absorptive topology is obtained

$$S_{21} = \frac{2(j\cos(\theta_T) + \sin(\theta_T))(Z_0^2 J_1^2 J_2^2 \sin^2(\theta_T) - Y_1 Y_2 - j J_2^2 Y_1 Z_0 \sin(2\theta_T))}{(2J_2^2 Y_1 + J_1^2 J_2^2 Z_0)(-jY_2 J_1^2 \cos(\theta_T) + (2J_1^2 J_2^2 Z_0 + Y_2 J_1^2)\sin(\theta_T))} \tag{2.4}$$

$$S_{11} = \frac{jZ_0 J_1^2 J_2^2(j\cos(\theta_T) + \sin(\theta_T))(-2J_2^2 Y_1 + Y_2 J_1^2 + 2J_2^2 Y_1 \cos(2\theta_T) + jZ_0 J_1^2 J_2^2 \sin(2\theta_T))}{(2J_2^2 Y_1 + J_1^2 J_2^2 Z_0)(-jY_2 J_1^2 \cos(\theta_T) + (2J_1^2 J_2^2 Z_0 + Y_2 J_1^2)\sin(\theta_T))} \tag{2.5}$$
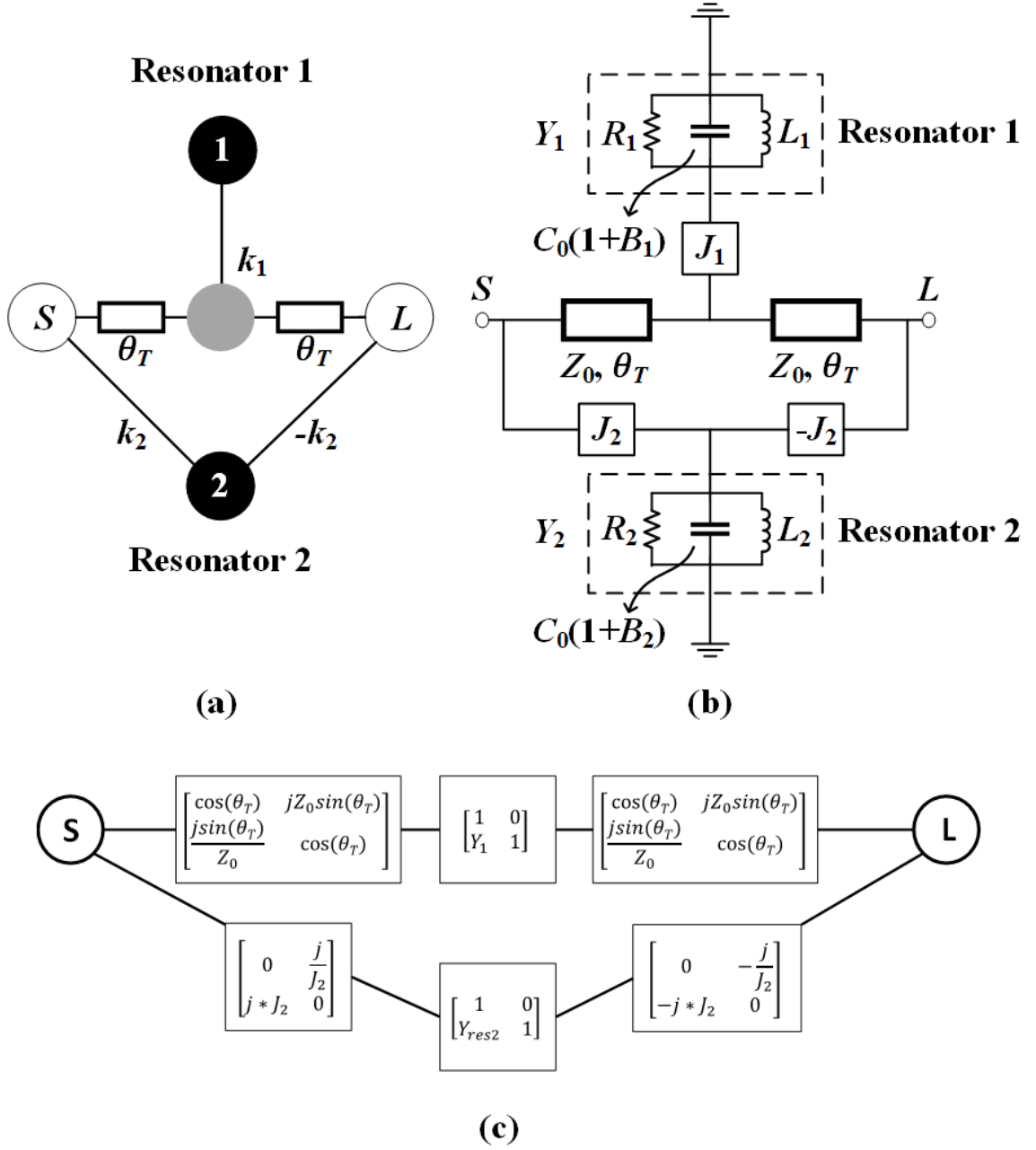
Fig. 2.1. (a) Coupling diagram of the triplet absorptive topology with admittance inverters. (b) Circuit topology (a) with admittance inverters. (c) ABCD matrix representation of (b).
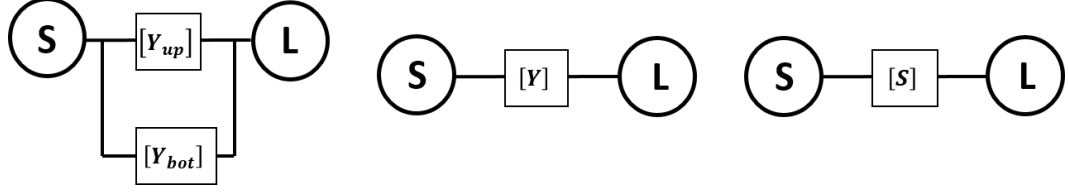
Fig. 2.2. Flow to derive S parameters from the $ABCD$ matrix.

2.1.1 All-Pass Condition

The all-pass condition is achieved when S_{11} in (2.5) is set to 0 across the entire frequency domain, and S_{21} in (2.4) is set to 1. To simplify the calculations, S_{21} in (2.4) is set to 1 at the center frequency. To get 0 for S_{11} across the entire frequency domain, all terms should be equal to 0 so that S_{11} is independent of frequency. An ideal resonator admittance $Y_{n,ideal}$ is used here to solve for the conditions. The admittance $Y_{n,ideal}$ is defined as

$$Y_{n,ideal} = \frac{1}{Z_R}(\frac{\omega}{\omega_0} - \frac{\omega_0}{\omega}) + \frac{i}{Z_R}B_n. \tag{2.6}$$

Under this condition, two relations are obtained from (2.5)

$$k_2 = \frac{\pm k_1}{2\sin\theta_T}, \tag{2.7}$$

$$B_1 - B_2 = \frac{k_1^2}{2}\cot(\theta_T). \tag{2.8}$$

And one relation is obtained from (2.4)

$$B_1 + B_2 = \frac{k_1^2}{2}\cot(\theta_T). \tag{2.9}$$

The complete solution to obtain the all-pass response is

$$k_2 = \frac{\pm k_1}{2\sin\theta_T}, \tag{2.10}$$

$$B_1 = \frac{k_1^2}{2}\cot(\theta_T), B_2 = 0. \tag{2.11}$$
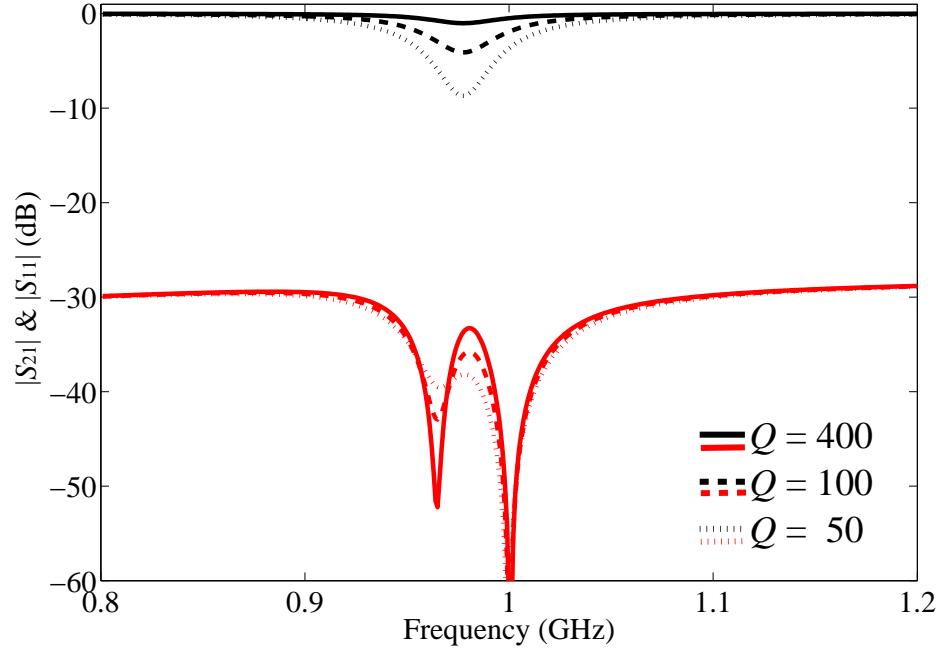
Fig. 2.3. Simulated all-pass state response in ADS with three different resonator Q-factors: 50, 100 and 400. In this design, the k_1 value is 0.2.
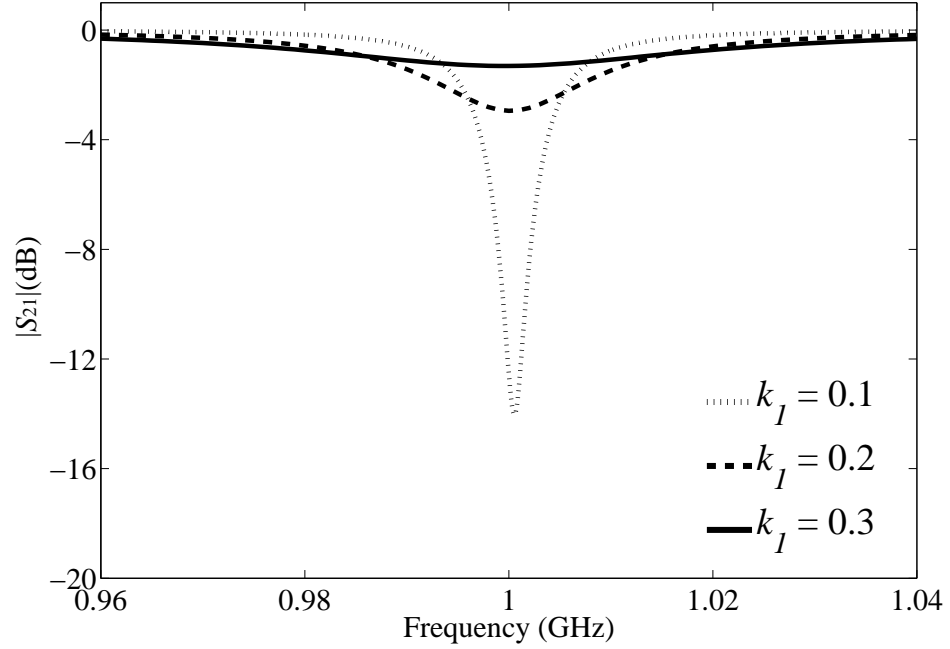
Fig. 2.4. Simulated all-pass state response in ADS with three different coupling k_1 value: 0.1, 0.2, and 0.3. In this design, the Q-factor is 300.

This solution applies to ideal resonators with infinite Q-factor. In reality, finite resonator Q-factor results in some insertion loss in the all-pass response. This insertion loss can be estimated by either replacing the ideal resonator admittance $Y_{n,ideal}$ with Y_n in (2.4), or with simulations. Figure 2.3 compares the all-pass response for three different resonator Q-factors: 50, 100 and 400. These are obtained by using Advanced Design System (ADS), at the design frequency of 1 GHz with coupling value $k_1 = 0.2$. The coupling k_2 follows the relationship derived in (2.10). Apart from the resonator Q_u, the coupling value k_1 will also affect the insertion loss of the all-pass state. Figure 5 also compares the all-pass response for three different coupling values: 0.1, 0.2, and 0.3 at the design frequency of 1 GHz with resonator $Qu = 300$. As can be seen, higher resonator Q-factor and higher coupling values result in lower all-pass insertion loss. With an evanescent-mode cavity, a Q-factor of 400 can be achieved. Based on the simulation results, high-Q implementations give less than 3-dB insertion loss for the all-pass state with a coupling value of 0.2.

2.1.2   Bandstop Condition

The quasi-absorptive bandstop condition is satisfied when S_{21} is set to 0 at the center frequency while the S_{11} condition is not required for the quasi-absorptive bandstop response. In order to obtain the absorptive response with an infinite notch, the resonator Q-factor needs to be included in the equations. At the design center frequency, the resonator admittance Y_{n,w_0} can be simplified as

$$Y_{n,w_0} = \frac{i}{Z_R}B_n + \frac{1}{Z_R Q_{u,n}}. \tag{2.12}$$

The relation between k_1 and k_2 in (2.10) is kept since it corresponds to the required condition for the all-pass state. If we assume that both resonators have the same Q-factor, the detunings can be solved from (2.4) by separating the real and imaginary parts, resulting in

$$B_1 = \pm\sqrt{\frac{k_1^4}{4} - \frac{1}{Q_u^2}} \tag{2.13}$$

and,

$$B_2 = -\frac{1}{2}k_1^2\cos(\theta_T) \mp \sqrt{\frac{k_1^4}{4} - \frac{1}{Q_u^2}}. \tag{2.14}$$

In reality, due to the effect of the transmission line electrical length frequency dependence, B_1 and B_2 in (2.13), (2.14) are slightly modified. The simulated absorptive bandstop responses with resonator Q_us of 50, 100 and 400 are simulated in ADS, and shown in Fig. 2.5. With ideal resonators, the S_{21} is an ideal 2nd-order Butterworth bandstop response. This can be verified by inserting in (2.13) and (2.14) infinite Q-factor into the S_{21} expression in (2.4). The simplified S_{21} becomes:

$$|S_{21}|^2 = \frac{4p^4}{4p^4 + (k_1^2)^4} \ at \ Q_u \to \infty, \tag{2.15}$$

with 3-dB bandwidth of $\sqrt{2}k_1^2$. With finite resonator Q-factor, the S_{21} still shows infinite notch at the design center frequency. The 3-dB bandwidth with finite Q-factor can be expressed as:

$$BW = \sqrt{\frac{4 + k_1^4 + \sqrt{8k_1^4 - k_1^8}}{4}} - \sqrt{\frac{4 - k_1^4 - \sqrt{8k_1^4 - k_1^8}}{4}}. \tag{2.16}$$

Figure 2.6 shows the absorptive bandstop response for three different coupling values: 0.1, 0.2, and 0.3 at the design center frequency of 1 GHz with resonator Q-factor as 300.
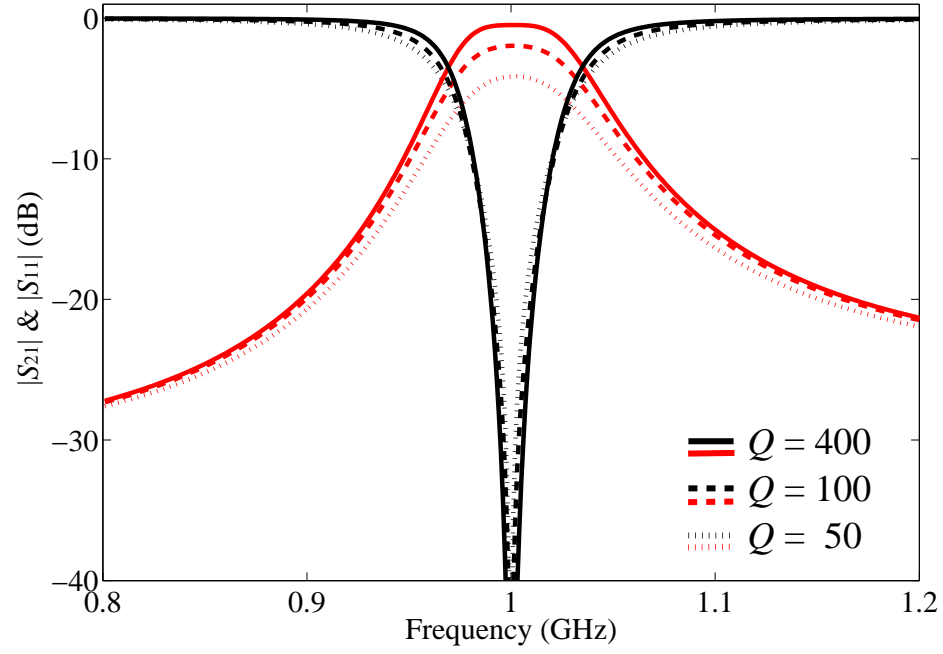
Fig. 2.5. Simulated absorptive Bandstop response in ADS with three resonator Q_u: 50, 100 and 400. In this design, the k_1 value is 0.2.
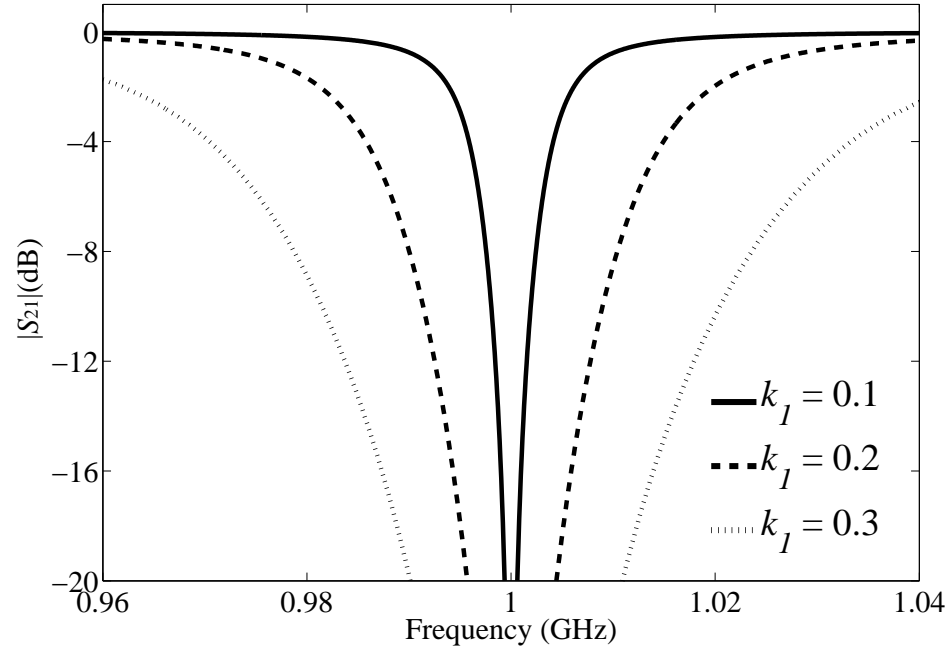
Fig. 2.6. Simulated absorptive Bandstop response in ADS with three different coupling k_1 value: 0.1, 0.2, and 0.3. In this design, the Q_u is 300.

2.2　Even- and Odd-Mode Analysis
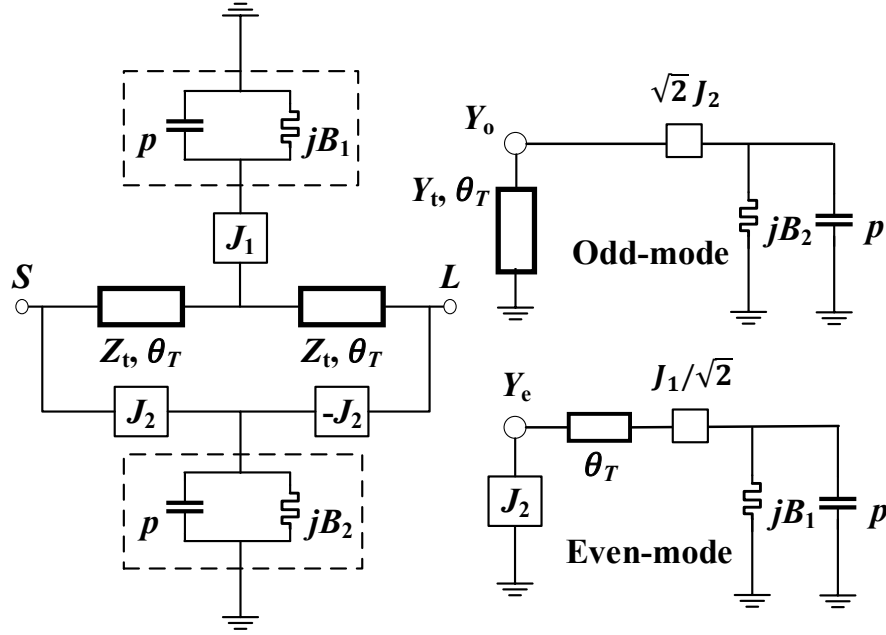
Fig. 2.7. Low-pass prototype of the triplet absorptive topology and
its even and odd mode admittance.

The even- and odd-mode analysis uses a different approach to obtain the low-pass
prototype and its S-parameters. The even- and odd-mode admittance are illustrated
in Fig. 2.7. For even mode, the middle of the lower branch is grounded and the
upper branch breaks in the middle. The equivalent circuit becomes a transmission
line of θ_T in series with resonator 1 with admittance inverter of $J_1/\sqrt{2}$. The inverter
J_1 is connected to ground and therefore gives equivalent admittance of infinity. The
even-mode admittance is given by

$$Y_e = Y_t \frac{\frac{J_1^2}{2(p+jB_1)}\cos\theta_T + jY_t\sin\theta_T}{Y_t\cos\theta_T + j\frac{J_1^2}{2(p+jB_1)}\sin\theta_T},\tag{2.17}$$

where p is the frequency variable $j\omega$. For odd mode, the middle of the upper branch is
grounded and the lower branch breaks in the middle. The equivalent circuit becomes
resonator 2 with admittance inverter of $\sqrt{2}J_2$ in parallel with a transmission line of

θ_T. If θ_T is 90 degrees, the shorted transmission line is equivalent to open. The odd-mode admittance is given by

$$Y_o = \frac{2J_2^2}{(p + jB_2)} - jY_t \cot \theta_T. \tag{2.18}$$

It should be noted that if θ_T is 90 degrees, the even- and odd-mode admittance can be simplified as

$$Y_e = \frac{2(p + jB_1)}{J_1^2}, \tag{2.19}$$

and

$$Y_o = \frac{2J_2^2}{(p + jB_2)}. \tag{2.20}$$

The transmission and reflection coefficients can be obtained with the following equations:

$$S_{21} = \frac{1 - Y_e Y_o)}{(1 + Y_e)(1 + Y_o)}, \tag{2.21}$$

and

$$S_{11} = \frac{Y_o - Y_e)}{(1 + Y_e)(1 + Y_o)}. \tag{2.22}$$

The transmission and reflection coefficients are calculated and the results are the same as using mixed-parameter analysis.

2.3 Coupling Matrix Synthesis

The coupling matrix is commonly used to synthesize filter typologies due to its convenience to derive filter response at the desired center frequency and with desired bandwidth. Lossy coupling matrix synthesis enables prediction of filter behavior with finite resonator Q-factors. The coupling coefficients are a phase shift of 90 degrees, and therefore if a section of transmission line is involved, usually the electrical length is multiple of quarter wavelength [19,20,24–27,29]. The coupling coefficient to represent 90 degrees of a transmission line is adequate for most of the bandstop typologies. It limits the investigation of advanced typologies. Furthermore, for existing typologies, the filter behavior with non-90 degree inverter is impossible to model in coupling

matrix and therefore hard to predict in the real application with fabrication tolerance. This section introduces a representation of a transmission line with an arbitrary phase in the coupling matrix. This technique is used in the coupling matrix model of the triplet absorptive filter topology.

2.3.1 Transmission line with Arbitrary Phase

A section of transmission line with admittance Y_0 and electrical length of θ_T is shown in Fig. 2.8(a). This transmission line can be represented as an admittance inverter with two susceptance, shown in Fig. 2.8(b). The J and B_J can be calculated when both of them are terminated with a load Y_L and match the input admittance. The admittance of the transmission line with termination Y_L is given by
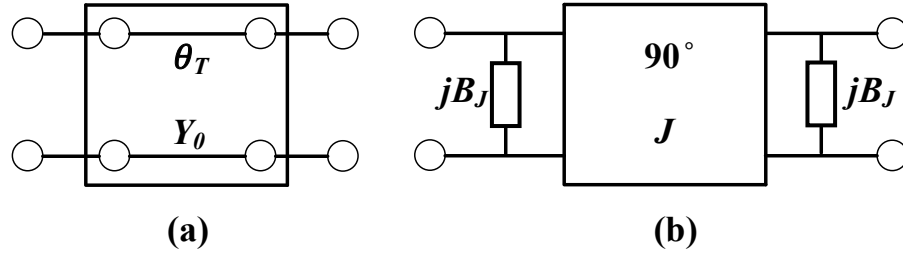
Fig. 2.8. (a) Circuit network of transmission line with admittance Y_0 and electrical length of θ_T. (b) Circuit network of an admittance inverter of J with two susceptance of B_J.

$$Y_{input} = Y_0 \frac{Y_L \cos \theta_T + jY_0 \sin \theta_T}{Y_0 \cos \theta_T + jY_L \sin \theta_T}. \tag{2.23}$$

The admittance of the admittance inverter with two susceptance B_J is given by

$$Y_{input} = \frac{J_i^2}{jB_J + Y_L} + jB_J = \frac{J_i^2 - B_J^2 + jB_J Y_L}{jB_J + Y_L}. \tag{2.24}$$

Two equations are equated and the following solution is obtained

$$B_J = -Y_0 \cot \theta_T, \tag{2.25}$$

$$J = \frac{\sqrt{Y_0}}{\sin \theta_T}. \tag{2.26}$$

In a low-pass prototype, The inverter J and coupling coefficient M is related by

$$J = M_i \sqrt{Y_0} \tag{2.27}$$

for external coupling, and

$$J = M_i Y_0 \tag{2.28}$$

for inter-resonator coupling. The susceptance B_J and detuning B_i in coupling matrix is related by

$$B_J = B_i Y_0. \tag{2.29}$$

2.3.2 Coupling Matrix of the Triplet Absorptive Topology

This section synthesize the triplet absorptive filter topology with arbitrary transmission line phase. The coupling diagram of the topology is shown in Fig. 2.9(a). The general coupling matrix of the absorptive bandstop topology can be represented as

$$M = \begin{bmatrix} -\cot(\theta_T) & 0 & \csc(\theta_T) & k_2 & 0 \\ 0 & B_1 - \frac{j}{Q\Delta} & k_1 & 0 & 0 \\ \csc(\theta_T) & k_1 & -2\cot(\theta_T) & 0 & \csc(\theta_T) \\ k_2 & 0 & 0 & B_2 - \frac{j}{Q\Delta} & -k_2 \\ 0 & 0 & \csc(\theta_T) & -k_2 & -\cot(\theta_T) \end{bmatrix} \tag{2.30}$$

where θ_T can be arbitrary degree. The equivalent topology after transformation is shown in Fig. 2.9.
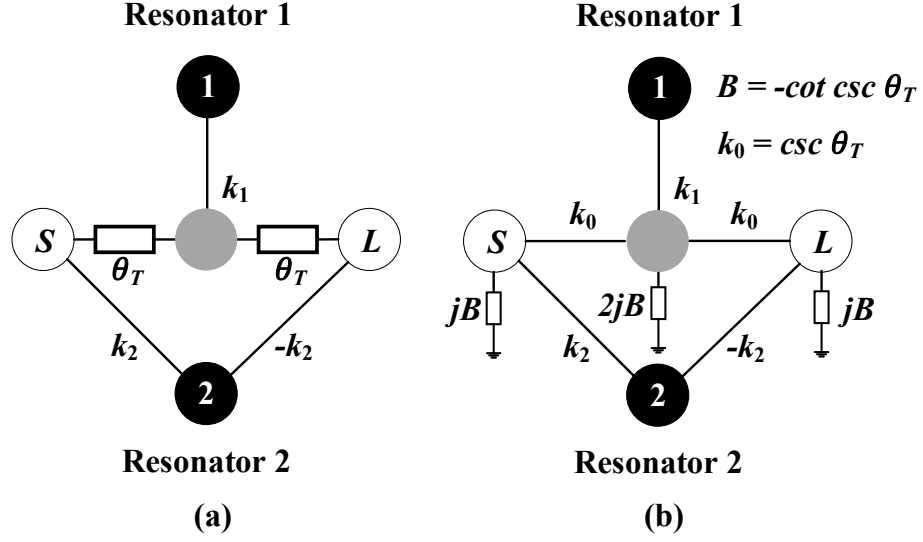
Fig. 2.9. (a) Coupling diagram of the absorptive bandstop-to-all-pass topology. (b) Transformation of (a). The transmission line section is replaced with a coupling of k_0 and two susceptance.

2.3.3 All-Pass Response

The coupling coefficients to achieve an all-pass filter response are calculated

$$
M = \begin{bmatrix}
-\cot(\theta_T) & 0 & \csc(\theta_T) & 0.595\csc(\theta_T) & 0 \\
0 & 0 & 1.19 & 0 & 0 \\
\csc(\theta_T) & 1.19 & -2\cot(\theta_T) & 0 & \csc(\theta_T) \\
0.595\csc(\theta_T) & 0 & 0 & -0.708\cot(\theta_T) & -0.595\csc(\theta_T) \\
0 & 0 & \csc(\theta_T) & -0.595\csc(\theta_T) & -\cot(\theta_T)
\end{bmatrix}
\tag{2.31}
$$

With ideal resonators, the transmission coefficient is calculated. The transmission coefficient for θ_T of 90 degree is given by

$$
S_{21} = \frac{-s^2 + 0.501335}{s^2 + 1.4161s + 0.501335}.
\tag{2.32}
$$

The transmission coefficient for θ_T of 45 degree is given by

$$
S_{21} = \frac{js^2 + 0.501335j}{s^2 + 1.4161s + 0.501335}.
\tag{2.33}
$$

Both of the responses are all-pass filter response. This response is plotted in Fig. 2.10.
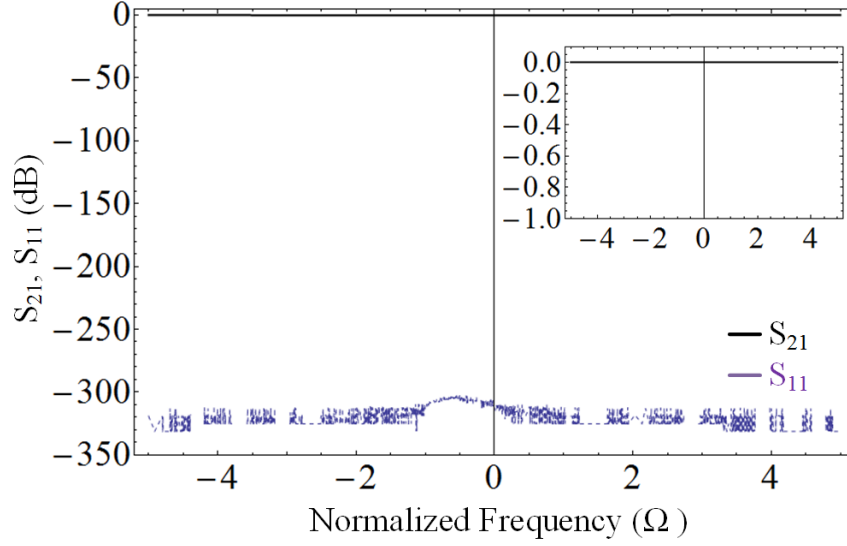
Fig. 2.10. All-pass response of the triplet absorptive filter topology. The results shown in this figure is mathematical. It is limited by the software's numerical precision. The inset shows the response from 0 to -1 dB.

The all-pass response for four different resonator Q-factors are compared at 3%, 6% and 10% fractional bandwidth with θ_T equal to 90 degrees and plotted in Fig. 2.11. It is shown that to achieve an insertion loss of less than 3 dB, resonator Q-factor should be larger than 300 for 3% bandwidth, 150 for 6% bandwidth, and roughly less than 75 for 10% bandwidth. It is noted that for different filter technologies, the maximum external coupling, or bandwidth is different. These figures provide a reference when designing the filter.
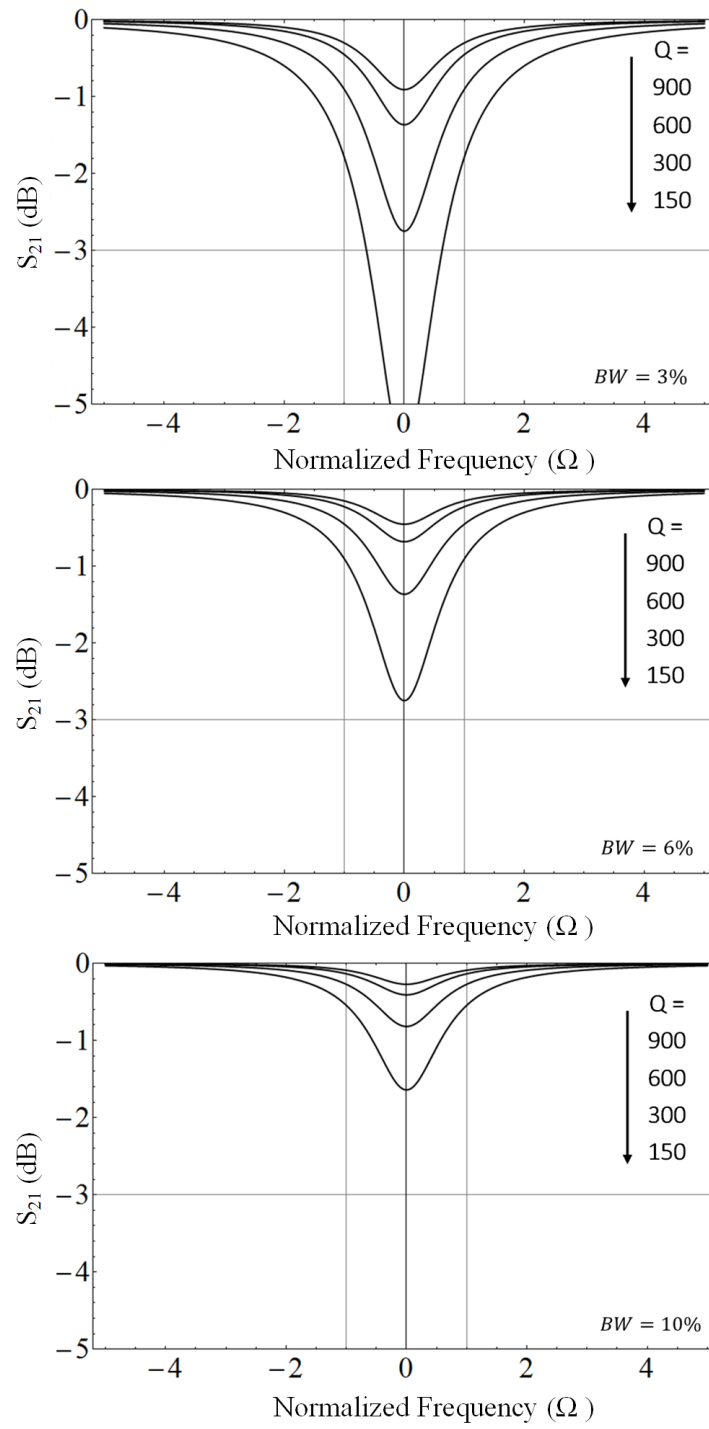
Fig. 2.11. Simulated all-pass state response with four different res-
onator Q-factors: 150, 300, 600, and 900 for 3%, 6%, and 10% frac-
tional bandwidth. θ_T is 90 degrees.
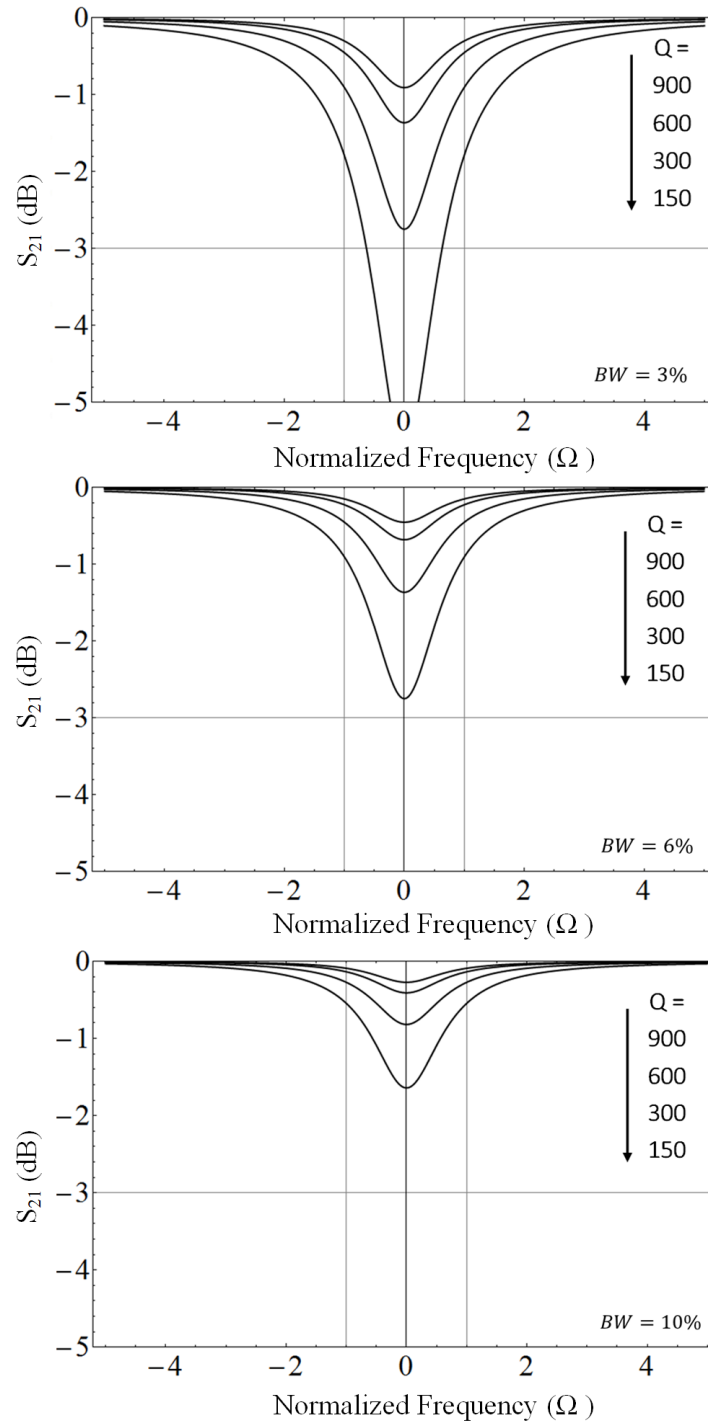
Fig. 2.12. Simulated all-pass state response with four different resonator Q-factors: 150, 300, 600, and 900 for 3%, 6%, and 10% fractional bandwidth. θ_T is 45 degrees.

The all-pass response for the same Q-factors and fractional bandwidths are plotted for θ_T equal to 45 degrees in Fig. 2.12. It is shown that for different θ_T, with a matched condition the all-pass response is the same.
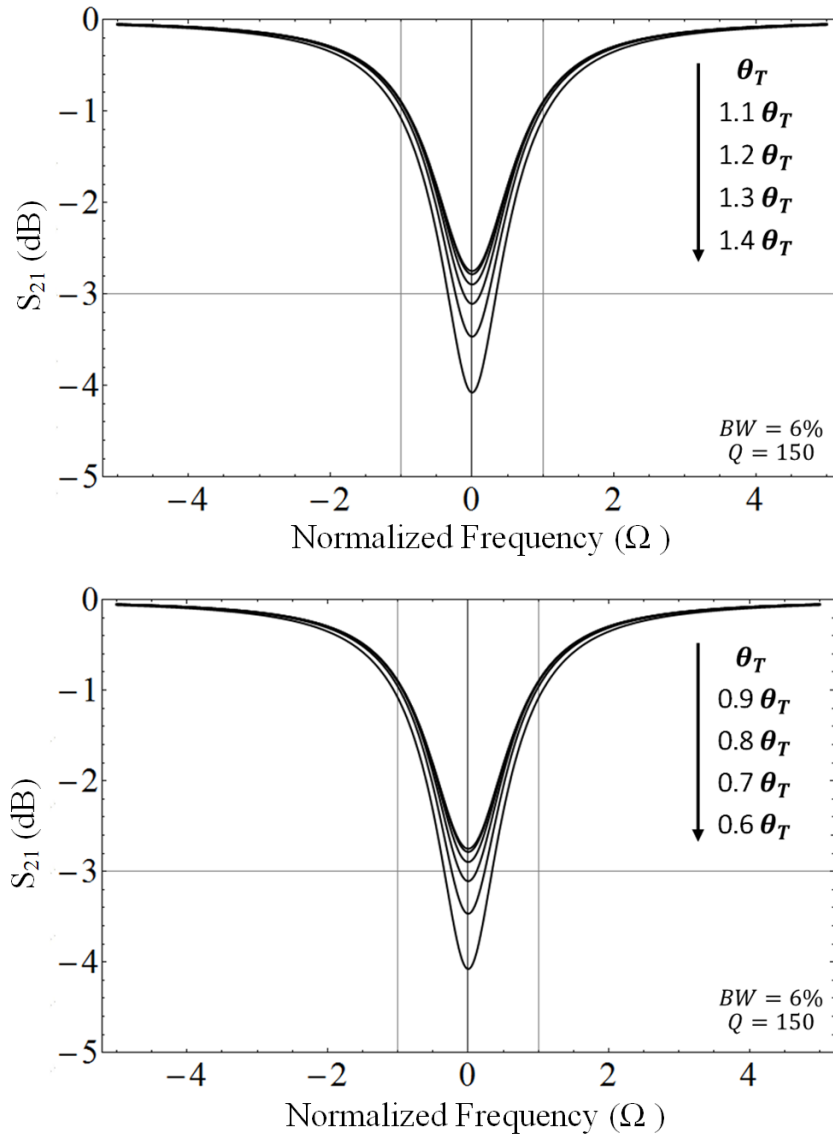
Fig. 2.13. Simulated all-pass state response with 100% variation of θ_T with Q-factors of 150 and fractional bandwidth of 6%.

The all-pass response with fixed external couplings but variation of θ_T is investigated and plotted in Fig. 2.13. This occurs when the filter is tuned away from the design center frequency. The transmission line degree varies with frequency. It is shown that the maximum insertion loss is 25%.

2.3.4 Quasi-Absorptive Bandstop Response

The coupling coefficients to achieve a second-order Butterworth bandstop response are calculated

$$M = \begin{bmatrix} -\cot(\theta_T) & 0 & \csc(\theta_T) & 0.595\csc(\theta_T) & 0 \\ 0 & 0.708 & 1.19 & 0 & 0 \\ \csc(\theta_T) & 1.19 & -2\cot(\theta_T) & 0 & \csc(\theta_T) \\ 0.595\csc(\theta_T) & 0 & 0 & -0.708[\cot(\theta_T)+1] & -0.595\csc(\theta_T) \\ 0 & 0 & \csc(\theta_T) & -0.595\csc(\theta_T) & -\cot(\theta_T) \end{bmatrix}$$
(2.34)

With ideal resonators, the transmission coefficient is calculated. The transmission coefficient for θ_T of 90 degree is given by

$$S_{21} = \frac{s^2}{s^2 + 1.4161s + 1.00267}.$$
(2.35)

The transmission coefficient for θ_T of 45 degree is given by

$$S_{21} = \frac{js^2}{s^2 + 1.4161s + 1.00267}.$$
(2.36)

Both of the responses are second-order Butterworth filter response. This response is plotted in Fig. 2.14.

In reality, resonators have a finite Q-factors. The quasi-absorptive response can be maintained by detuning the resonators. As an example, the triplet filter with Qfactor of 100 and a fractional bandwidth of 6 % is plotted from the coupling matrix in Fig. 2.15. It is shown that the attenuation level is degraded to 30 dB. The coupling matrix is adjusted by changing the detuning of the resonators. The corrected response is shown in Fig. 2.15. After correction, the attenuation is very deep. This coupling
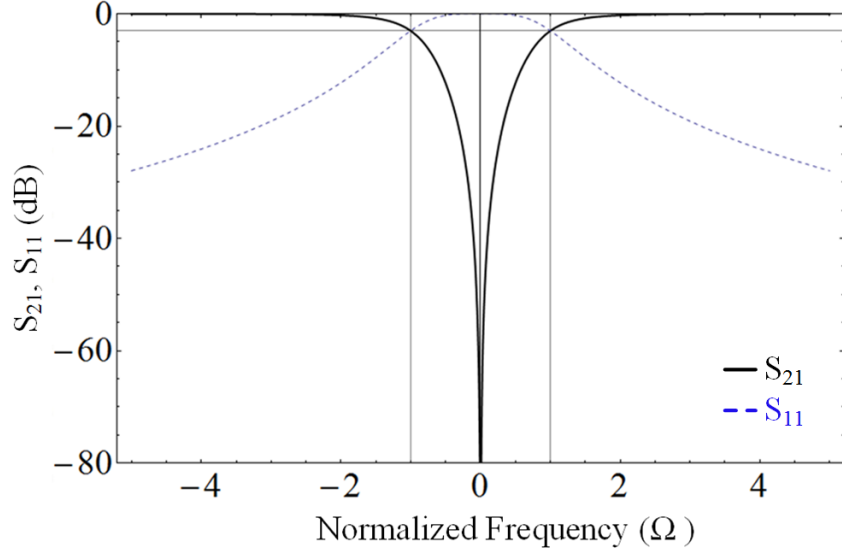
Fig. 2.14. Quasi-absorptive bandstop response of the triplet filter topology.
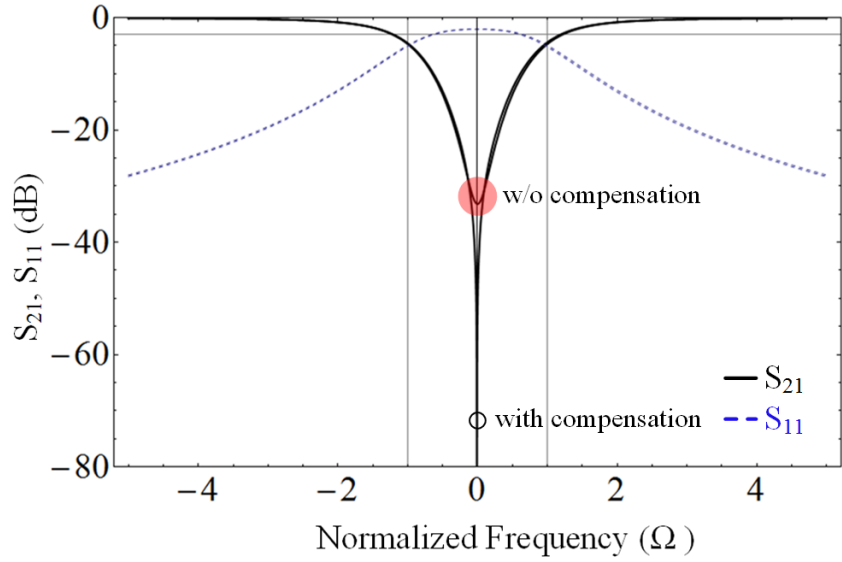
Fig. 2.15. Normalized frequency response of the triplet filter with and without detuning compensation.

matrix is still generic and can be applied to various θ_T. The corrected coupling matrix

is

$$
M = \begin{bmatrix}
-\cot(\theta_T) & 0 & \csc(\theta_T) & 0.595\csc(\theta_T) & 0 \\
0 & 0.6966 & 1.19 & 0 & 0 \\
\csc(\theta_T) & 1.19 & -2\cot(\theta_T) & 0 & \csc(\theta_T) \\
0.595\csc(\theta_T) & 0 & 0 & -0.49\cot(\theta_T) - 0.708 & -0.595\csc(\theta_T) \\
0 & 0 & \csc(\theta_T) & -0.595\csc(\theta_T) & -\cot(\theta_T)
\end{bmatrix}
\tag{2.37}
$$

This coupling matrix is generic and works with various θ_T.

2.3.5 Fully-Absorptive Bandstop Response

The coupling coefficients to achieve fully-absorptive response is derived.

$$
M = \begin{bmatrix}
-\cot(\theta_T) & 0 & \csc(\theta_T) & 0.5\csc(\theta_T) & 0 \\
0 & 0 & 1 & 0 & 0 \\
\csc(\theta_T) & 1 & -2\cot(\theta_T) & 0 & \csc(\theta_T) \\
0.5\csc(\theta_T) & 0 & 0 & -0.5\cot(\theta_T) & -0.5\csc(\theta_T) \\
0 & 0 & \csc(\theta_T) & -0.5\csc(\theta_T) & -\cot(\theta_T)
\end{bmatrix}
\tag{2.38}
$$

The frequency response from this coupling matrix is plotted in Fig. 2.16. It shows a fully-absorptive bandstop response with Q-factor of 2 and fractional bandwidth of 1. The fractional bandwidth is related with Qu by $\Delta = 2/Q_u$. If the resonator Q-factor is 50, the fractional bandwidth needs to be 4 %. If the resonator Q-factor is 100, the fractional bandwidth needs to be 1 %. If the resonator Q-factor is 400, the fractional bandwidth needs to be 0.25 %. The implementation of the filter needs to consider both bandwidth and available Q-factors for the resonators.
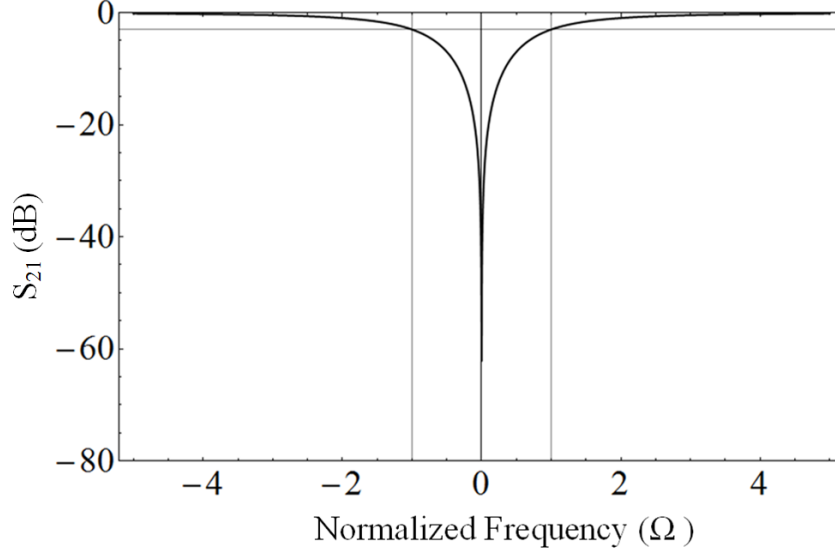
Fig. 2.16. Fully-absorptive bandstop response of the triplet filter topology.

2.4 Discussions

All of the methods discussed in the previous sections can synthesize the triplet filter topology, although they focus on different aspects. Coupling matrix synthesizes the low-pass prototype of the filter topology, which has a normalized frequency, bandwidth, and impedance. It can easily scale to the desired center frequency, bandwidth, and arbitrary source and load impedance [32]. With arbitrary phase representation technique, the coupling matrix can be used in the synthesis of more complex typologies. Another advantage of the coupling matrix is that if there are no analytical solutions for a certain topology, coupling coefficients can be solved numerically with computer-aided synthesis iterations as the entire synthesis is mathematical.

The mix-parameter and even- and odd- analysis are used when analytical solutions are available. For example, the quasi-absorptive bandstop response with ideal and non-ideal resonators to achieve Butterworth response, the fully-absorptive bandstop response with non-ideal resonators, and the all-pass response with ideal resonators of the triplet topology can be solved analytically. If there are no analytical solutions,

there two methods are limited. An example is an all-pass response with non-ideal resonators. It cannot be solved analytically, and therefore the behavior of the all-pass response is hard to understand or optimize with these two methods.

Another example is the higher-order synthesis of the triplet typology. With 90-degree transmission line section, the bandstop response of the triplet topology of higher orders is solved analytically with even- and odd- analysis [33]. The solution for an arbitrary degree of transmission line section is not available yet. The coupling matrix approach will be more straightforward.

In even- and odd-analysis, the even and odd modes of an unknown filter topology can be compared and mapped to a studied topology, to solve for the unknown topology. The mix-parameter does not have this advantage. The coupling matrix maps the entire transmission and reflection coefficients, which is mathematically harder to solve.

In conclusion, based on the author's experience, the easiest and fastest way to generate the S-parameters is the coupling matrix method, then the even- and odd-analysis. The easiest way to solve the coefficients of a topology for a specific transfer function is to map the even and odd modes. If this is not possible, the coupling matrix could be used to find numerical solutions.

3. L-BAND HIGH Q TUNABLE QUASI-ABSORPTIVE BANDSTOP-TO-ALL-PASS FILTERS

This chapter presents a demonstration of the triplet absorptive filter topology synthesized in the previous chapter. The filter is designed and implemented using evanescent-mode cavity technology and is the first implementation of this topology in this technology. Both quasi-absorptive bandstop response and all-pass response are achieved.

3.1 Filter design and Implementation

The filter is designed with a frequency range from 1 to 2 GHz and implemented with evanescent-mode cavity resonators because of its high Q-factors [58]. The resonators are loaded with a post with a small gap which can be tuned with piezoelectric actuators. The gap is designed to tune from 10 to 50 μm. The exploded view of the HFSS model for the filter is shown in Fig. 5.10. The top layer with a 50-Ω microstrip line source-to-load coupling is designed on a 0.508-mm thick Rogers 4003 substrate ($\varepsilon_r = 3.38$, $\tan(\delta) = 0.0027$). The cavities are designed on a 1.524-mm thick Rogers 4003 substrate. Each cavity resonator is loaded with a post that creates a parallel capacitance with the upper cavity wall and can be tuned with piezoelectric tuners. The filter can theoretically achieve a tuning range from 1 to 2 GHz if the gap is tuned from 8 to 48 μm. The filter couplings are realized through slots at the ground plane between the microstrip lines and the cavities. The angles of the slots determine the coupling values. Here, the angles are selected to be 136° for slot 1 and 104° for slot 2. The resulting k_1 is 0.2 and k_2 is 0.13, which satisfy the required condition to achieve an all-pass response. The pads on top of the coupling slots add shunt capacitance to the microstrip line to compensate the series inductance introduced by coupling slots.

The design method and equivalent circuit models of the slots and pads are explained in detail in [34]. The simulated loaded resonator Q-factor is approximately 440. The fabricated filter is shown in Fig. 3.2.
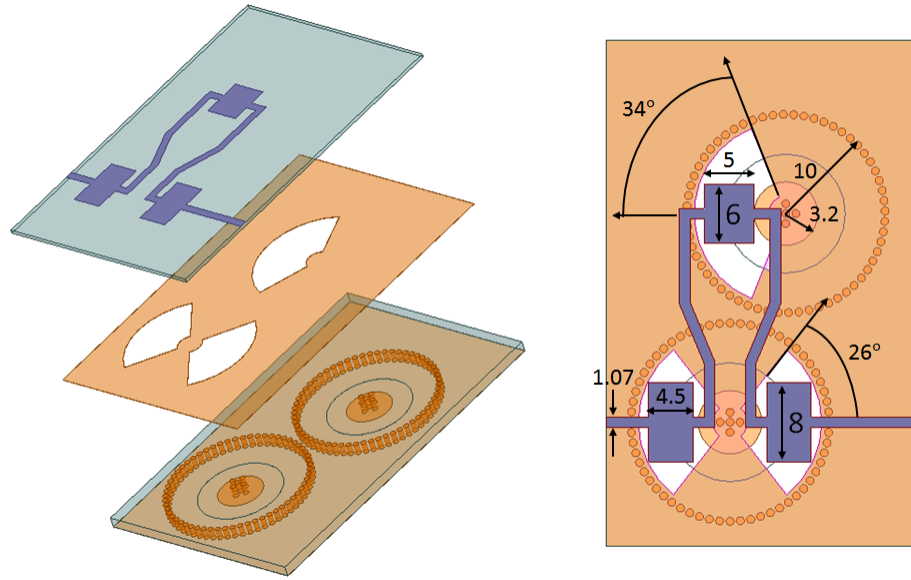
Fig. 3.1. Exploded view of the simulation model in HFSS and dimensions in mm for the evanescent-mode cavity filter.
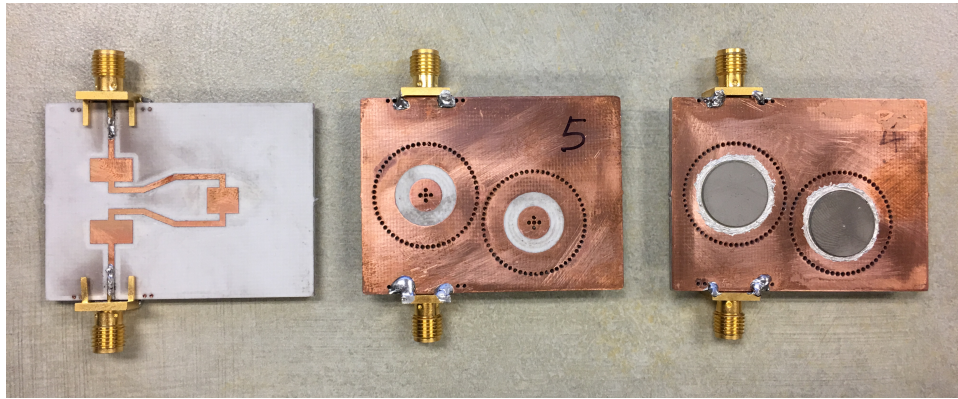
Fig. 3.2. Fabricated bandstop-to-all-pass cavity filters without and with piezoelectric actuators.

3.2   Measurement Results

The fabricated filter is measured with an Agilent N5230C network analyzer and Keithley 2410 providing ±200 V DC bias for the piezoelectric actuators. The filter can continuously tune from all-pass response to absorptive bandstop response with high isolation (70 dB) across its entire frequency range from 1.1 to 2 GHz. It is hard but possible to obtain 80-dB deep isolation with higher resolution from the DC power supply. Fig. 3.3 shows the measurement results for various attenuation levels.
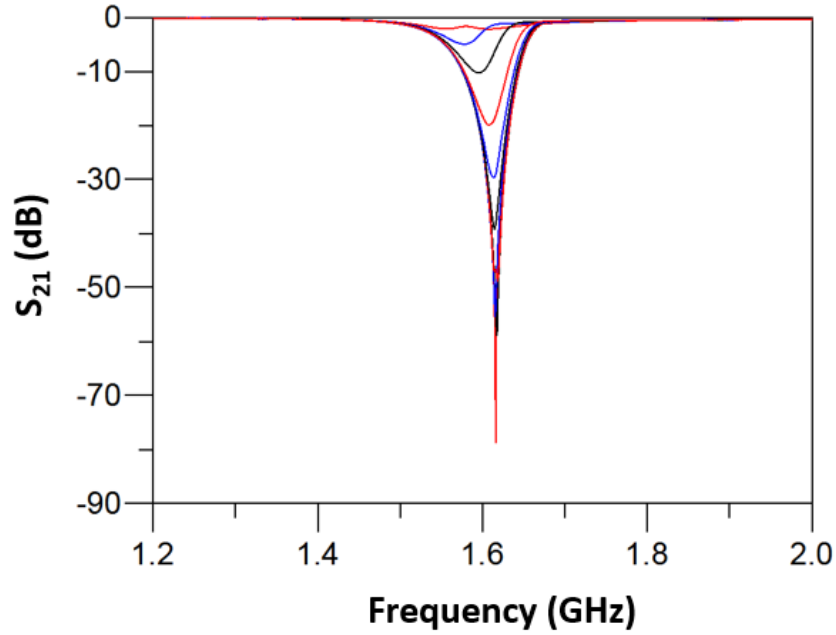
Fig. 3.3. Measured bandstop response with tunable attenuation levels from 80-dB to 2.16-dB.

This filter demonstrates a 70-dB attenuation across its entire tuning range. The measured 3-dB bandwidth is 4.3% at 1.1 GHz, and monotonic increasing to 9% at 2 GHz. The measured 10-dB bandwidth is 2.3% at 1.1 GHz and increasing to 4.9% at 2 GHz. Fig. 3.4(b) shows frequency response of quasi-absorptive bandstop state. The tuning range of this filter can be improved by reducing the initial gap of the cavity. The measured all-pass state insertion loss is decreasing from 3.14-dB at 1.1

GHz to 2.27-dB at 2 GHz as resonator Q-factor increases along frequency. Fig. 3.4(a) shows the frequency response of all-pass states across its tuning range. The extracted unloaded resonator Q-factor is approximately 400.

Figure 3.5 shows agreement between measurement results and simulation results in HFSS for both all-pass state and absorptive bandstop state.
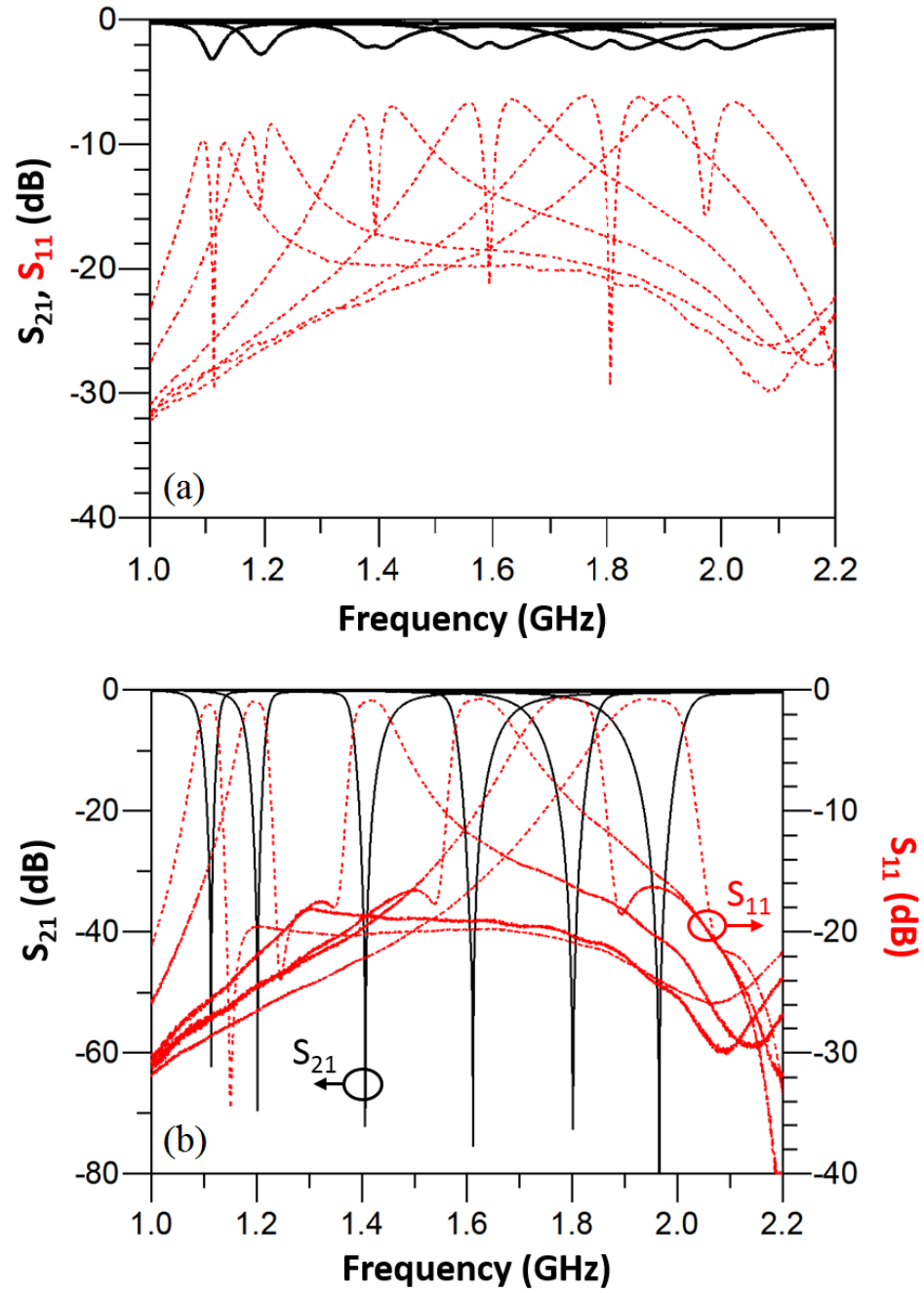
Fig. 3.4. Measured frequency response of (a) all-pass state across its entire tuning range and (b) absorptive bandstop state.
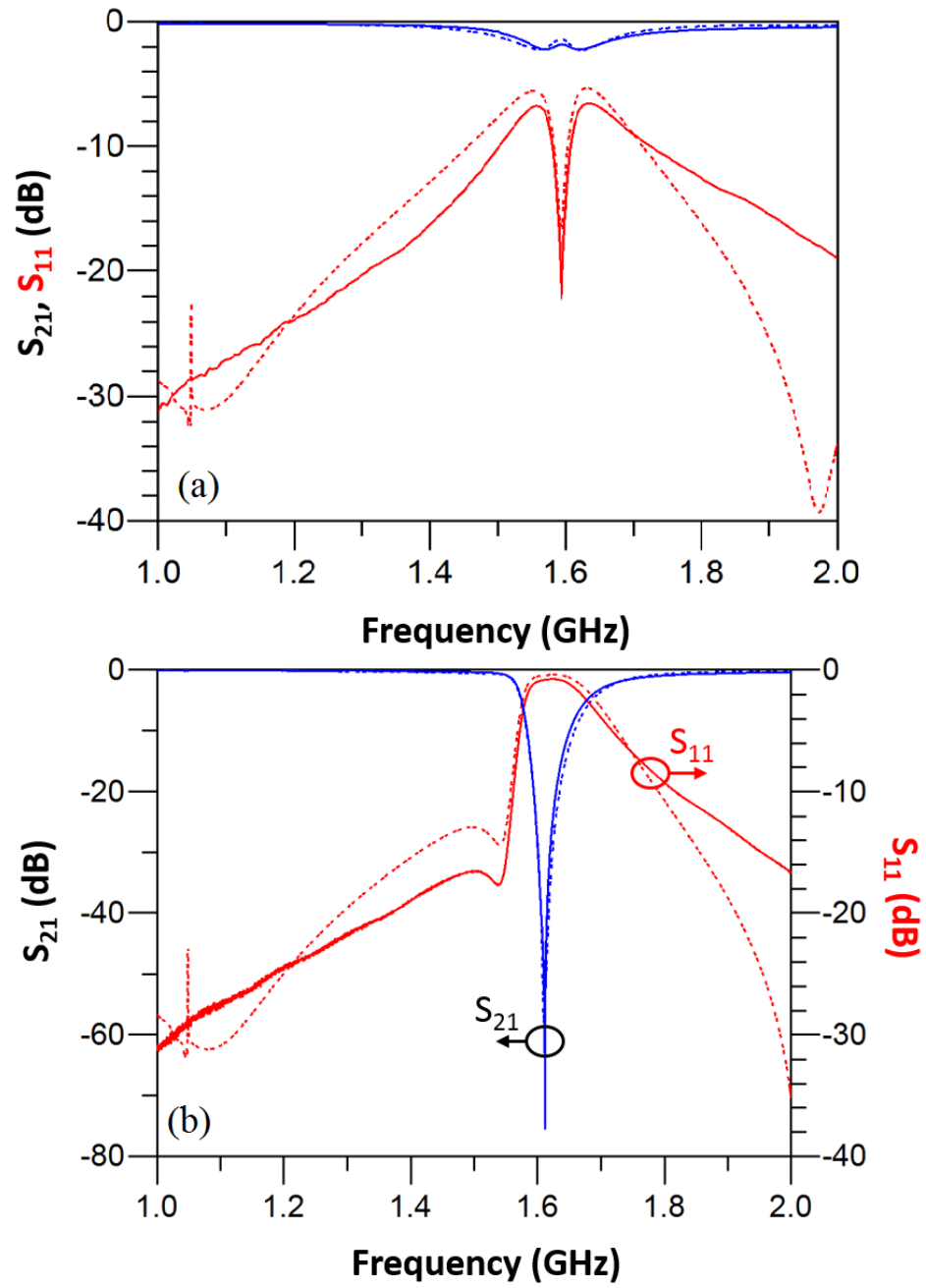
Fig. 3.5. Measured versus HFSS simulated frequency response of (a) all-pass state and (b) absorptive bandstop state.

4. FREQUENCY-SELECTIVE LIMITERS USING TRIPLE-MODE FILTERS

This chapter presents a new FSL based on a tunable triple-mode absorptive bandstop-to-all-pass filter topology and an integrated closed-loop feedback control scheme, as shown in Fig. 4.1. The developed FSL has three operating modes. The first mode is referred to as the user-activated bandstop mode since the user can request a notch regardless of the input power level. In this mode, a measured notch of $45-55$ dB in its $1.5-2$ GHz tuning range has been achieved. The out-of-band insertion loss is also less 0.8 dB. The second mode exhibits an all-pass characteristic (all-pass mode) with a measured loss of less than 3.1 dB. This measurement is done including the two SMA connectors and the associated connector-to-microstrip transitions. In the third mode (power-activated mode) the filter automatically activates a notch within the $1.5-2$ GHz range if the incident power exceeds preset a threshold. The power threshold level is tunable from -45 to $+8$ dBm. The implemented filter employs the high-quality substrate-integrated cavity technology with an extracted resonator unloaded Q-factor of 300.

4.1 System Architecture

The overall system diagram for the proposed filter is shown in Fig. 4.2 . It includes 1) an absorptive bandstop-to-all-pass filter (black font), 2) a power detector and comparator (green font) that are coupled to one of the resonators, and 3) a feedback control loop scheme (blue font) that controls both resonators. The absorptive bandstop-to-all-pass filter consists of two resonators in two parallel networks. By tuning either of these two resonators, the filter shows bandstop, all-pass, or variable-attenuation states. In this chapter, resonator 1 is locked at a given frequency while
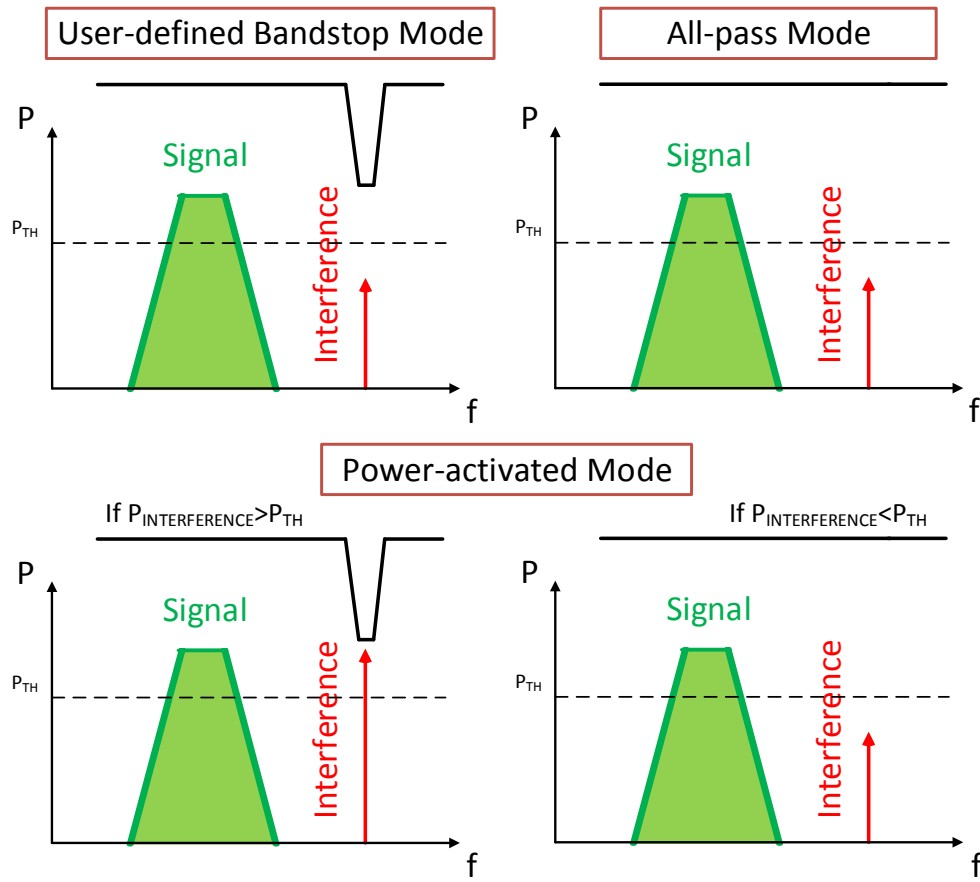
Fig. 4.1. A FSL using tunable triple-mode absorptive bandstop-to-all-pass filter. In power-activation mode, the filter will switch between bandstop response and all-pass response automatically based on input power at interferer frequency. In bandstop mode, a notch can be remained at desired frequency.

resonator 2 is tuned to realize the needed response. The advantage of assigning these roles to the resonators is that the power detector can be connected to the resonator that always tracks the incident signal (i.e. resonator 1) [30]. The output of the power detector is compared to a threshold voltage to decide the power-dependent response. The threshold voltage level can be easily controlled resulting in a reconfigurable power threshold level.
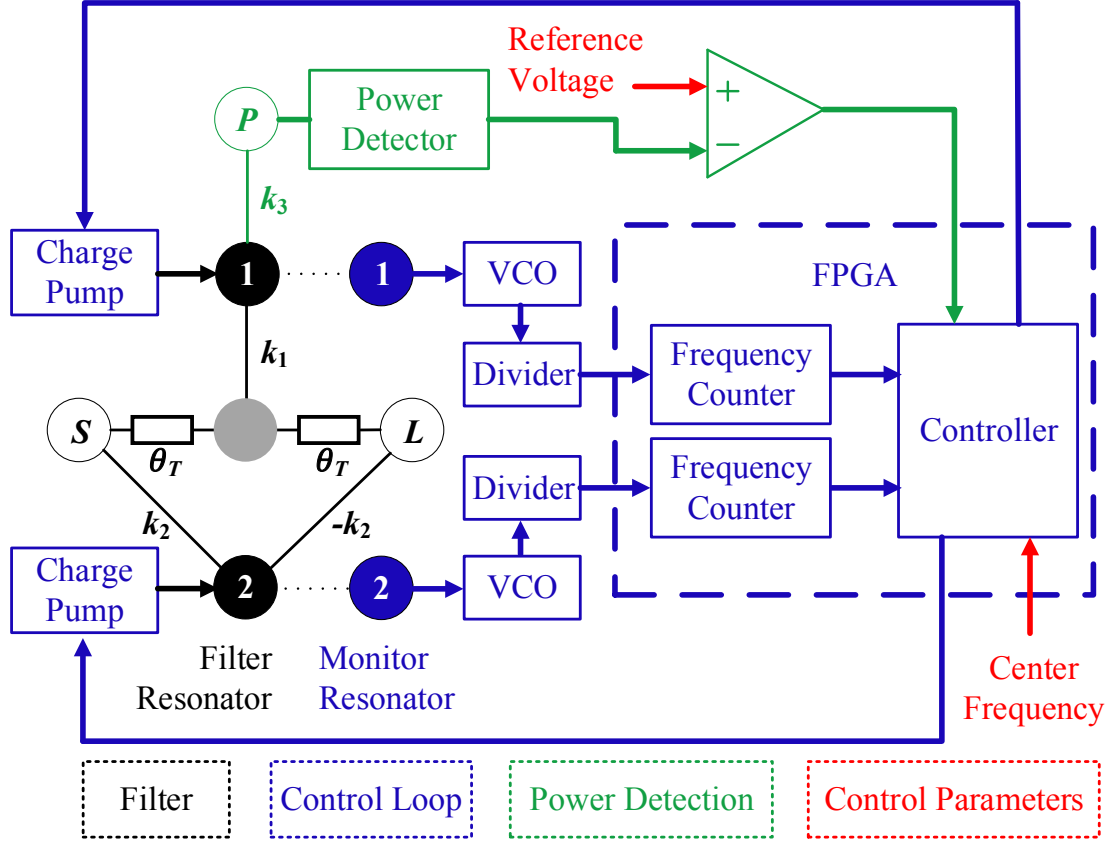
Fig. 4.2. Overall system diagram for proposed triple-mode filter with absorptive bandstop-to-all-pass filter (in black), feedback control loops (in blue), and power detection (in green). Tunable/input parameters are in red color.

The employed feedback control loop is implemented to enable field operation with variable temperature and other environmental factors. It also allows the user to operate the FSL in the field without the need for test equipment. As shown in Fig. 4.2, a monitoring resonator, at a different frequency range, is implemented so that it shares the same voltage-tuned diaphragm with the primary resonators. This way the monitoring resonator's frequency follows and the filter resonator's frequency. The monitoring resonator is implemented as part of a voltage-controlled oscillator (VCO).

The VCO output is frequency down-converted to fit the operating frequency range of the internal frequency counter modules in the FPGA. The control algorithm that compares the monitoring resonator's frequency to the desired frequency is programmed in the FPGA. The tuning voltage is subsequently generated through a charge pump that is also included in the developed module. The design theory and measured results of this architecture are presented in Sections III and IV respectively.

4.2 FSL Topology

In this section, the design theory of the proposed FSL is explained in detail. The absorptive bandstop-to-all-pass filter topology is presented first. Effect of filter bandwidth and finite Q_u on all-pass state response are also discussed. Subsequently, feedback loop control and power detection integration are described.

4.2.1 Bandstop-to-all-pass filter

The bandstop-to-all-pass filter topology is the same as the previous chapter. The design equations to achieve bandstop and all-pass responses are the same.

4.2.2 Power Detection

The designed absorptive bandstop-to-all-pass filter switches between the absorptive bandstop state and the all-pass state by detuning only one resonator. Therefore, continuous power detection at the center frequency is possible from resonator 1. The block diagram of the power detection scheme is shown in Fig. 4.3.

Power detection is realized by weak coupling input signal to a third output port, port P. The S_{31} (port 1 corresponding to port S, and port 3 corresponding to port P) response is derived in [30] as

$$|S_{31}|^2 = \frac{k_1^2 k_3^2}{4p^4 + (2k_3^2 + k_1^2)}, \tag{4.1}$$
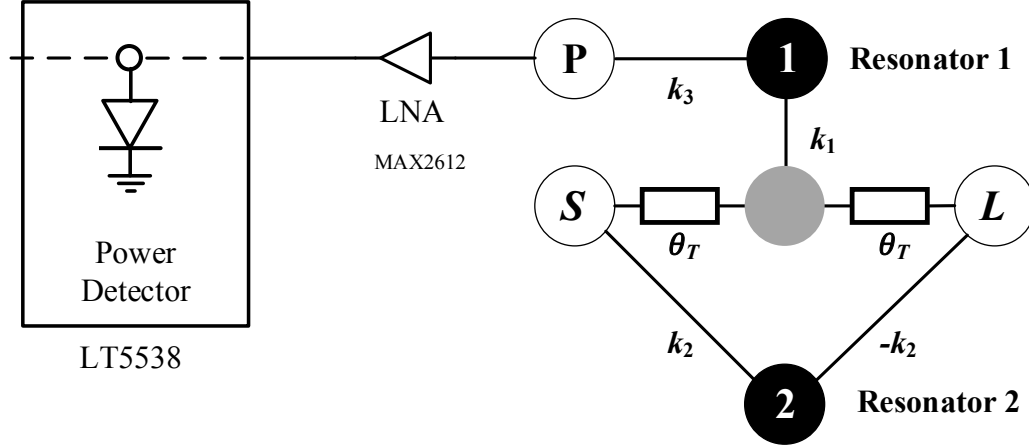
Fig. 4.3. Block diagram for bandstop-to-all-pass filter topology with third port for power detection. This diagram also includes detector diode connected to the third port.

where

$$p = \frac{1}{Z_R}(\frac{\omega}{\omega_0} - \frac{\omega_0}{\omega}) \tag{4.2}$$

This is a first-order bandpass response with the center frequency as resonator 1. Due to the fact that the S_{31} response does not vary when tuning resonator 2, the detected RF power from resonator 1 will be stable and independent of the tunable filter states. Since the coupling k_3 is very small, the implementation of the power detection does not significantly affect Q_u of resonator 1. The LNA is used to allow for a low power threshold level. An RF power detector diode is used to sense the amplified coupled signal and convert the power level into an analog voltage signal.

4.2.3 Feedback Loop Control

As discussed in [54], the high-Q piezoelectric tuners may exhibit hysteric behavior. In order to improve filter reliability, a feedback control loop is implemented on the filter. In [55, 56], the design theory of a back-to-back monitoring resonator is de-

scribed. A similar monitoring system is employed in this work. Figure 4.4 illustrates the block diagram of the monitoring and control loop.
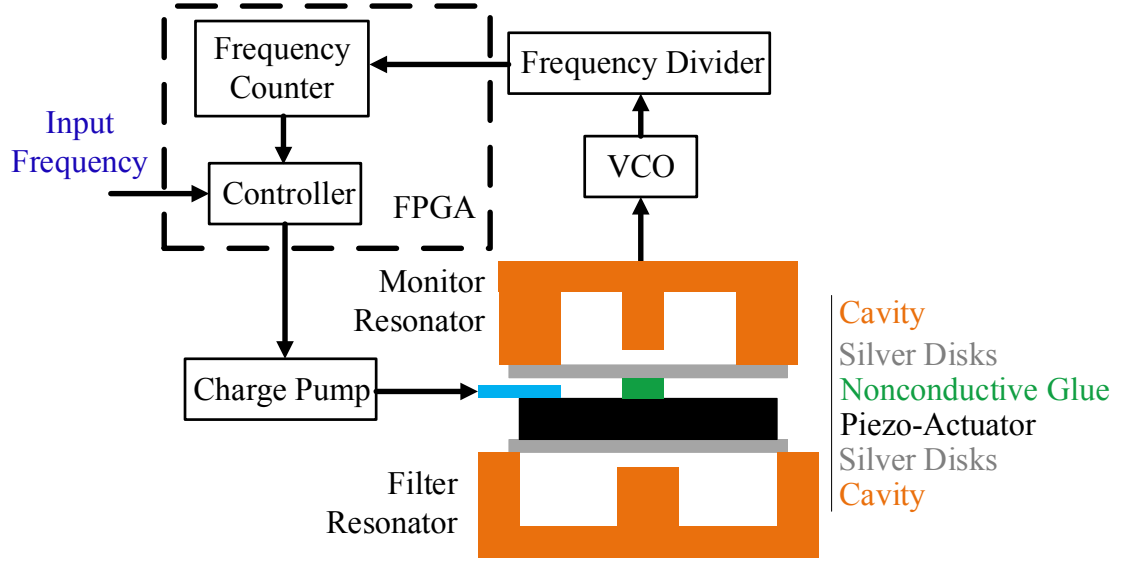
Fig. 4.4. Block diagram illustration of monitoring and control system [57].

Another evanescent-mode cavity resonator (monitoring resonator) is mounted on the top of the filter resonator using non-conductive glue. Two resonators share a piezoelectric tuner. This way the monitoring resonator frequency decreases whenever the filter resonator frequency increases and vice versa. Therefore sensing the frequency of the monitoring resonator reveals the frequency of the filter resonator. Also, the monitoring path is independent of filter path; thus the RF performance of the filter is minimally affected. A Colpitts oscillator is designed to generate the output frequency tone at the center frequency. Due to the speed limit of the FPGA, the output frequency from the oscillator circuit is divided. The binary ripple counter in the FPGA calculates the frequency. The control algorithm in the FPGA compares the sensed frequency with the desired frequency and updates the bias voltage through the charge pump.

The monitoring resolution can be represented as

$$Resolution = \frac{MD}{T},$$
(4.3)

where M is the ratio between the filter resonator frequency and the monitoring resonator frequency, D is the divisor of the frequency divider, and T is the control cycle time of the ripple counter in the FPGA [49]. There are trade-offs between the control resolution and other system parameters. The control resolution can be improved by decreasing the divisor, which requires faster FPGA or increasing the control cycle time, which will, in turn, slow down system response time.

4.2.4   Control Algorithm

In this application, resonator 1 always stays at the operating frequency. The frequency locations for resonator 2 that realizes the bandstop and the all-pass states are recorded in a calibration table. Therefore a calibration table that includes the resonator 1 center frequencies, the resonator 2 bandstop frequencies, and the resonator 2 all-pass frequencies is stored in a Matlab program that is used to send commands to the programmed FPGA. A sample calibration table is shown in Table 4.1.

It should be highlighted that the numbers in the calibration table correspond to the frequencies of the monitoring resonator.

4.3   FSL Design and Implementation

The demonstrated FSL is designed with 1.5 to 2 GHz tuning range and -40 dBm power threshold level. The absorptive bandstop-to-all-pass filter is designed and implemented with evanescent-mode substrate integrated cavity technology due to the high Q-factor of the resonators [54]. Figure 4.5 shows the HFSS model for the filter.

The top layer with a 50 Ω microstrip line source-to-load coupling is designed on a 0.508-mm thick Rogers 4003 substrate ($\varepsilon_r = 3.38$, $\tan(\delta) = 0.0027$). The cavities

Table 4.1.
Example Calibration Table for the FSL

F_C	Res1	Res2(BSF)	Res2(All-Pass)
[GHz]	[unitless]	[unitless]	[unitless]
...	...	...	...
1.60	19020	22960	22400
1.65	18600	22700	22000
1.70	18000	22200	21500
1.75	17600	21900	20900
...	...	...	...

are designed on a 1.524-mm thick Rogers 4003 substrate. Each cavity resonator is loaded with a post that creates a parallel capacitance with the upper cavity wall and can be tuned with piezoelectric tuners. The filter can theoretically achieve a tuning range from 1 to 2 GHz if the gap is tuned from 8 to 38 μm. However, due to the implementation limitations, the final tuning range is from 1.5 to 2 GHz. The filter couplings are realized through slots at the ground plane between the microstrip lines and the cavities. The angles of the slots determine the coupling values. Here, the angles are selected to be 68° for slot 1 and 52° for slot 2. The resulting k_1 is 0.2 and k_2 is 0.13, which satisfy the required condition to achieve an all-pass state (2.10). The pads on top of the coupling slots add shunt capacitance to the microstrip line to compensate the series inductance introduced by coupling slots. The design method and equivalent circuit models of the slots and pads are explained in detail in [**?**]. A via coupling that is located 4.5 mm away from the cavity center is designed to provide −18-dB coupling to port P for the implementation of the power detection. The unloaded Q-factor of resonator 1 is reduced from 440 to 340 due to this external
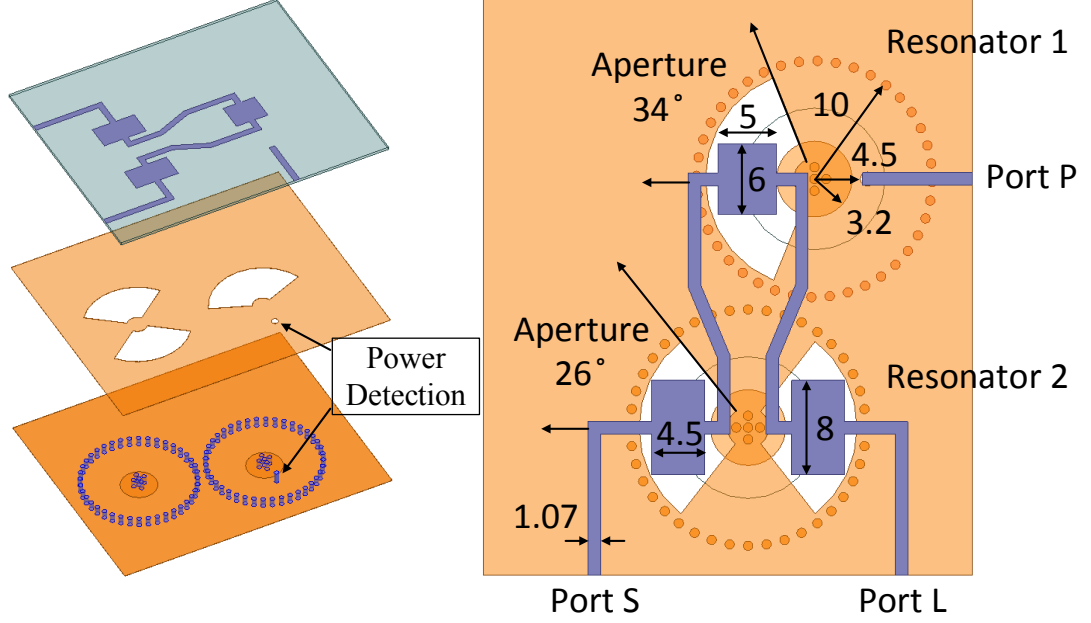
Fig. 4.5. HFSS simulation model and dimensions (in millimeters) of the proposed evanescent-mode cavity filter with a power detection port.

power coupling based on HFSS simulation. In order to keep the signal above the noise floor, a fixed 18-dB gain LNA (MAX2612) is used between port P and the power detector (LT5538). The comparator is implemented using the LM293 circuit from Texas Instruments.

The control loop resolution is selected based on simulations. Simulation results show that a resolution of 100 kHz (0.01%) gives a 50-dB attenuation level, and a resolution of 500 kHz (0.05%) gives 40-dB. Based on (4.3) and availability of commercial components, the ratio of filter frequency and monitoring frequency is designed to be 2, the divisor is set to 60, and the control cycle time is set to 1 ms. This way the control resolution is 120 kHz. Figure 4.6 shows the circuit schematic of the Colpitts oscillator in the feedback control loop.
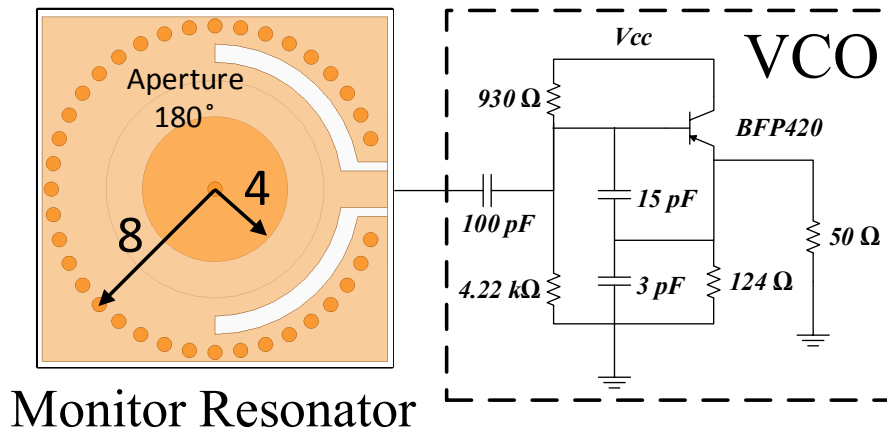
Fig. 4.6. Circuit schematic of Colpitts oscillator with dimensions (in millimeters). The components utilized are also shown.

The monitoring resonator with the 180-degree coupling aperture is designed to operate from 500 MHz to 1 GHz. A BFP 420 BJT is used to implement the Colpitts oscillator to operate across the whole tuning range. The frequency dividers are implemented using MC 12093 with a division of 6, and ICS 674 with a division of 10. The output of ICS 674 is a TTL signal, which can be recognized directly by FPGA. To be noted, the output of the Colpitts oscillator contains high-frequency harmonics. A low-pass filter can reduce these harmonics. In this work VLF-1000+/VLF-800+, coaxial filters from Mini-Circuits are used.

The complete assembled filter is shown in Fig. refassembled. The filter is assembled in a box so that it can be easily used.

4.4 Measurement Results

The fabricated FSL is measured for its three modes as well as long-term performance. The measurement setup is shown in Fig. 4.8.

Frequency measurements use the Agilent N5230C network analyzer, and power measurements use a single tone generator (Agilent E4433B) and a spectrum ana-
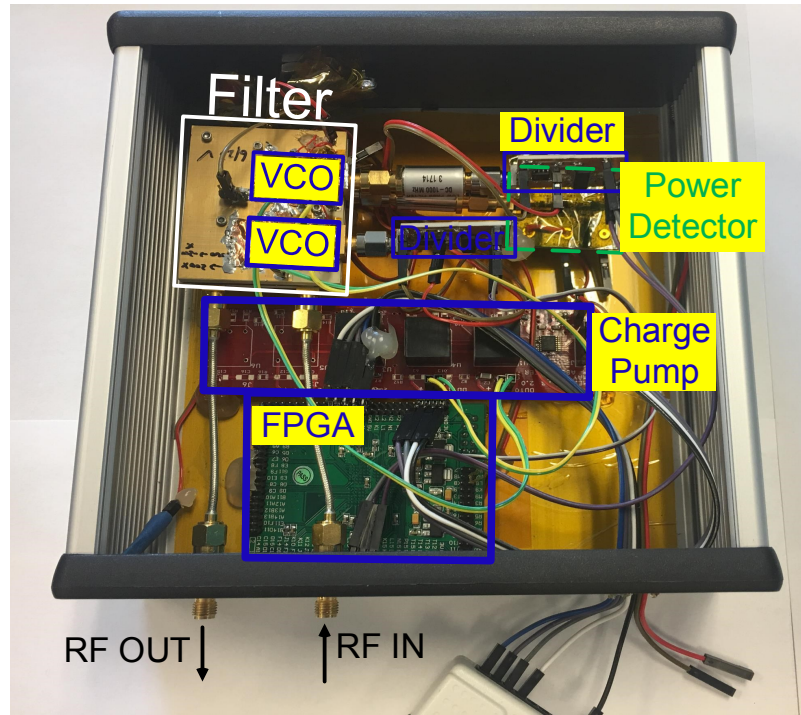
Fig. 4.7. Complete assembled filter in a box.

lyzer (Tektronix RSA3408A). The FSL is provided with a fixed 5-V bias for all the measurement. The following subsections discuss the measurement results separately.

4.4.1 User-Defined Bandstop Mode

The FSL in user-defined bandstop mode is measured with the Agilent N5230C network analyzer. In this measurement, the FSL is tuned to selected frequencies using a Matlab program with the calibration table shown in Table 1. As shown in Fig. 4.9, the FSL can present a measured notch of $45-55$ dB in its $1.5-2$ GHz tuning range. The measured 3-dB bandwidth is 7.8% at 1.5 GHz and increases monotonously to 11.0% at 2 GHz. The measured 10-dB bandwidth is 4.0% at 1.5 GHz and increases
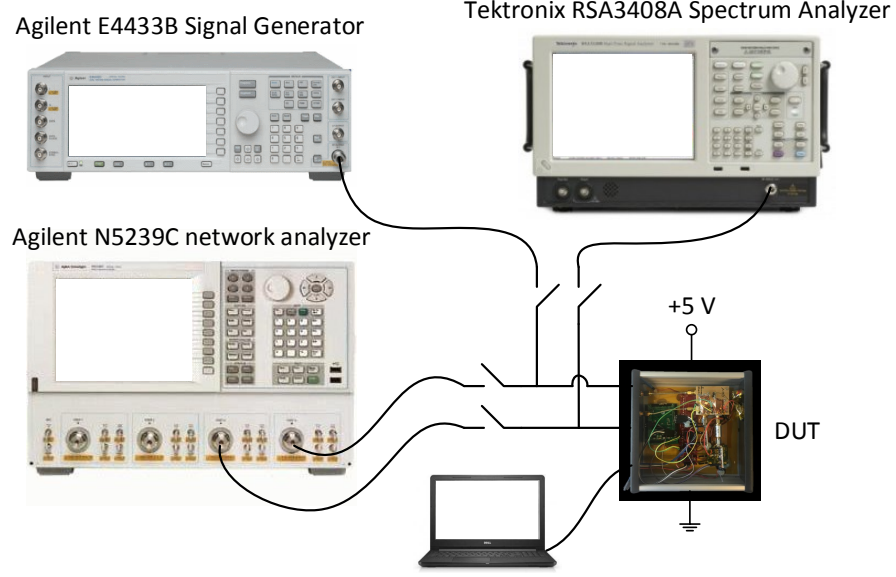
Fig. 4.8. Experimental setups for the demonstrated filter with manual switching between two setups (Frequency response and power response).

to 5.0% at 2 GHz. The measurement results agree with theoretical predictions of the notch depth (50 dB) based on the achieved control loop resolution.

4.4.2 All-Pass Mode

Figure 15 shows the measurement results for the fabricated FSL in its all-pass mode. The measured out-of-band insertion loss is less than 0.8 dB. The measured insertion loss is 3.1 dB at 1.5 GHz and is decreased to 2.84 dB at 2 GHz including the two SMA connectors and the associated connector-to-microstrip transitions. The green arrows indicate loss due to impedance mismatch (k_1 value) and finite Q-factor. The blue arrows emphasize loss due to finite Q-factor.
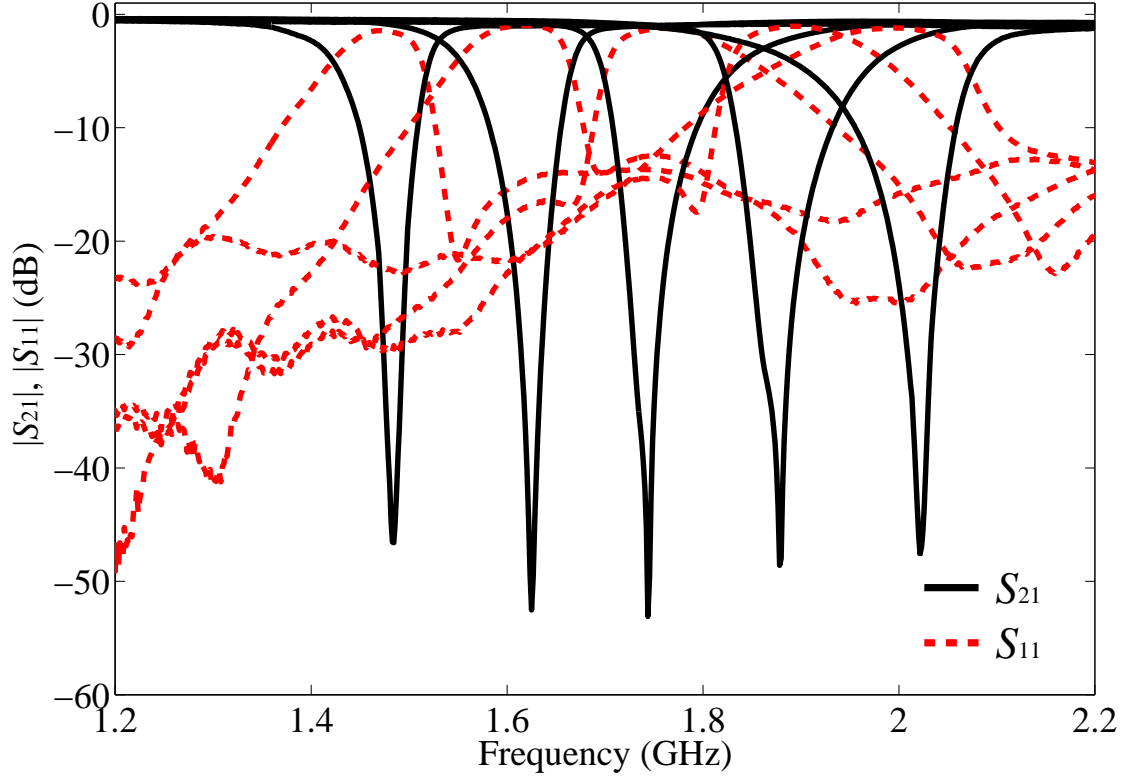
Fig. 4.9. Measured frequency response of the FSL in user-defined bandstop mode. The FSL presents a measured notch of 45−55 dB in its 1.5−2 GHz tuning range. 3-dB bandwidth is from 7.8% at 1.5 GHz to 11.0% at 2 GHz.

4.4.3 Power-Activated Mode

The FSL in power-activated mode is tested at 1.5, 1.625, 1.75, 1.875, and 2 GHz separately. In this test, the power threshold level is set to −40 dBm. The incident power at the selected frequency is swept from −50 to −35 dBm, and the output power level at that frequency is recorded from the spectrum analyzer with 1 dBm increment. The measurement results are plotted in Fig. 4.11. The FSL demonstrates more than 40 dB isolation when the incident power is higher than the threshold power, and less than 3.1 dB when the incident power is smaller than the threshold power. The power
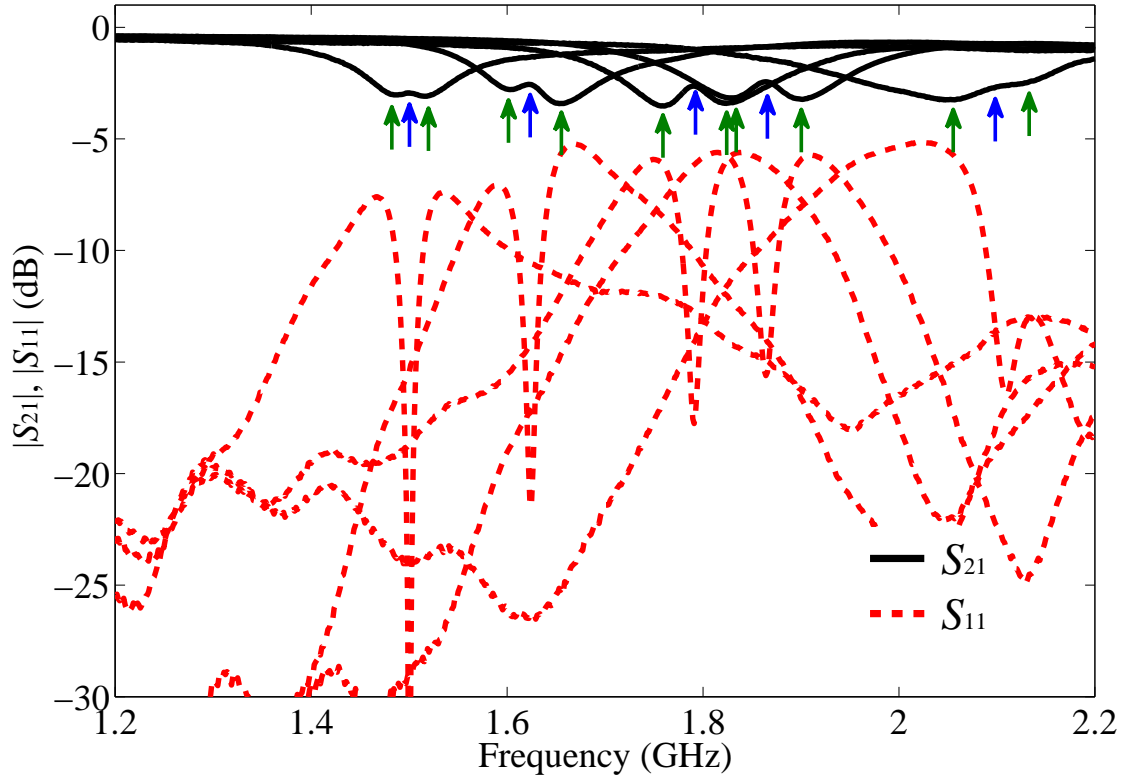
Fig. 4.10. Measured frequency response of FSL in all-pass mode. The minimum insertion loss is 2.84-dB and maximum is 3.08-dB.

threshold has $\pm$ 2 dBm variation, and this is due to the variance of the external coupling k_3 and gain of the LNA. It should be highlighted that the lower boundary of the power threshold level in this application is mainly limited by the noise floor, which is around -50 dBm. The level of the noise floor is determined by the amount of cross-talk/leakage from the monitoring resonator's VCO, which operates at a power level of about 8 dBm. The cross-talk/leakage could be further reduced by shielding the VCO circuit.
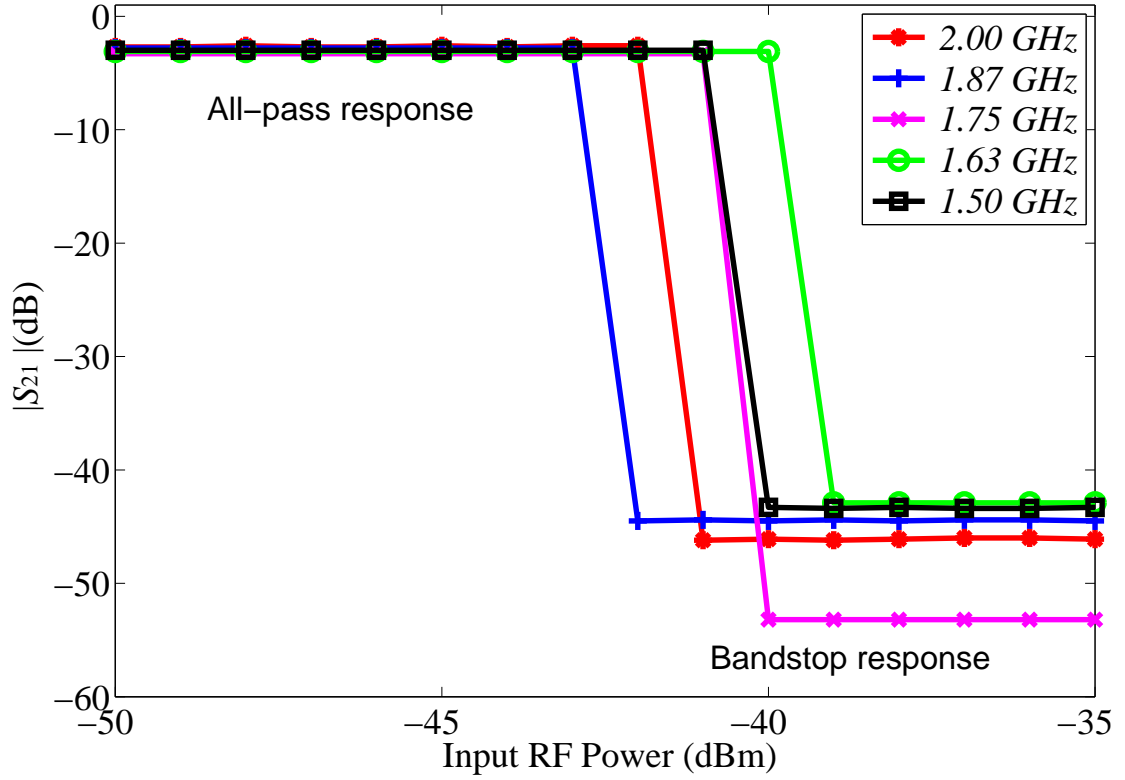
Fig. 4.11. Measured RF input power vs. isolation level at 1.5, 1.625, 1.75, 1.875, and 2 GHz respectively with 1 dBm step size from -50 to -35 dBm. The FSL demonstrates more than 40-dB isolation in bandstop state and less than 3.1 dB in all-pass state.

4.4.4 Long-Term Test

The long-term test has been performed on the FSL, and the results are presented in Fig. 17. In this test, the FSL is tuned to a constant frequency (1.75 GHz), and the isolation level at that frequency is recorded every 10 minutes for 9 hours. As shown in Fig. 4.12, the attenuation level slightly varies with time but is always larger than 40 dB. The test was stopped at 9 hours with not observed failures.
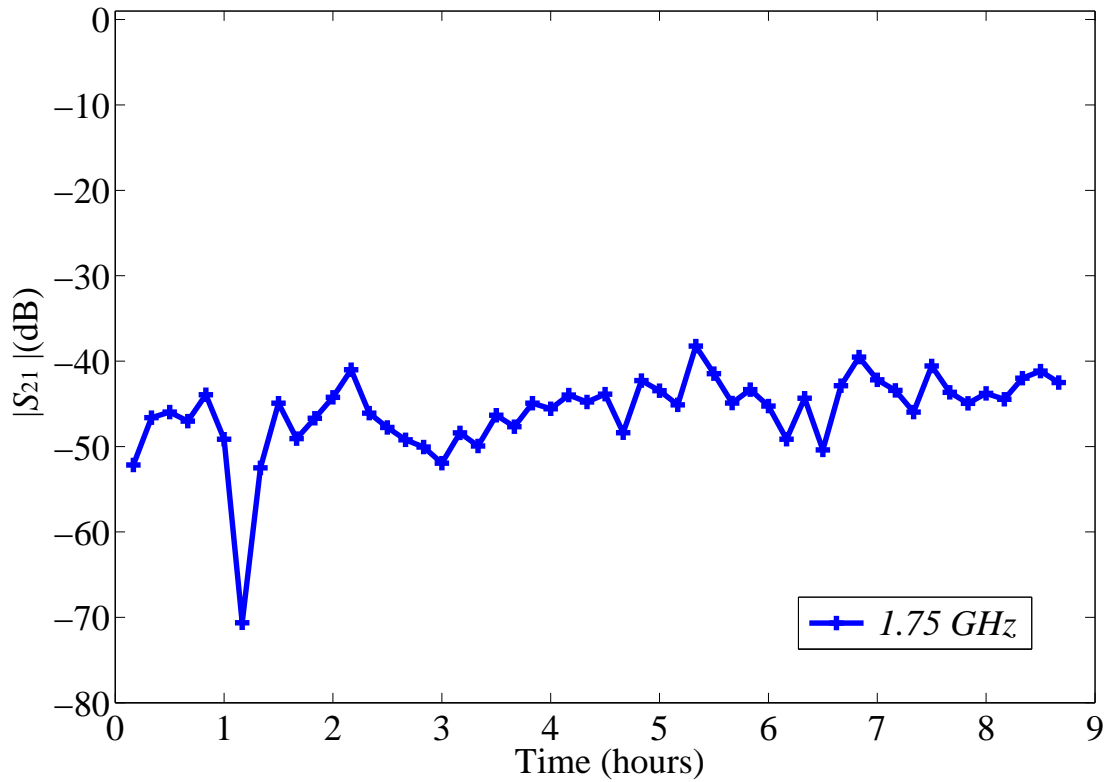
Fig. 4.12. Measurements of long-term test. The fabricated FSL locates its notch at 1.75 GHz for 9 hours. The figure plots the variation of notch level at 1.75 GHz across time.

4.4.5 Comparison with the State of Art

A quantitative comparison between the proposed FSL and several existing state-of-the-art, as shown in Table 4.2. It can be seen that the FSL presented in this report has the highest attenuation level. Also, the proposed FSL has the widest tuning range of the power threshold level from −50 to +8 dBm.

Table 4.2.
Comparison of Proposed FSL to State-of-the-Art

Ref.	Tech.	Topology	Frequency Range [GHz]	Max. Attn. [dB]	Power Threshold [dBm]
[38]	Nuclear	BSF	1.2 kHz	30	-42
[39]	YIG	BSF	10 MHz	20	3.2
[40]	YIG	Stripline	2$-$8	30	0
[41]	YIG	Stripline	2.5$-$5.3	11	0
[43]	YIG	Stripline	0.4$-$0.8	40	-27
[46]	Diode	Parametric	0.85	13	0
[47]	Diode	Parametric	2	18	-10
[50]	Diode	BSF	2.2	35	0
[53]	Diode	BPF	1$-$1.3	22	16$-$33
This Work	Cavity	BSF	1.5$-$2	45	-50$-$8

5. OPTIMIZATION OF ROBUSTNESS FOR MINIATURE AND TUNABLE CAVITY FILTERS

As the number of communication bands grows and the RF environment gets more complex with a crowded spectrum, tunable communication systems become a promising solution [59]. In such a system, filters are desired to be transfer-function-adaptive, high-quality, of wide tuning, linear, and reliable. Among the existing tunable filter technologies, the evanescent-mode cavity filter technology has demonstrated the potential to meet most of these critical features [60]. For decades, the filter reconfigurability has been extensively researched and has demonstrated excellent results beyond center frequency and bandwidth tuning [23, 26–28, 61–107]. While these results are exciting, for in-field operations, robustness becomes more important.

The control of tunable filters has been studied extensively in [56, 57]. A feedback control loop is designed and implemented to monitor and control the resonator frequency. Two cavity resonators, the one of interest and a reference one, are stacked together, sharing a common membrane. By this way, the filter's resonator frequency is revealed by monitoring the reference resonator frequency. This control loop has been demonstrated in several applications with controlled resonator/filter responses [55, 105, 106].

However, there have been no systematic studies of how to make these filters robust for real-world applications. As different controlled actuators have different resolutions, tuning variations, thermal coefficients, etc. these studies need to be conducted so that in-field performance can be guaranteed.

This chapter presents, for the first time, the study of robustness for cavity applications. Three implementations and five designs of resonators are presented and compared in Section II. The trade-offs among robustness, unloaded resonator Q-factor, and volume are discussed in detail. In Section III, the procedure to design and
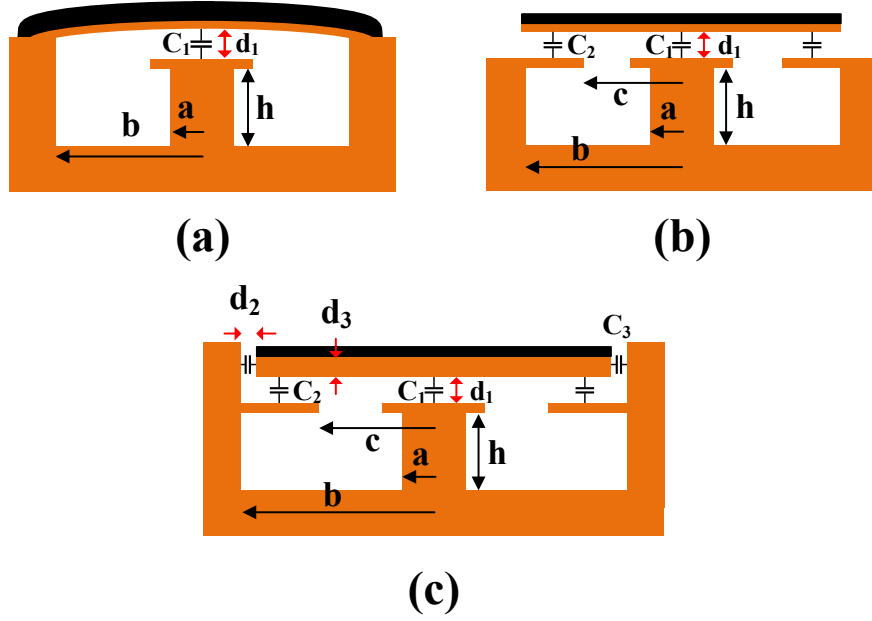
Fig. 5.1. Three different cavity resonator designs: (a) a contact design, (b) a contact-less design that improves robustness at the cost of resonator Q-factor, and (c) a novel contact-less cavity resonator with extended side-wall (ESW) that improves the Q-factor.

optimize the resonator and filter for cavity applications is proposed and explained. There are four steps to this procedure: first, setting the filter specifications; second, determining the minimum post gap needed based on the sensitivity of the filter topology and the maximum drift of the actuator; third, designing the resonator couplings based on the Q-factor needed and the minimum post gap; lastly, implementing the filter accordingly. A quasi-absorptive bandstop-to-all-pass filter from [35] is redesigned as a demonstration. The filter is then measured for long-term stability, repeatability, RF power handling, vibration, and temperature sensitivity. These measurement results show great promise for the optimization of robustness for cavity filters and applications.

5.1 Contact and Contact-less Resonator Designs

In this section, three cylindrical evanescent-mode cavity designs with different implementations of the membranes are presented and comparatively studied. The physical structures of the resonators are illustrated in Fig. 5.1, where (a) is the contact design, (b) is the contact-less design, and (c) is the contact-less design with extended side-wall (ESW). The lumped-element models, as well as the trade-offs, are discussed in the following subsections. Five designs with the same tuning range are presented and compared for unloaded Q-factor, frequency variation due to gap error, RF power handling, and volume.

5.1.1 Contact Design

The contact design, shown in Figure 5.1(a), is well-studied and the most commonly used cavity resonator design [23, 26–28, 61–107]. Modified from a cylindrical cavity resonator, the top of the cavity is replaced with a tunable membrane. A post or a group of posts are implemented in the middle of the cavity to suppress the electrical field within. Thus, an additional mode at a frequency much lower than the TE and TM modes is formed. By changing the post gap, d_1, the effective capacitance of the resonator changes, and therefore so does its center frequency. The lumped-element model is a shunt LC resonator, where the inductance of the model is the coaxial inductance of the cavity given by

$$L_0 = \frac{\mu_0 h}{2\pi} ln(\frac{b}{a}).$$ (5.1)

The total capacitance is the parallel sum of the coaxial capacitance C_0 and the post capacitance C_1. The coaxial part can be represented as

$$C_0 = \frac{2\pi\epsilon_0 h}{ln(b/a)}.$$ (5.2)

The post capacitance can be represented using a nonlinear, large-gap capacitor model [109]

$$C_1 = \frac{\epsilon_0 \pi a^2}{d_1}[1 + \frac{2d_1}{\pi a} ln\frac{8\pi a}{ed_1} + (\frac{d_1}{\pi a} ln\frac{d_1}{8\pi a})^2],$$ (5.3)

where e is the natural number.

The unloaded Q-factor is given by

$$\frac{1}{Q_{total}} = \frac{1}{Q_c} + \frac{1}{Q_d} + \frac{1}{Q_r} \tag{5.4}$$

where Q_c is due to the conduction loss, Q_d is due to the dielectric loss of the substrate, and Q_r is due to radiation loss. The conduction loss in the cavity can be approximated using a quarter wavelength coaxial resonator where Q_c is defined as

$$Q_c = 2\omega W_e / P_c. \tag{5.5}$$

The energy stored in the cavity is given by

$$W_e = \frac{\varepsilon_0 \varepsilon_r}{4} \int_0^h \int_0^{2\pi} \int_a^b \frac{V_0^2}{(lnb/a)^2} \frac{1}{r} (2A\sin kz)^2 \, dr \, d\phi \, dz \tag{5.6}$$

where W_e is the time-average electric field energy in the cavity, A is a normalization factor, k is the propagation constant, and V_0 is the voltage difference between the post and the membrane. The loss due to current conduction is given by

$$P_c = \frac{R_s}{2} \int_0^h \oint_a^b \frac{Y_0^2 V_0^2}{(lnb/a)^2} \frac{1}{r} (2A\sin kz)^2 \, dr \, d\phi \, dz + \frac{R_s}{2} \int_0^{2\pi} \int_a^b \frac{Y_0^2 V_0^2}{(lnb/a)^2} \frac{1}{r} (2A)^2 dr \, d\phi \tag{5.7}$$

where R_s is the sheet resistance and Y_0 is the free space admittance. Solving (5.6) and (5.7) and plugging into (5.5), Q_c is given by [108]

$$\frac{1}{Q_c} = \sqrt{\frac{f\varepsilon}{\pi\sigma}} (4 + \frac{2h(\frac{1}{a} + \frac{1}{b})}{\log(\frac{b}{a})}). \tag{5.8}$$

The dielectric loss in the cavity is given by

$$P_d = \frac{1}{2} \int_0^h \int_0^{2\pi} \int_a^b J * E^* \, dr \, d\phi \, dz. \tag{5.9}$$

Then, by solving in a similar method as (5.8), Q_d is given by

$$\frac{1}{Q_d} = \frac{2\omega W_e}{P_d} = \frac{\varepsilon}{\varepsilon''} = \frac{1}{\tan\delta}. \tag{5.10}$$

The radiation loss, Q_r, in the contact design is insignificant.

5.1.2   Contact-Less Design

The contact-less design, shown in Fig. 5.1(b), was introduced to simplify assembly and improve robustness [110]. In the contact-less design, the membrane is suspended, and tuning is achieved by moving the whole membrane rather than by deflection. Thus, the membrane can be implemented with rigid metals. The contact-less design has a couple of advantages over the contact design, all leading to a more robust design. First, the tuning range is practically larger without the limitations of deflection. Second, the thermal expansion from bonding materials between the cavity and the membrane is eliminated. The contact-less cavity model is still a shunt LC resonator, where its total capacitance is the parallel sum of the coaxial capacitance (C_0) with the series sum of the post (C_1) and ring capacitance (C_2). The ring capacitance, C_2, can be represented using a thick planar ring capacitor model [111]

$$C_2 = \frac{2\epsilon_0 \pi (b^2 - c^2)}{d_1}.$$

(5.11)

5.1.3   Contact-Less Design with Extended Side-Wall (ESW)

The contact-less design suffers from poor unloaded Q-factor at large gaps. The extracted unloaded Q-factors of several cavity resonators are simulated in HFSS and compared in Fig. 5.2. In an octave frequency range, the unloaded resonator Q-factor drops more than 70% for the contact-less design, compared to 28% for the contact design. To solve this problem, a side-wall is implemented on the contact-less cavity, as shown in Fig. 5.1(c), to reduce the gap between the tunable membrane and ground. The unloaded Q-factors with three different side-wall gaps are plotted with dashed lines in Fig. 5.2. Now, the unloaded Q-factor drops less than 45% with a 1 mm side-wall gap and less than 33% with a 100 μm side-wall gap, meaning that the ESW design has better performance than the regular contact-less design. However, the Q-factor of the ESW design is approximately 10% lower than the contact design with a 100 μm side-wall gap. The lumped-element model for the contact-less design with

ESW is similar to the contact-less design except there is an additional capacitance, C_3, which can be given by

$$C_3 = \frac{2\pi\epsilon_0 d_3}{ln[b/(b-d_2)]}.$$

(5.12)

Meaning that the resonator frequency is given as

$$f = \frac{1}{\sqrt{L(C_0 + \frac{C_1(C_2+C_3)}{C_1+C_2+C_3})}}.$$

(5.13)
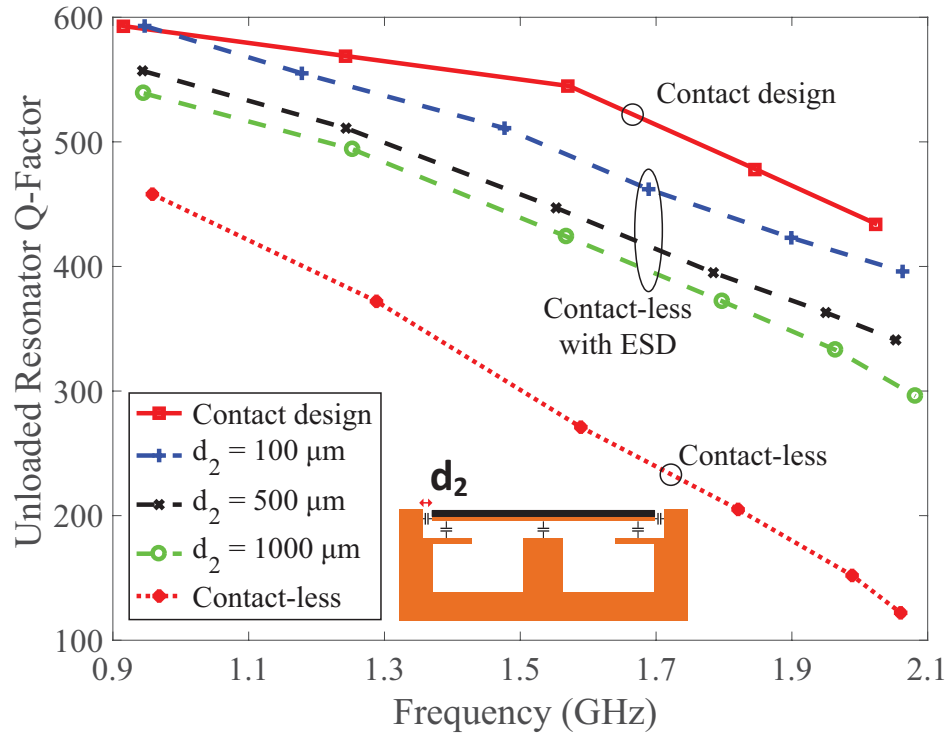
Fig. 5.2. Physical structures of three cavity resonator designs: (a) the conventional contact design, (b) the contact-less design, and (c) the contact-less design with extended side-wall.

5.1.4 Comparisons for Robustness

In this subsection, five cavity resonator designs with different post gap range and membrane implementations are presented. For convenience, they are named from

design I to V with ascending post gap sizes. Designs I, II, and IV use the contact design, while designs III and V use the contact-less design with ESW, where the side-wall gap, d_2, is 200 μm. Table 5.1 summarizes the design parameters referencing Fig. 5.1. The contact-less design is omitted for the reasons stated in the previous subsection.

Table 5.1.
Dimensions of the Cavity Resonators

Design	I	II	III	IV	V
Category	Contact	Contact	ESW	Contact	ESW
d_1 (μm)	10-50	50-350	50-350	150-2400	150-2400
b (mm)	10	8	8	10	10
a (mm)	3.3	5.3	5.3	6.7	6.7
h (mm)	1.5	4	4	6.35	6.35
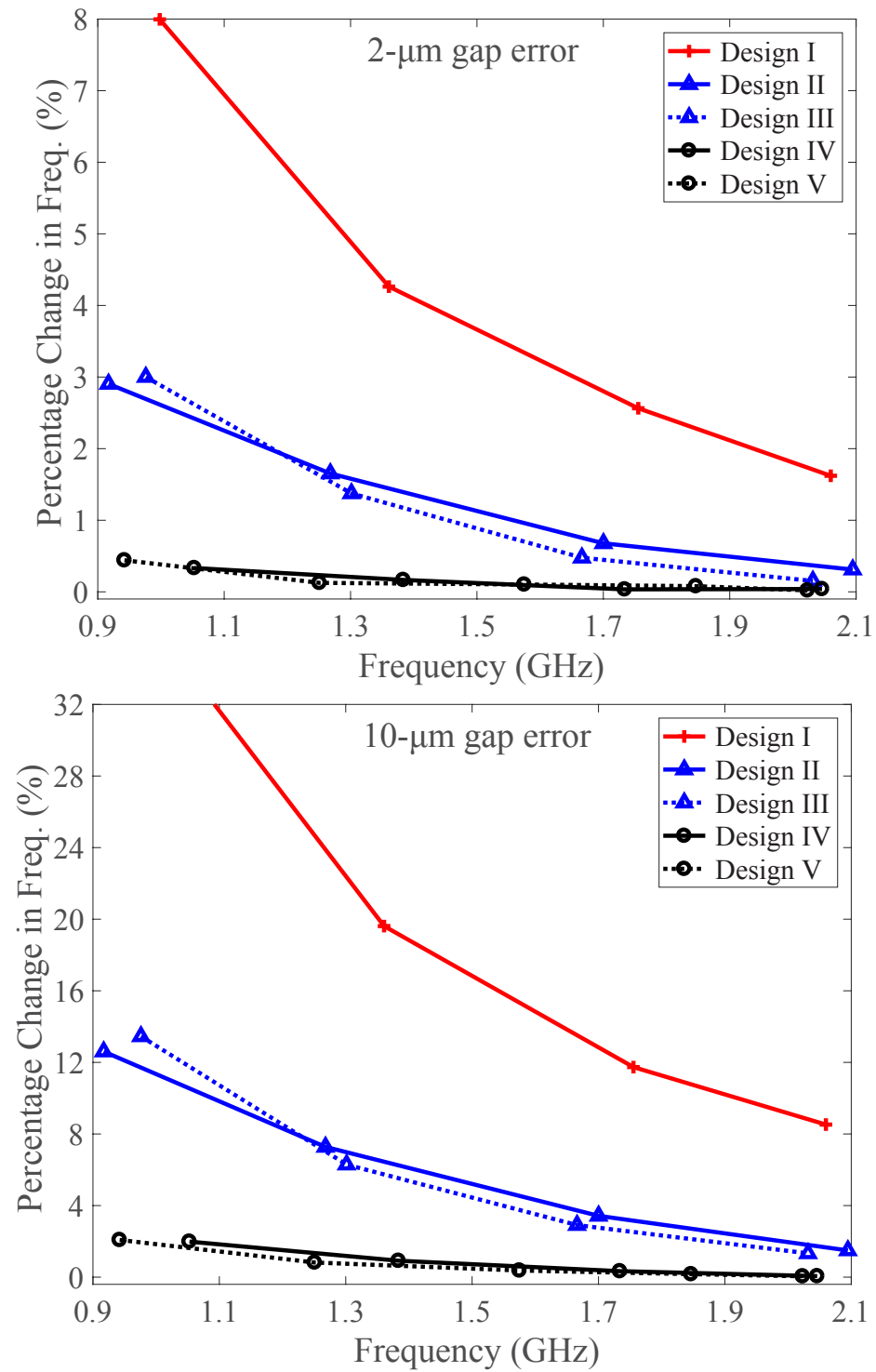
Fig. 5.3. Variation of frequency due to gap error of 2 μm (top) and 10 μm (bottom) as a function of center frequency.

Frequency Susceptibility

In real-life applications that demand sustainable performance in a range of environments, a filter's dynamic behavior needs to be understood. Whether the system is subjected to environmental vibrations or extreme temperatures or even finite actuator control, there will be an error in the post gap, thus shifting the center frequency and degrading the in-band performance. These deviations are shown in Fig. 5.3 with a 2 and 10 μm gap error. It is clear that designs IV and V are the least susceptible to a deviation in their post gap since a small deviation over a large post gap will not vary the capacitance much. For designs IV and V, the maximum error is 0.5% with a 2-μm gap error and 2.1% with a 10-μm gap error. What should be noted is the severity of the frequency shift as a function of gap size and that a larger post gap will be the least susceptible to vibrations and temperature-related deviations.

In reality, however, it is hard to achieve the needed 2-mm deflection from the membrane without corrugation or bending in design IV, the contact case. The thermal expansion from the bonding materials between the membrane and the cavity may significantly affect the robustness of the resonators with the contact design. This leads to the ultimate conclusion that the contact-less design with ESW is the optimum choice when considering both RF performance and robustness.

Unloaded Q-Factor

For bandstop filters, higher isolation is desired to reject interference bands while for bandpass filters, a lower insertion loss is preferred. Thus, for both cases, the Q-factor is important when designing a cavity filter. The unloaded resonator Q-factors across a wide post gap range from 10 to 5000 μm for the five designs are extracted and shown in Fig. 5.4. As can be seen, there is an optimal post gap range for Q-factor, which occurs in-band (1-2 GHz) for designs II and III, the designs with a mid-sized post gap. At the low-frequency end, the post gap is very small and therefore the Q-factor is decreasing for design I. At the high-frequency end, the post gap is very

big and therefore the Q-factor is also decreasing for designs IV and V due to radiation losses. For all the designs, the Q-factor is above 380. These results are obtained from HFSS using a Rogers TMM 3 substrate ($\varepsilon_r = 3.27$, $\tan(\delta) = 0.002$) with vias as the cavity's sidewalls. It should be noted that at high frequencies, the coupling values are larger with the same coupling structure, and thus, yield a wider bandwidth. This will compensate for the insertion loss coming from a lower Q-factor. There is less than 10% difference between the contact designs and the contact-less designs with ESW (design II vs. III and IV vs. V).
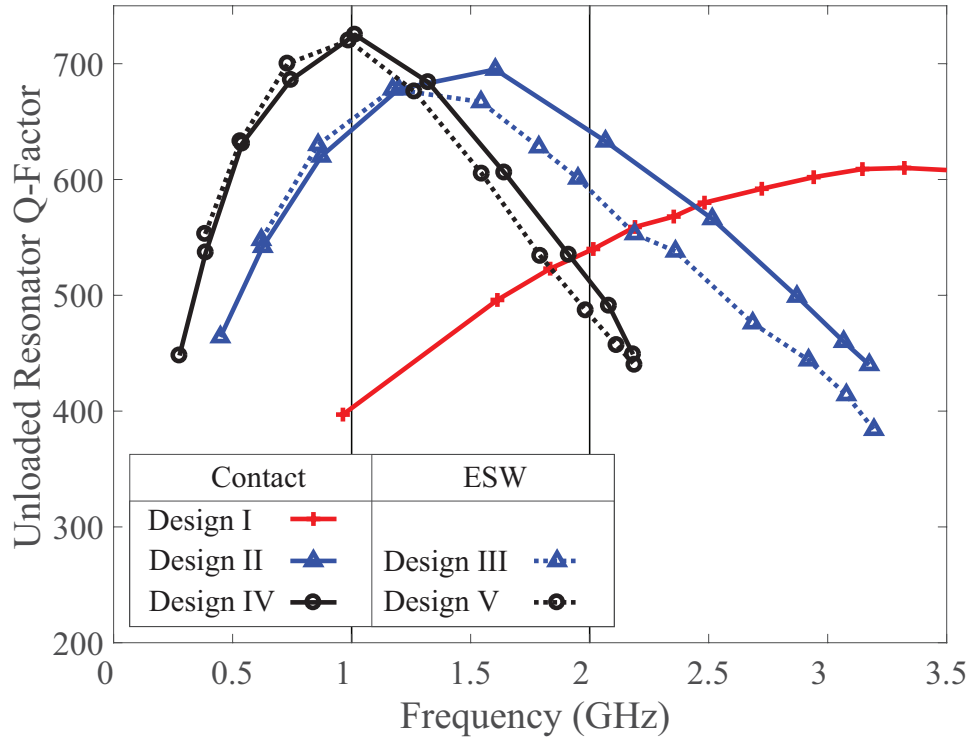
Fig. 5.4. Simulated unloaded Q-factor versus frequency for all the designs with a post gap range from 10 to 5000 μm.

Maximum Power Handling

Today's systems must be able to handle strong interferers without incurring damage. For this reason, the power handling capabilities for all five designs have been

evaluated in HFSS by applying an RF input with varying power levels. The magnitude of the electric field is plotted on the membrane and around the post area for a 700-W input for designs IV and V as seen in Fig. 5.5. This illustrates the magnitude of the electrical fields on the post, the side-wall, and on the membrane for designs IV and V. The electric field is concentrated uniformly between the post and the membrane for both designs, and also between the membrane and the side-wall for design V. Here, the membrane is implemented with a copper disk of 0.5-mm thickness. The gap between the side-wall and the membrane is 200 μm. When the electric field on the post is 7.9 V/μm [113,114], resulting in AC air breakdown, that signifies its maximum power handling capability. The analytical solution to predict the maximum power handling capability is detailed in [113]. The maximum power handling capability for each design is shown in Table 5.2. It is evident that for higher power applications, a larger post gap is desirable as this reduces the potential for break down.
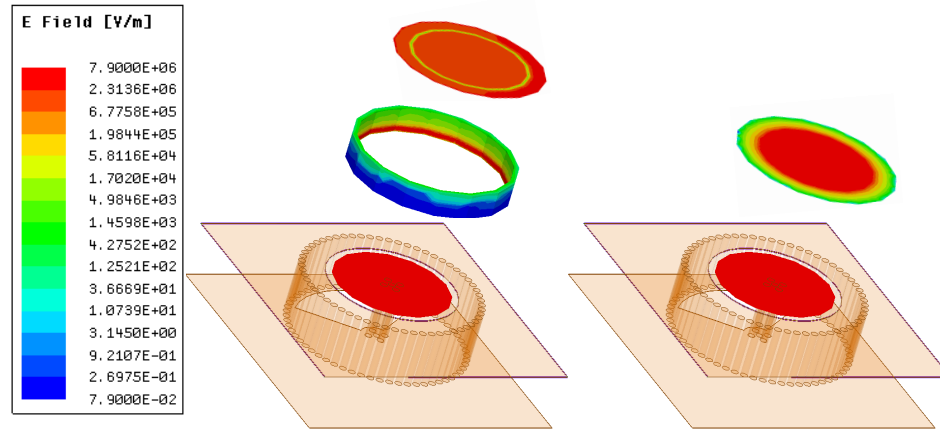
Fig. 5.5. Exploded view of the magnitude of electric field distribution on the post, the side-wall, and the membrane for design V (contactless design with extended side-wall, left) and IV (contact design, right) at its minimum post gap with 700-W input.

Volume

The volume of the resonator is directly related to the post gap. Therefore, a more robust design requires a larger resonator volume. For the same post gap, the resonator with ESW design is 50% larger than the contact design. This is due to the implementation of the side-wall.

Table 5.2.
Performance Summary of the Cavity Resonators

	I	II	III	IV	V
Gap (μm)	10-50	50-350	50-350	150-2400	150-2400
Q-factor	403-553	499-571	517-553	426-593	380-586
Freq. error (2μm) (%)	1.6-8.0	0.3-2.4	0.15-3	0.04-0.3	0.02-0.4
Freq. error (10μm) (%)	8.5-36.3	1.5-12.6	1.3-13.5	0.06-2	0.05-2.1
Max. Power (W)	1.5	41	60	700	700
Vol. (mm^3)	118	201	302	499	748

Summary

Although the contact design is slightly better than the ESW design in terms of Q-factor and form factor, there are some practical limitations for the contact design. In application, the contact design cannot realistically achieve the post gap distances

required. Additionally, the fatigue on the metal membrane leaves it more prone to deviations. For these reasons, only the ESW design will be considered.

The discussed properties are summarized in Table 5.2. Designs IV and V have a smaller frequency deviation due to the gap error. They also show better power handling capability. On the other hand, at the high-frequency end, the Q-factors of designs IV and V are approximately 26% less than that of designs II and III, the designs with a mid-sized post gap, with a volume 2.5 times larger. Design I has the smallest volume. In summary, there is a design trade-off between the robustness and both the Q-factor and the resonator volume. This paper focuses on the optimization of robustness. Therefore, the frequency variation is the most critical factor to consider. The following section presents a procedure to find out the minimum post gap required for robustness. The resonator designed with this minimum post gap will maximize the Q-factor and minimize the volume.

5.2 Design and Optimization Procedure

In this section, a design procedure to optimize the robustness of any filter is presented and discussed. This section presents a generic procedure while concurrently providing a specific example. In summary, the steps include: first, setting the filter specifications; second, determining the minimum post gap needed based on the sensitivity of the filter topology and the maximum drift of the actuator; third, designing the resonator couplings based on the Q-factor needed and the minimum post gap; lastly, implementing the filter accordingly. A more detailed flowchart for both the specific and the generic case can be seen in Fig. 5.6.

5.2.1 Filter Specifications

A wide variety of filters may be implemented using the methodology proposed in this paper. The user must determine certain filter specifications, however, before applying the procedure prescribed in Fig. 5.6. This includes the filter type, desired
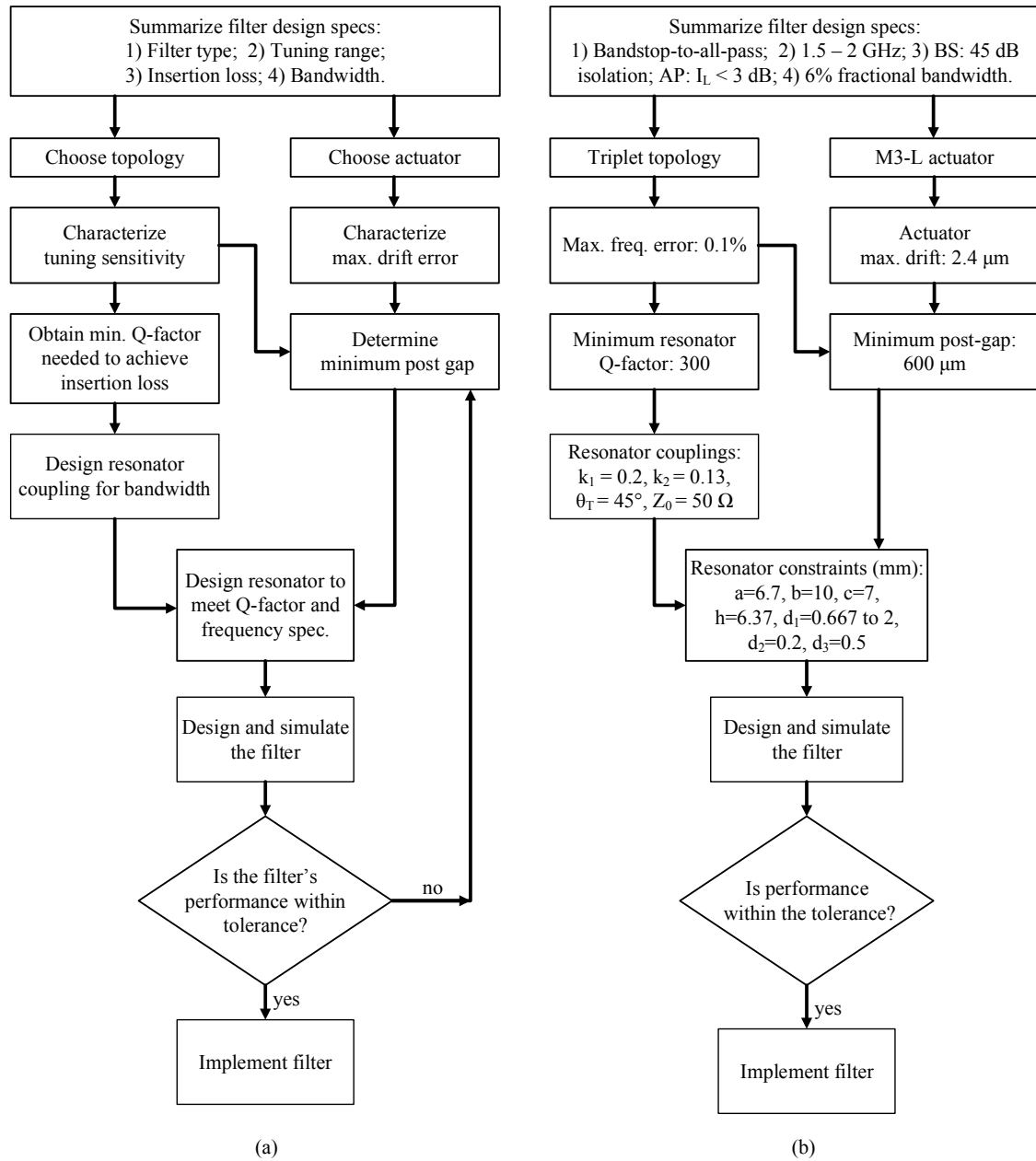
Fig. 5.6. Design and optimization flowchart of a robust cavity resonator filter for (a) a general case and (b) the specific case for this paper.

tuning range, acceptable insertion loss, and bandwidth. Additionally, the user must select a topology and an actuator.

As a design example, the filter from [35] is redesigned and optimized for robustness. The filter's specifications can be seen in Fig. 5.6(b). To reiterate, the filter is bandstop-to-all-pass with a 1.5 to 2 GHz tuning range while maintaining 45 dB of isolation for the bandstop mode and less than 3 dB of isolation in the all-pass mode. The fractional bandwidth is selected to be 6%. The tuning sensitivity mainly depends on the filter topology and, in general, absorptive topologies are more sensitive than conventional ones, which is why a triplet absorptive topology is used in the demonstration in this paper. The actuator is selected to be the commercial M3-L as its compact size provides an in-house control loop and has a wide tuning range, up to 6 mm. From [35], a resonator with unloaded Q-factor above 300 will satisfy the all-pass insertion loss specification.

5.2.2 Minimum Post Gap

The post gap is the key to ensuring that the filter's performance will not deviate from the specifications either over time or while in use. For this reason, and the reasons given in section II, the gap must be large enough to support the anticipated deviations while also providing a high Q-factor. Both the sensitivity of the chosen topology and the drift of the chosen actuator needs to be understood.

Characterize Tuning Sensitivity of Topology

The tuning sensitivity of a topology is defined by how much the RF performance is degraded as the tuning error increases. In other words, the sensitivity simulation suggests how much tuning error can be tolerated in order to meet the specifications set forth for insertion and return loss.

For the demonstration, the isolation at the center frequency as a function of tuning error for both the conventional and absorptive topology is plotted in Fig. 5.7. The
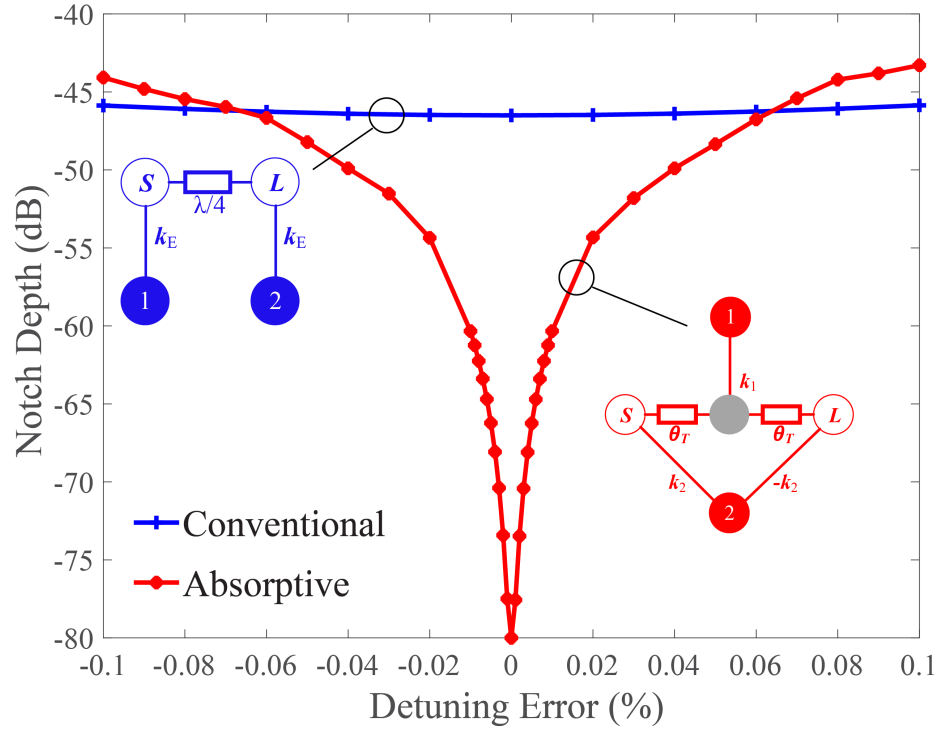
Fig. 5.7. Plot of notch depth versus percentage error in tuning for conventional and absorptive bandstop topologies. Resonator Q-factor is 300 in the simulation. Absorptive topology can achieve higher isolation but is more sensitive to detuning error.

results are obtained from simulations in Advanced Design Systems (ADS) with an unloaded resonator Q-factor of 300 at 1.5 GHz. To maintain isolation of more than -45 dB for the absorptive topology, only a percentage error of $\pm 0.1\%$ can be tolerated.

Characterize Maximum Drift of Actuator

Due to finite actuator control and sensing limits, the actuator's position may vary over time. This drift needs to be documented so that the post gap can be designed to enable the filter to meet the desired specifications. In essence, this step is to characterize by how much the actuator deviates.

In this paper, the M3-L actuator is selected rather than the piezo-actuator which has been previously used in many cavity applications due to its several advantages,
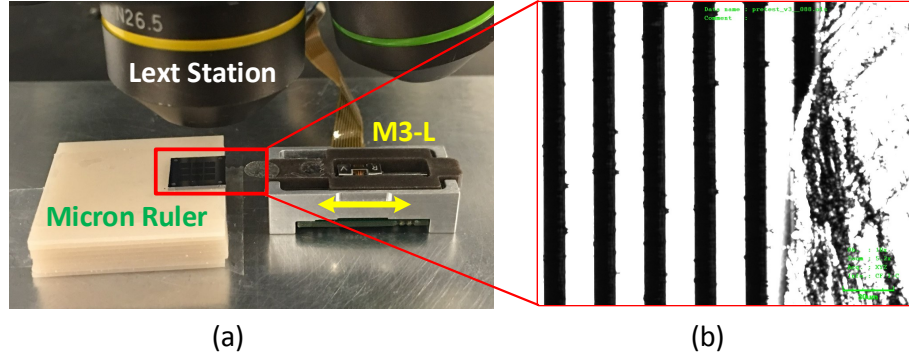
Fig. 5.8. (a) Measurement setup for the characterization of the M3-L actuator with Lext and a micro-ruler on silicon wafer. (b) Illustration of an example measurement.

mainly cost and availability. The travel distance of the M3-L actuator is 6 mm, which is ideal for the large post gap cavity designs for robustness, rather than 40 μm afforded by a piezo-actuator. Furthermore, this is all housed in a compact structure (28 by 13.2 by 7.5 mm) that contains the control loop while the piezo's is external. However, the M3-L's built-in control loop's resolution is 0.5 μm while the piezo allows for nanometer-resolution control [56, 57].

Both of the control loops for the M3-L and the piezo-disks are indirect controls. The M3-L senses its actuator position to control the frequency while the piezo monitors the frequency of a reference resonator that shares a membrane with the main resonator, as it is stacked on top. A calibration table is used to record and recall the frequency-position relation to realize in-field operation without network analyzers. However, when this relation differs or when there is an error in position sensing, the resonator frequency drifts. For cavity resonators tuned by actuators, measuring the long-term drift of the actuator can predict this error. With careful design, this error can be controlled within an acceptable margin by designing for a larger post gap.

The long-term drift of the M3-L actuator is characterized under the laser scanning microscope as shown in Fig. 5.8(a). A silicon wafer with etched lines is used as a
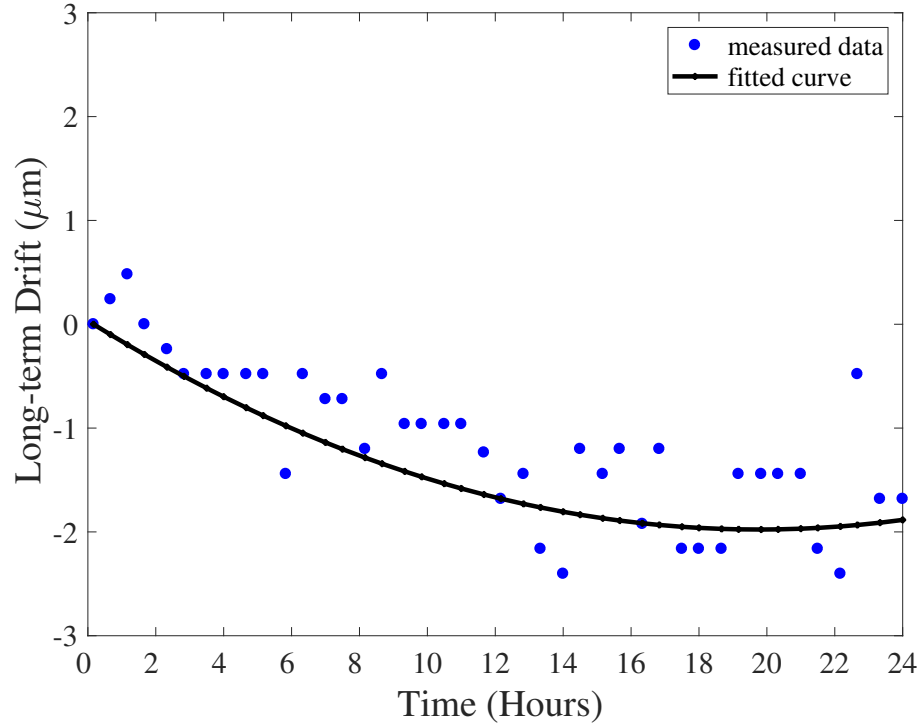
Fig. 5.9. Long-term drift of the M3-L actuator over 24 hours. Maximum drift is 2.4 μm.

micro-ruler to measure the position of the actuator pin. The tested M3-L actuator is mounted on the base with screws so that motor actions will not contribute to the drift. An illustration of the measurement is shown in Fig. 5.8(b). The measurement data is processed and plotted in Fig. 5.9 with a fitted curve. It is shown that the actuator starts to drift at the beginning and settles after around 20 hours. The maximum drift is approximately 2.4 μm.

Calculate Minimum Post Gap

The actuator drift error measured needs to be translated to frequency deviation of the topology. This is done to calculate the minimum post gap such that the maximum deviation of the actuator provides the maximum acceptable frequency deviation that can be tolerated. The resonator frequency can be calculated as

$$f = \frac{1}{2\pi\sqrt{LC}} = \frac{1}{2\pi\sqrt{L\frac{\epsilon\epsilon_0\pi a^2}{d_0+d_1}}} \propto \sqrt{d_0 + d_1}, \tag{5.14}$$

where d_1 is the tunable post gap and d_0 is the equivalent gap representing non-tunable capacitors, including the coaxial capacitance. Then d_0 can be estimated to be the same as d_1 to allow for the wide tuning range. The frequency variation due to a post gap error is then given by

$$\frac{f(1+\Delta)}{f} = \frac{\sqrt{d_0 + d_1 + E}}{\sqrt{d_0 + d_1}}, \tag{5.15}$$

where Δ is the maximum allowed frequency error for the filter topology and E is the maximum drift of the actuator.

Since the actuator deviates by 2.4 μm (± 2.4 μm), this represents a 0.1% deviation in frequency. Using eq. (5.15) and setting $\Delta = 0.1\%$ and $E = 2.4$ μm, the minimum gap d_1 should be 600 μm. It should be noted that a larger gap could be implemented to increase robustness but at the cost of both size and a degradation in Q-factor.

5.2.3 Resonator Design

In order to design the resonator, both the resonator and its couplings need to be considered. The resonator volume limits the maximum couplings and the minimum length of the transmission line above the resonator. The resonator design parameters include the outer radius b, post radius a, inner radius c, cavity height h, post gap d_1, wall-gap d_2, and membrane thickness d_3. While the coupling parameters are wholly based on the selected topology.

For this paper, the coupling specifications of [35] may be reused. The condition required to achieve the all-pass response is given by [35]

$$k_2 = \frac{\pm k_1}{2\sin\theta_T}. \tag{5.16}$$

Table 5.3.
Available substrates and calculated values for a and c

thickness (mm)	a (mm)	c (mm)
5.08	8.1	5.86
6.35	6.7	7.42
6.985	6.1	7.92
7.62	5.5	8.35

The resonator couplings k_1, k_2, and θ_T are 0.2, 0.13, and 45 degree, respectively, which satisfies the above conditions and achieves a 3-dB bandwidth of 6%. The 3-dB bandwidth can be approximated as $\sqrt{2}k_1^2$.

The wall-gap d_2 should be as small as possible based on Fig. 5.2 to maintain a high Q-factor. In reality, the wall-gap is limited by the assembly. Thus, d_2 is 0.2 mm. The membrane should be thin for compactness, as well as not too thin for robustness. Therefore, d_3 is 0.5 mm. For this topology, the outer radius of the cavity is limited by the length of the transmission line. Here, the outer radius, b is 10 mm. Now C_3 can be calculated. Inserting d_2, d_3, and b into eq. (5.12), C_3 is 1.73 pF. For design convenience, C_1 is designed to be the same as C_2. From eq. (5.3) and eq. (5.11), c is approximately equal to $\sqrt{a^2 + b^2}$. Inserting the eq. (5.1) for L_0, eq. (5.2) for C_0, and eq. (5.3) for C_1 into eq. (5.13), and setting the resonant frequency f to 1.5 GHz, a and h can be calculated. Several available Rogers TMM 3 substrates are listed and their corresponding a and c are calculated in Tab. 5.3. For the 5.08-mm substrate, c is smaller than a, therefore it is not a working design. All the rest listed in the table are valid designs. For compactness, the 6.35-mm substrate is selected. Therefore, a is 6.7 mm. The dimensions and RF properties of the resonator are summarized as design IV in Tab. 5.4. Four other resonators with different post gap ranges and same frequency tuning range (1.5 to 2 GHz) are simulated and included for comparison.

Table 5.4.
Dimensions and RF properties of the Cavity Resonators

Design	I	II	III	IV	V
gap (μm)	22-50	95-200	220-560	0.6k-2.6k	1k-6k
Rout (mm)	7	8	9	10	12
Rin (mm)	4	5	6	6.7	9
height (mm)	1.91	5.08	6.35	6.35	7.62
vol. (mm^3)	294	1021	1616	1995	3447
Q-factor	453-531	601-667	476-648	457-605	314-561
Freq. error (2μm) (%)	1.6-2.0	0.15-0.75	0.1-0.36	0.02-0.1	0.01-0.05
Freq. error (10μm) (%)	8.5-9	1.3-4.4	0.37-1.6	0.05-0.5	0.004-0.2
Max. Power (W)	42	145	450	700	1700

Only resonator IV and V satisfy the frequency variation tolerance, and resonator IV has a higher Q-factor and smaller volume than resonator V. The table and the results validate the design and the procedure.

5.2.4   Filter Design and Implementation

The quasi-absorptive bandstop-to-all-pass filter with 1.5 to 2 GHz tuning range from reference [35] is redesigned based on the resonator designed in the previous section. The exploded view of the filter model in HFSS is presented in Fig. 5.10,

which has three laminated layers with PCB substrates: the transmission-line layer, the cavity layer, and the side-wall layer. The transmission-line layer has a 50 Ω source-to-load microstrip line which is designed on a 0.508-mm thick Rogers TMM 3 substrate ($\varepsilon_r = 3.27$, $\tan(\delta) = 0.002$). The cavity layer has two cavity resonators which are designed on a 6.35-mm thick Rogers TMM 3 substrate.
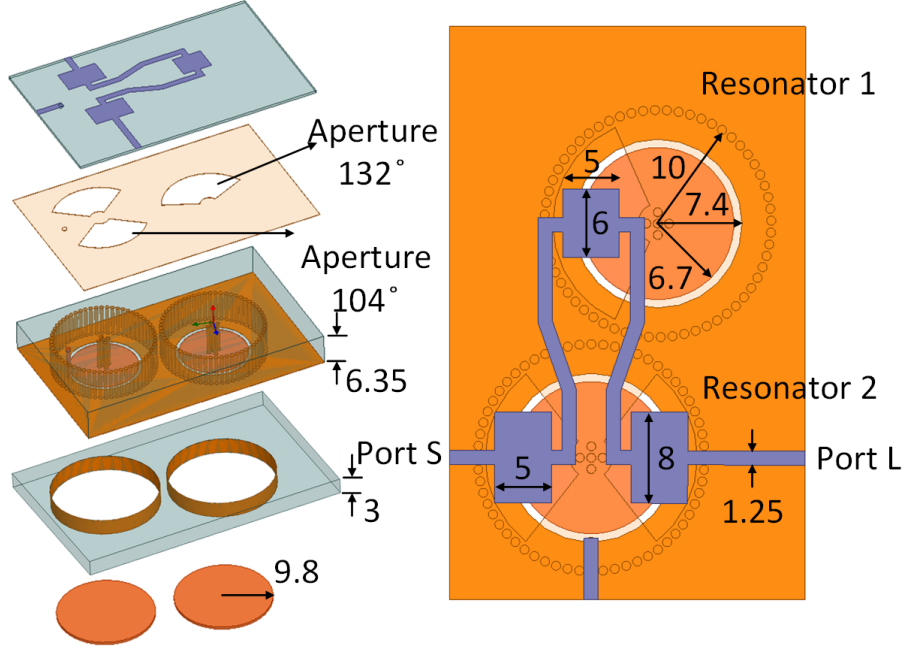
Fig. 5.10. HFSS simulation model and dimensions (in millimeters) of the proposed evanescent-mode cavity filter.

The coupling of the resonators is controlled by the angles of the aperture slots at the ground plane between the microstrip lines and the cavities. The angles are selected to be 132° for resonator 1 and 104° for resonator 2. The resulting k_1 is 0.2 and k_2 is 0.13, which satisfy the required condition to achieve both the all-pass and the bandstop states [35]. In order to compensate for the series inductance introduced by the coupling slots, capacitive pads are added in the design [34]. The side-wall layer consists of a 3-mm thick Rogers TMM 3 substrate with two electroplated holes over which the membranes sit. The filter is simulated in HFSS with a deviation in the post gap to validate the robustness. If the filter performance does not satisfy the

criteria, the minimum resonator gap should be increased, and the resonator should be redesigned accordingly. The design iterations should be repeated until the deviated filter performance meet the design criteria.

The filter is assembled without using superglue and epoxies which have a thermal expansion higher than 1 μm per degree Celsius. Instead, gold-plated screws and solder are used for bonding as shown in Fig. 5.11. The packaging box is made of aluminum, and the M3-Ls are screwed on it. The filter is one part of the system, and therefore other parts are shown in the housing unit such as a power sensing board.
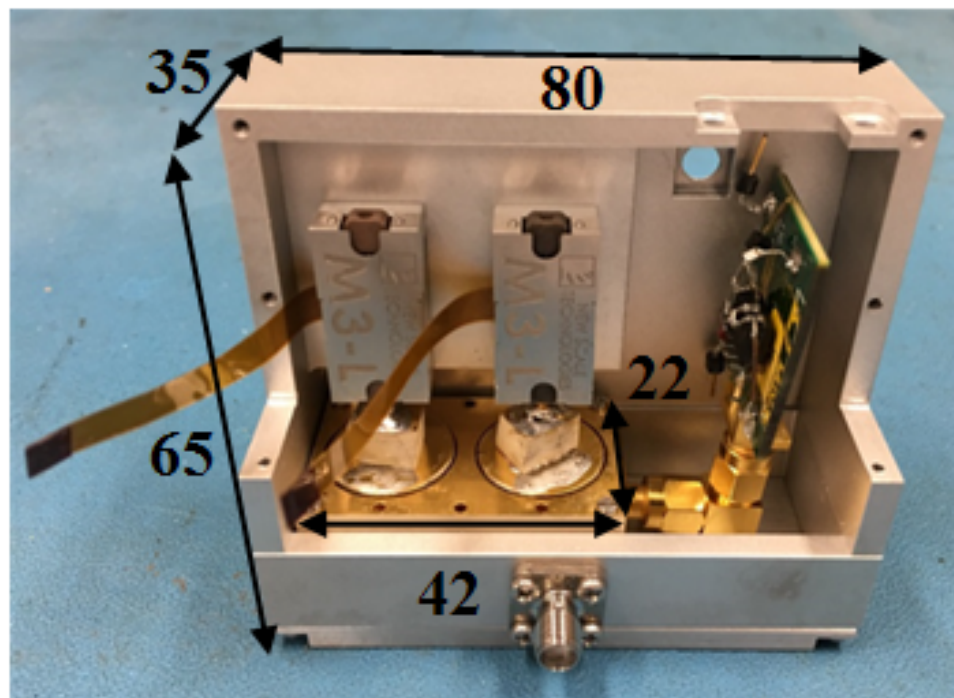
Fig. 5.11. Filter prototype with full metallic packaging. All dimensions are in millimeter.

5.3   Filter Measurement Results

The absorptive bandstop-to-all-pass filter is measured for its response and for robustness, which includes long-term stability and repeatability, RF power handling, vibration, and temperature sensitivity measurements. These measurements validate
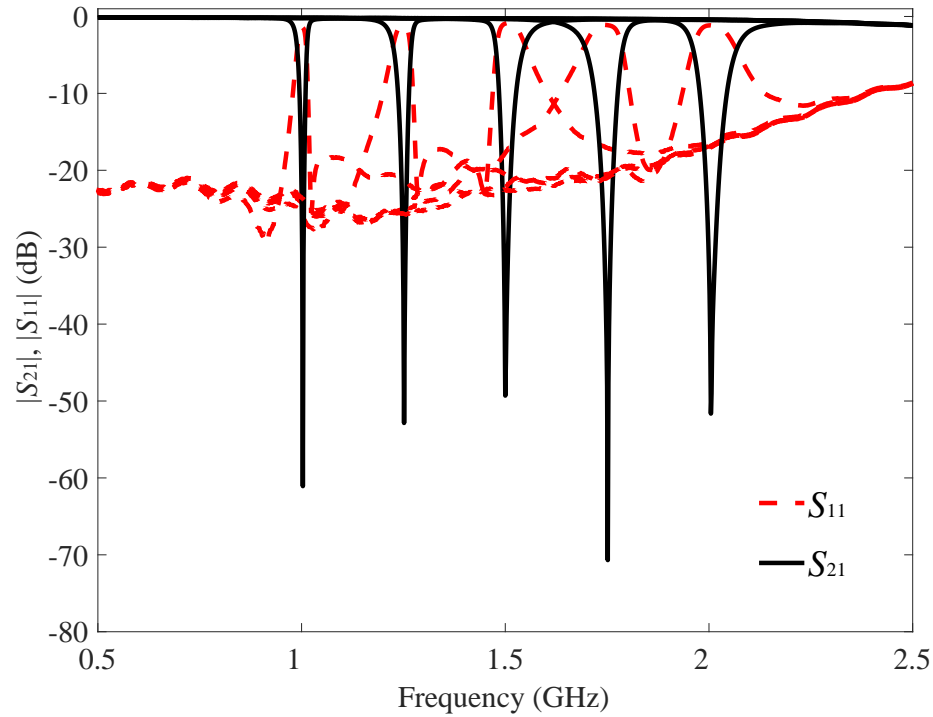
Fig. 5.12. Measured frequency response of the filter in the bandstop state. The filter presents a measured notch of 45 to 55 dB in its 1-2 GHz tuning range. 3-dB bandwidth is increases from 5.3% at 1.5 GHz to 6.2% at 2 GHz.

the robustness of the filter and investigate its potential in a variety of applications. This section presents the measurement setups and discusses the results in detail.

5.3.1 Bandstop-to-All-Pass Response

The bandstop and all-pass responses are measured with the Agilent N5230C network analyzer. The bandstop measurement results from 1 to 2 GHz are shown in Fig. 5.12. The notch filter can achieve a notch of 45 to 55 dB across its entire tuning range. The measured 3-dB bandwidth is 5.3% at 1.5 GHz and increases monotonically to 6.2% at 2 GHz. The measured 10-dB bandwidth is 2.7% at 1.5 GHz and increases to 3.0% at 2 GHz. The all-pass measurement results are shown in Fig. 5.13. The measured out-of-band insertion loss is less than 0.8 dB. The in-band insertion loss is

decreasing from 2.2 dB at 1.5 GHz to 2 dB at 2 GHz, but this loss can be mitigated by shifting the notch out of band thus giving 0.8 dB of insertion loss. Note that the filter is measured with two SMA connectors with the associated connector-to-microstrip transitions. Based on the all-pass insertion loss, the Q-factor is extracted to be 320 at 1.5 GHz and 250 at 2 GHz.
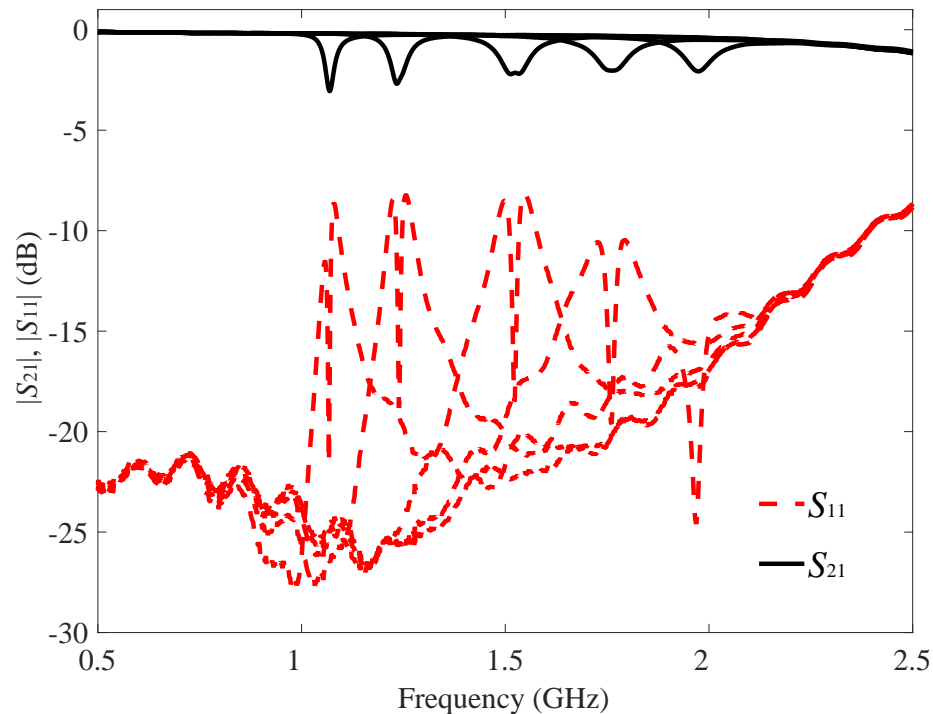
Fig. 5.13. Measured frequency response of the filter in all-pass mode. The in-band insertion loss is 2.9 dB at 1 GHz, 2.2 dB at 1.5 GHz, and 2 dB at 2 GHz.

5.3.2 Long-term Stability

In this measurement, the filter is tuned to a certain frequency, and the isolation level at that frequency is recorded every 10 minutes for 5 days. The long-term stability is measured at 1.5, 1.75, and 2 GHz. The results, as plotted in Fig. 5.14, suggest that the attenuation level slightly varies with time, but the filter maintains a more than 45-
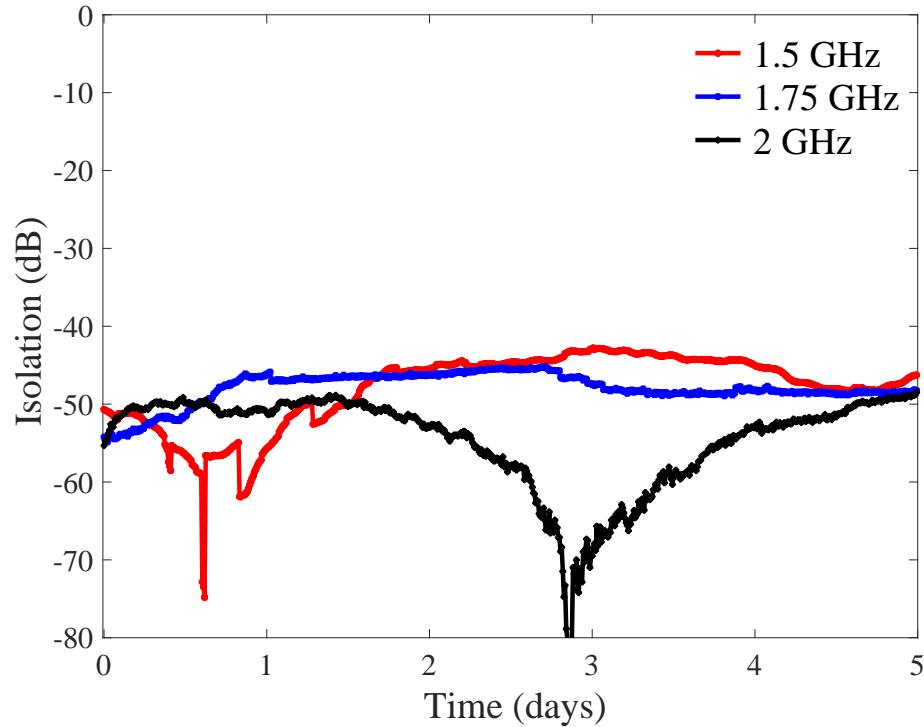
Fig. 5.14. Measurements of the long-term test. The fabricated filter's notch is recorded at 1.5, 1.75, and 2 GHz for 5 days.

dB notch for the first 24 hours, and a 40-dB notch throughout the whole measurement period. The test was stopped at the end of the 5th day with no observed failures. It should be noted that theoretically, infinite isolation occurs when the two resonators are at exactly the right frequencies. This is seen with the 2-GHz curve at the close of day three.

5.3.3   Repeatability

The repeatability is characterized as another aspect of robustness. The notch filter is controlled to switch between a certain frequency and its "home" state for 2000 iterations. The "home" state is when the post gap is at its maximum, which is 6 mm due to the M3-L limitations. The time interval between each move is 10 seconds, and the isolation at the desired frequency is recorded 6 seconds after each hit. The

filter is tested at 1.5, 1.75, and 2 GHz, and the results are plotted as a histogram in Fig. 5.15. The calculated expectation values are -45.2, -47.56, and -51.08 dB, and the standard deviations are 4.58, 2.50, and 1.31 dB for 1.5, 1.75, and 2 GHz, respectively. The absolute worst isolation occurs at 1.5 GHz and is around 35 dB.
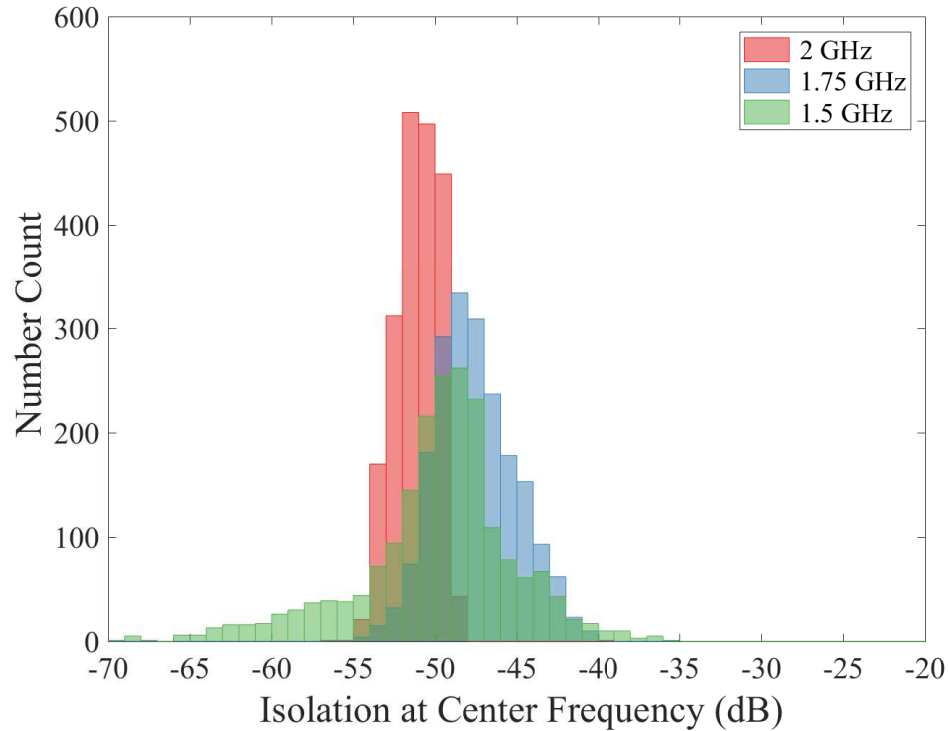
Fig. 5.15. Measurements of repeatability test of 2000 hits at 1.5, 1.75, and 2 GHz. Measurements are plotted as a histogram. The calculated mean is -45.2, -47.56, and -51.08 dB with a standard deviation of 4.58, 2.50 and 1.31 dB for 1.5, 1.75, and 2 GHz, respectively.

5.3.4 Vibration and Temperature Sensitivity

The filter is tested for vibration and temperature sensitivity which characterizes the performance for most real-world applications. It should be stated that these tests capture the effects of the filter's performance which include the whole system, specifically the actuator circuit.
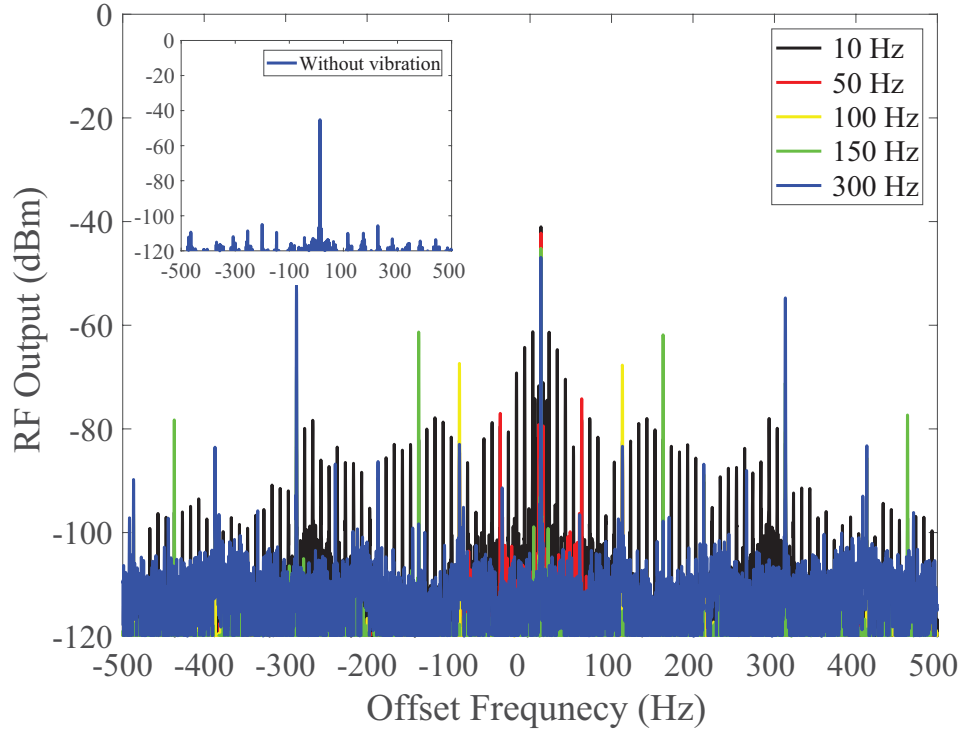
Fig. 5.16. Spectrum of the RF output from the filter under 10-, 50-, 150-, and 300-Hz vibration at 1 g. The input is a 0-dBm single-frequency signal at 1.75 GHz. The filter is able to maintain a 40-dB isolation level while the harmonics are lower than −50 dBm.

In the vibration test, the filter is mounted on a shaker where an ADXL335 accelerometer is used to characterize the acceleration [115]. The filter has been tested under 10-, 50-, 150-, and 300-Hz vibration at 1 g and the responses are plotted in Fig. 5.16. The filter is excited with a single-frequency tone of 1.75 GHz with 0 dBm input. Without the vibration, the wide-band response contains no harmonics greater than −100 dBm. The effect of these vibrations is generated harmonics offset by the same delta frequency as the vibration source since the membrane and thus post gap capacitance are being modulated. Nonetheless, this does not affect the filter's performance at the notch frequency as it is able to maintain a 40-dB isolation level. There are, however, harmonics slightly lower than −50 dB offset by the vibration frequency. The worst of which occurs at a vibration frequency of 300 Hz as this is close to the
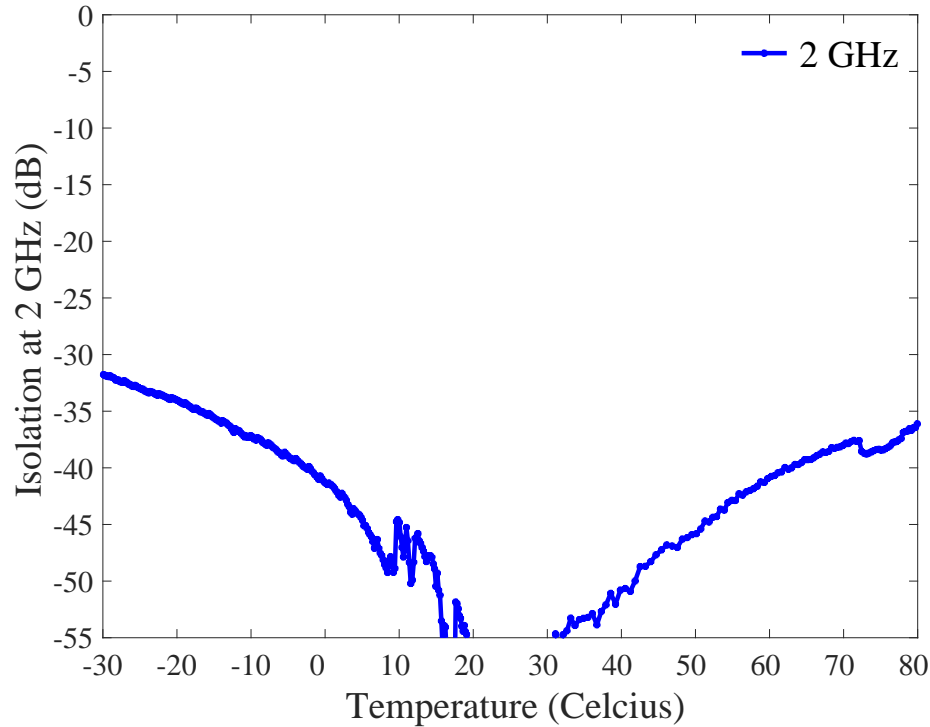
Fig. 5.17. Measurement of notch depth at 2 GHz with temperature a sweep from −30 to 80 degrees Celsius. The filter is able to maintain a more than 30-dB notch.

mechanical SRF of the M3-L actuator. It should be mentioned that the applied frequency's motion is parallel to the normal of the membrane, representing a worst-case scenario.

For the temperature test, an environmental chamber is swept from −30 to 80 degrees Celsius while the filter's 2 GHz response is recorded. The filter's isolation is plotted in Fig. 5.17. For the whole temperature range, the filter shows a controlled response and is able to maintain a more than 30-dB notch. It is worth mentioning here the cause in the degradation in performance at the extreme temperature ends. The primary cause of this performance change is due to the actuator and its construction. For instance, the plastic pin of the M3-L actuator has a thermal coefficient of 0.5 μm per degree Celsius which causes it to expand at high temperatures and compress at low temperatures causing a deviation in the membrane displacement. A first-

order approximation can be made from section II where the error in the post gaps is discussed. Similar effects can be explained when other implementations are used by looking at the thermal expansion.

5.3.5 RF Power handling

For the high-power measurement, an Agilent N5230C network analyzer is used to provide the filter a 1.75 GHz excitation that is amplified to 10, 50, 75, and 100 W with an AMP2070A power amplifier. Accounting for the insertion loss from the connecting cables, a 0.36 dB loss is seen meaning the maximum tested power is about 92 W. The output from the filter is attenuated by the same gain as the amplifier. The transmission coefficient for the frequency response is shown in Fig. 5.18. As the reflection coefficient is not merely from the filter but rather from the power amplifier, it is not shown. The filter is able to maintain a 90-W high power test without failure, showing great potential in high-power applications.

5.4 Conclusion

For the first time, a design procedure to optimize for robustness of evanescent-mode substrate-integrated cavity resonators and filters is presented and demonstrated with one of the most sensitive filter topologies. The contact-less design with extended side-wall (ESW) has been proved to be the most robust implementation. The demonstrated filter is designed and optimized following the proposed procedure using this resonator design. The fabricated filter meets all the design criteria and is robust. It has demonstrated a 40-dB bandstop notch throughout the 5-day measurement and does not drift at the end. The repeatability is verified with expectations more than -45 dB and the absolute minimum data point is more than -35 dB. The filter has also been tested for RF power handling, vibration, and temperature sensitivity. The results suggest that careful design can significantly improve the robustness of the cavity filters.
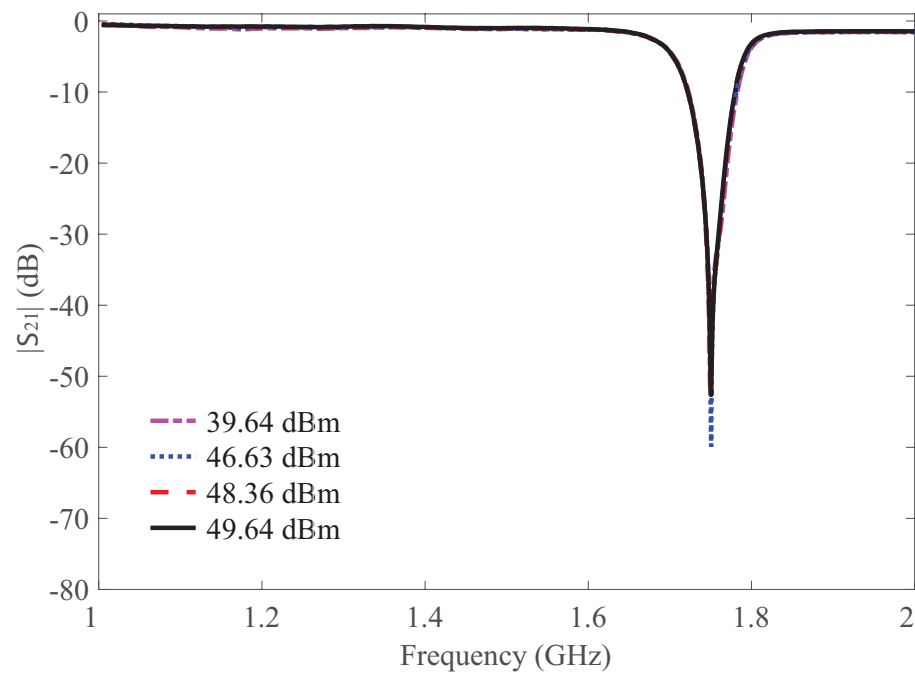
Fig. 5.18. Frequency response of the filter with 10-, 50-, 75- and 90-W RF input power. A more than 50-dB notch is maintained under all input powers.

6. FREQUENCY-SELECTIVE LIMITERS WITH OPTIMIZED STRUCTURES AND FORM FACTOR

This chapter presents an FSL that is implemented with the filter demonstrated in the previous chapter. This FSL is implemented with a commercial actuator, M3-L, which has built-in control loop [116]. As a result, the size of the proposed FSL is as small as 7% of the FSL in Chapter 4. The FSL demonstrates the same state-of-the-art RF performance. Also, as the filter is optimized for robustness, the FSL is reliable.

6.1 System Architecture

The overall system diagrams for the proposed FSL and the FSL in Chapter 4 are shown in Fig. 6.1. The FSL in Chapter 4 includes 1) a triplet absorptive bandstop-to-all-pass filter (black font), 2) a power detector and comparator (green font) that are coupled to one of the resonators, and 3) a feedback control loop scheme (blue font) that controls both resonators. The proposed FSL employs M3-L actuators, which has built-in control loops. The M3-L can be directly controlled from Matlab, and therefore the FPGA is not necessary anymore. Instead, a NI DAQ is used to acquire the power level information from the comparator. The simplified system diagram of the proposed FSL is shown in Fig. 6.1(b).
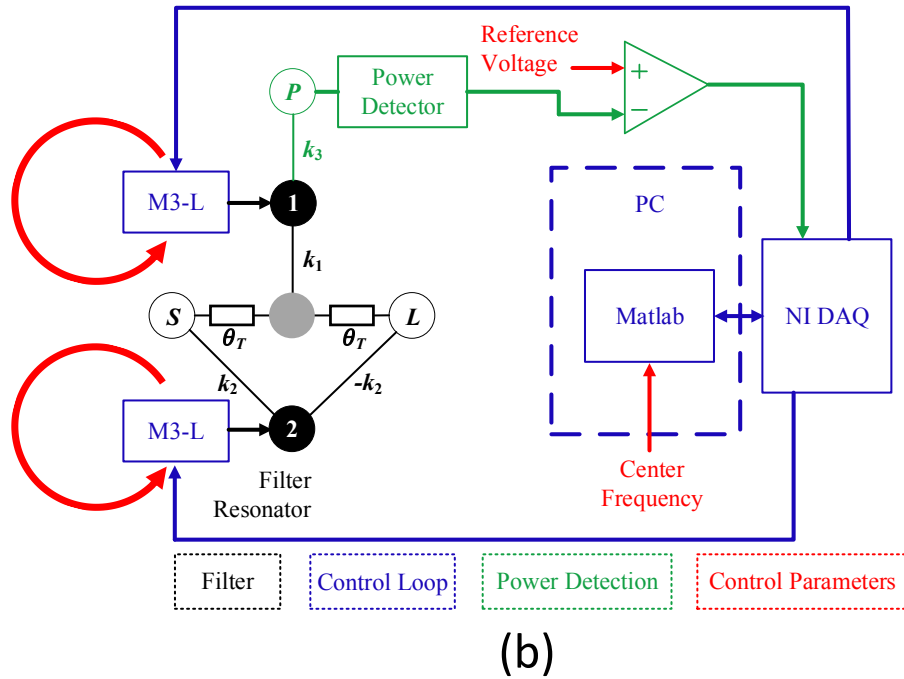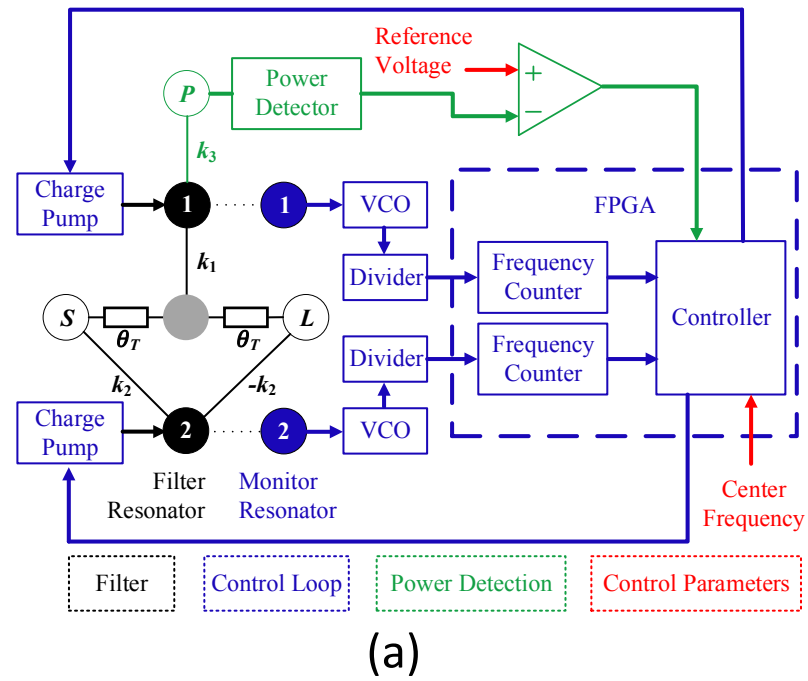
Fig. 6.1. Overall system diagram for FSLs in (a) Chapter 4, and (b) this chapter. The filter is in black, feedback control loops are in blue, and power detection is in green. Tunable/input parameters are in red color.
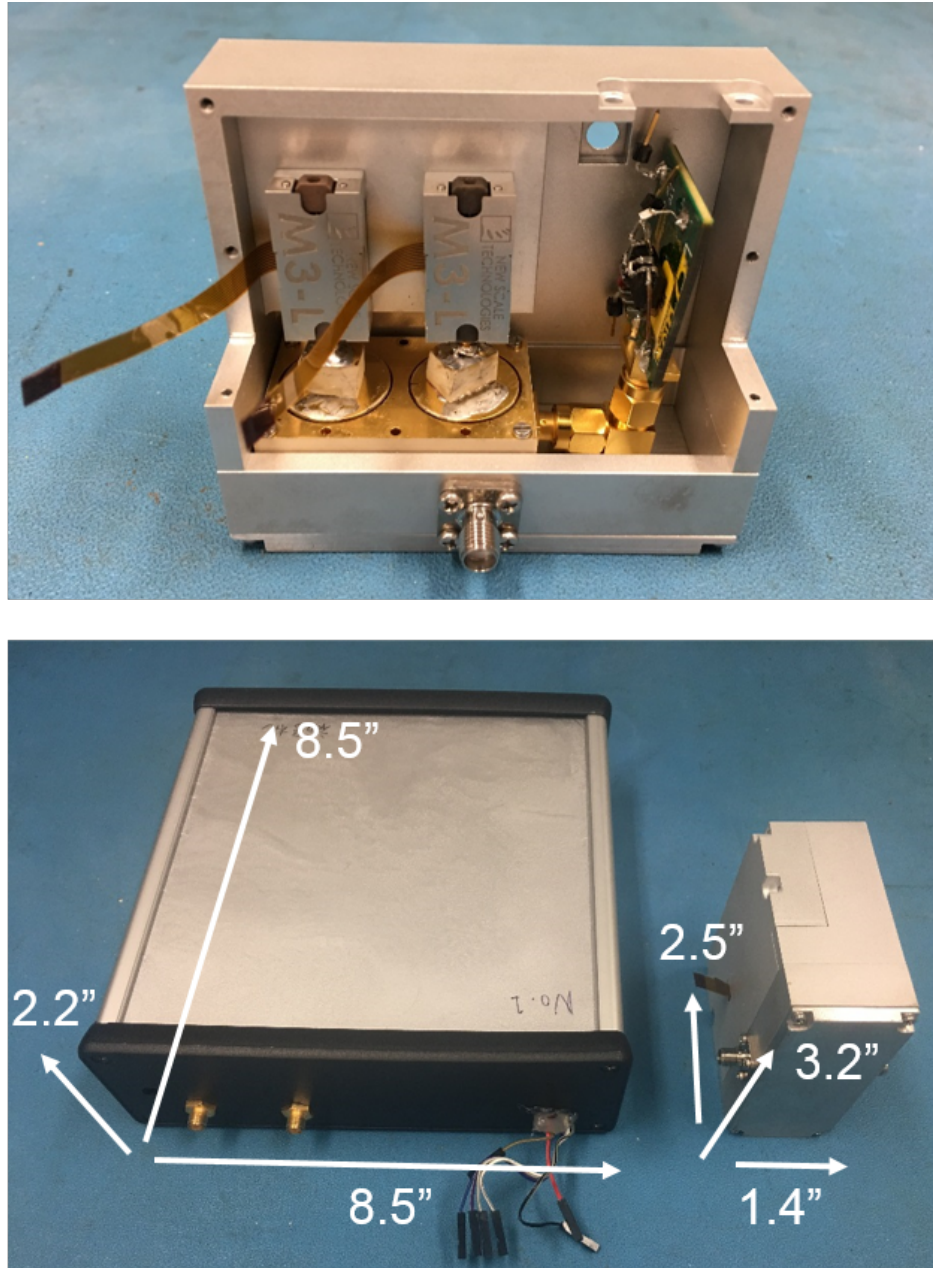
Fig. 6.2. Filter prototype with full metallic packaging (top) and comparison of dimensions of the filter from Chapter 4 (bottom).

6.2   FSL Implementation

The filter from the previous chapter is used to implement the FSL. The power detection scheme is installed on resonator 2. A via coupling, which results in -20-dB coupling, is implemented in the cavity. The output is connected to the input of the power detector (LT5538). A LED indicator is made for the visualization purpose. The FSL is assembled without using superglue and epoxies. Instead, gold-plated screws and solder are used for bonding. The packaging box is made of aluminum, and the M3-Ls are screwed on it.

6.3   Measurement Results

The fabricated FSL is measured for its three modes. The measurement setup is the same as the setup used to measure the FSL in Chapter 4. Frequency measurements use the Agilent N5230C network analyzer, and power measurements use a single tone generator (Agilent E4433B) and a spectrum analyzer (Tektronix RSA3408A). The FSL is controlled by a computer, and there is no external bias needed. The following subsections discuss the measurement results separately.

6.3.1   User-Defined Bandstop Mode

The FSL in user-defined bandstop mode is measured with the Agilent N5230C network analyzer. In this measurement, the FSL is tuned to selected frequencies using a Matlab program with the calibration table. The bandstop measurement results from 1 to 2 GHz are shown in Fig. 6.3. The notch filter can achieve a notch of 45 to 55 dB across its entire tuning range. The measured 3-dB bandwidth is 5.3% at 1.5 GHz and increases monotonically to 6.2% at 2 GHz. The measured 10-dB bandwidth is 2.7% at 1.5 GHz and increases to 3.0% at 2 GHz.
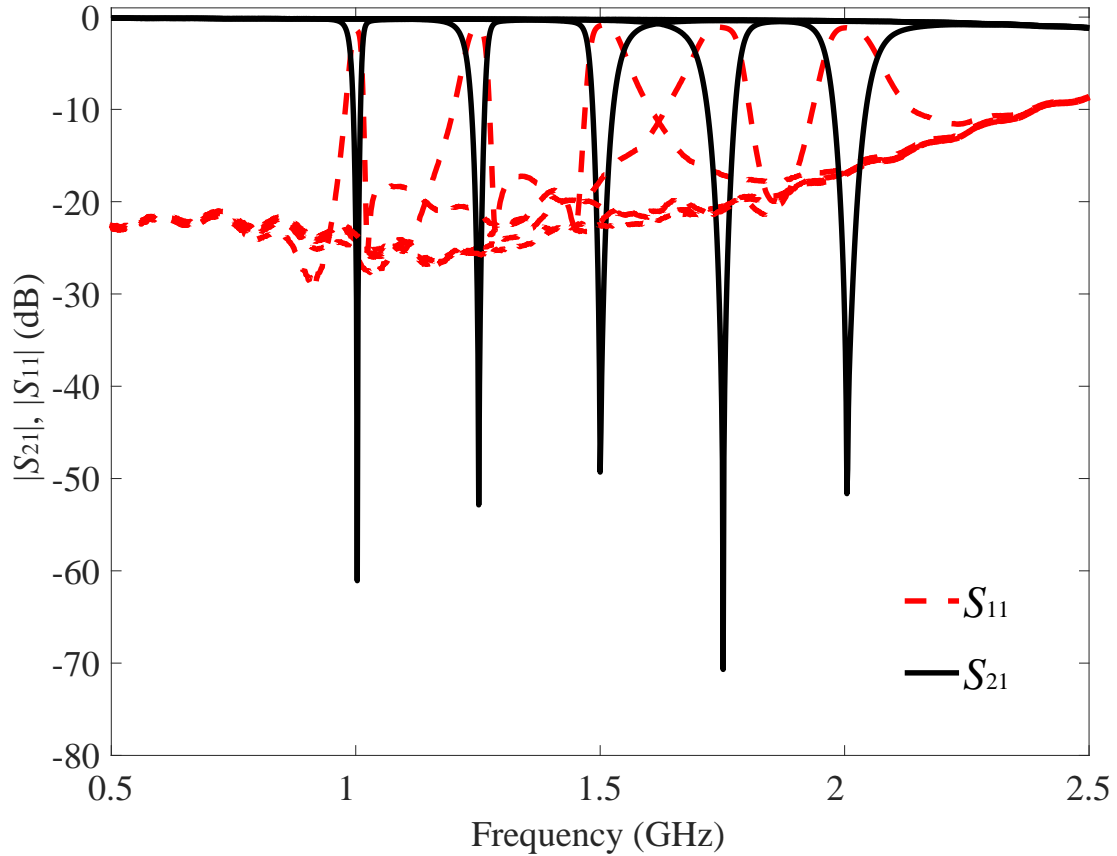
Fig. 6.3. Measured frequency response of the filter in bandstop state. The filter presents a measured notch of $45-55$ dB in its $1-2$ GHz tuning range. 3-dB bandwidth is from 5.3% at 1.5 GHz to 6.2% at 2 GHz. This figure is the same as Fig. **??** and is repeated here for convenience.

6.3.2 All-Pass Mode

The all-pass measurement results are shown in Fig. 6.4. The measured out-of-band insertion loss is less than 0.8 dB. The in-band insertion loss is decreasing from 2.9 dB at 1 GHz, to 2.2 dB at 1.5 GHz, and 2 dB at 2 GHz. Note, the filter is measured with two SMA connectors and the associated connector-to-microstrip transitions.
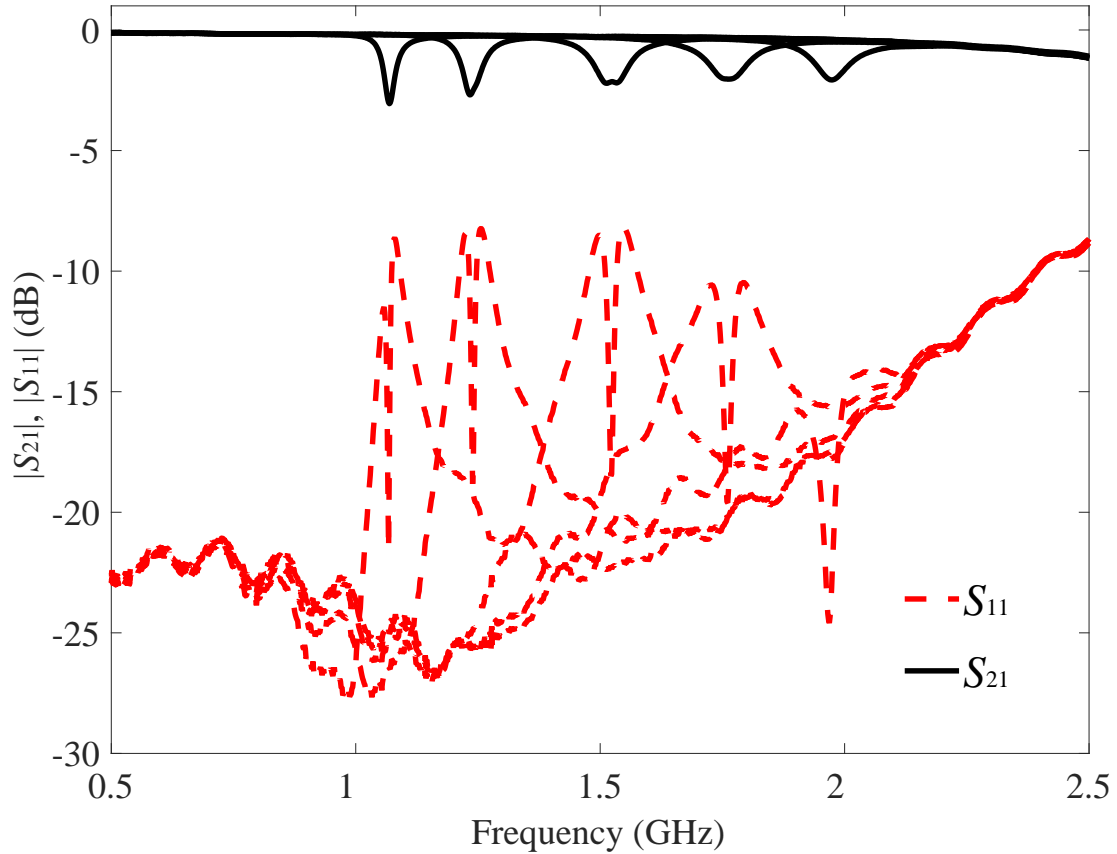
Fig. 6.4. Measured frequency response of the filter in all-pass mode. The in-band insertion loss is 2.9 dB at 1 GHz, 2.2 dB at 1.5 GHz, and 2 dB at 2 GHz. This figure is the same as Fig. **??** and is repeated here for convenience.

6.3.3   Power-Activated Mode

The filter in power-activated mode is measured at 1, 1.25, 1.5, 1.75, and 2 GHz, respectively. In this test, the power threshold level is set to -45 dBm. The incident power at the selected frequency is swept from -50 to -35 dBm, and the output power level at that frequency is recorded from the spectrum analyzer with 1 dBm increments. The measurement results are plotted in Fig. 6.5. The power thresholds are measured -47.35, -44.85, -43.05, -43.95, and -44.65 dBm. The power threshold has 2 dBm

variation, and this is due to the variance of the external coupling and gain of the LNA.
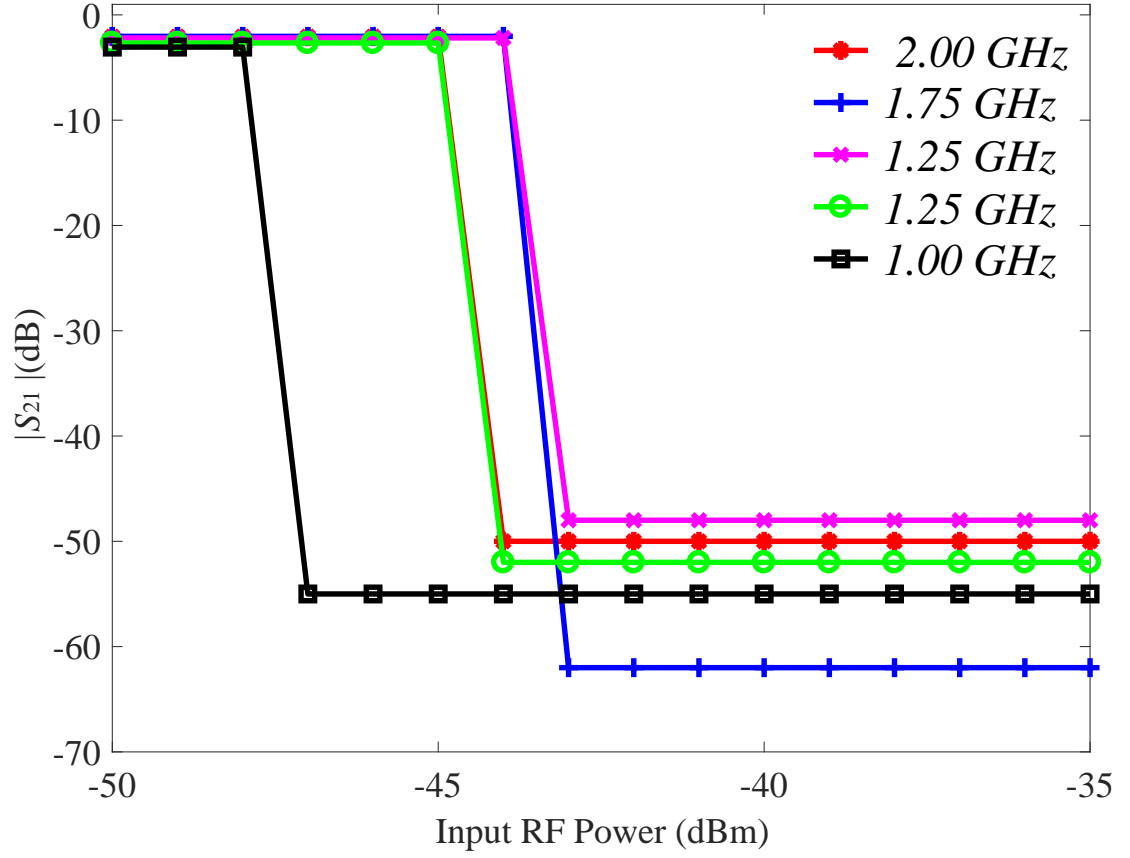
Fig. 6.5. Measured RF input power vs. isolation level at 1, 1.25, 1.5, 1.75, and 2 GHz respectively with 1 dBm step size from -50 to -35 dBm. The power threshold is -47.35, -44.85, -43.05, -43.95, and -44.65 dBm.

7. SUMMARY AND FUTURE WORK

7.1 Dissertation Summary

This dissertation has presented the coupling matrix synthesis of the triplet absorptive bandstop-to-all-pass filter topology. The demonstration is implemented with substrate-integrated evanescent-mode cavity technology with a tuning range from 1 to 2 GHz. This filter topology has unique property that in both modes one resonator is always located at the center frequency. This enables real-time power monitoring at the center frequency. The filter is used to implement the frequency-selective limiters (FSLs). There are three components in this system: filter, feedback control loops, and power detector scheme. The system is demonstrated with the same technology and a long-term measurement up to 9 hour is reported. To further optimize the robustness of the system, several designs of cavity resonator are comparatively studied. With a large gap range (200 - 2000 μm) and a contact-less design with extended side-wall design, the variation of resonate center frequency due to gap error is minimal and the unloaded Q-factor is minimally affected. A commercial M3-L actuator is used which has integrated control loop. The filter is redesigned based on a novel design procedure. A long-term measurement up to 5 days is reported for the demonstrated filter.

7.2 Contributions

The specific contributions of this dissertation are as follows.

Chapter 2: For the first time, the coupling matrix synthesis of the triplet absorptive filter topology is presented. An advanced coupling matrix technique is developed to represent transmission lines with arbitrary degrees. The coupling matrices that

yield quasi-absorptive bandstop response, fully-absorptive bandstop response, and all-pass response are derived. The coupling matrices are modified to include the resonator Q-factors. Coupling coefficients are revised to maintain absorptive response.

Chapter 3: For the first time, the triplet absorptive filter topology is implemented with high-Q substrate-integrated evanescent-mode cavity technology. The filter demonstrates both quasi-absorptive response with high isolation (70-dB) and all-pass response with minimum insertion loss of 2.27 dB and maximum insertion loss of 3.14 dB. These two responses are demonstrated in 1.1 GHZ to 2 GHz frequency range. The filter can also be tuned between these two states to achieve variable attenuation. The extracted unloaded resonator Q-factor is 400. This is the first time to demonstrate this topology with an octave tuning range. The all-pass insertion loss is also state-of-the-art.

Chapter 4: A FSL system that is superior in terms of RF and limiting performance than the existing ones is demonstrated. This system employed the triplet absorptive filter topology, is implemented with high-Q substrate-integrated evanescent-mode cavity technology, integrated with feedback control loops, and has a reconfigurable power limit level. While the mostly used FSLs that are implemented either with ferrite material or Shotkey diodes provide around 40-dB isolation, this proposed FSL can provide 70-dB isolation. While the mostly used FSLs have pass insertion loss of more than 5 dB, this FSL has pass insertion loss of less than 3.1 dB. While the mostly used FSLs cannot easily change the limit power, this FSL can be reconfigured in the -45 to $+8$ dBm range, which covers most of the wireless applications. The FSL is demonstrated in $1.5-2$ GHz tuning range. The extracted resonator Q-factor is around 300.

Chapter 5: For the first time, the robustness for the substrate-integrated evanescent-mode cavity applications is studied. All of the existing resonators designs are comparatively studied, and the trade-offs are discussed. The optimal resonator design for robustness is presented. A filter-level design and optimization procedure is proposed. To the knowledge of the author, this is the first time for such a design procedure. This produced is generic and can be applied with any actuators and filter typologies. As an

example, a bandstop filter with the triplet absorptive filter is demonstrated. The filter demonstrates its robustness in terms of long-term stability, repeatability and temperature sensitivity. The filter is also tested in high-power and vibration environments to show the potential. The measurement results suggest that a careful design can significantly improve the robustness of the filters using the evanescent-mode cavity technology.

Chapter 6: A FSL with the same features as the FSL demonstrated in Chapter 4 but only 7% volume is demonstrated. The FSL employs the optimized filter design and implementation from Chapter 5. The actuator is implemented with commercial M3-L actuators. The controlled maximum attenuation is more than 45 dB and the minimum attenuation is less than 2.9 dB. The FSL has a octave tuning range from 1 to 2 GHz.

7.3 Future Work

This dissertation provides the coupling matrix synthesis of the triplet absorptive topology. A transmission line with arbitrary degrees is represented in the coupling matrix. This opens a huge area: coupling matrix synthesis of filter topologies with non-90-degree inverters. One of the examples is to reinvestigate the quarter wavelength bandstop topologies. With resonator detunings, it is possible that the topology does not require 90 degree phase shift. Another example is the absorptive filter design I. It is shown that the absorptive response is decreases when the phase shift is not 90 degree. With the help of this technique, the filter behavior with non-90-degree transmission line can be analyzed, and thus, tuning range. In [19], an absorptive topology with two sections of 120 degree transmission lines is demonstrated with fully-absorptive response. However, the topology is not studied. These are just a few examples to illustrate the impact of this technique, and the world where it applies.

The optimized FSL in this dissertation is based on a large-gap cavity resonator. The large-gap cavity resonator is not well-studied. For example, all the previous

works suggest that with a larger post-gap, the unloaded Q-factor increases. This is true when the post-gap is very small. As the post-gap increases, there is a point where the unloaded Q-factor actually starts to decrease. The study of Q-factor and gap can significantly improve RF property of the cavity resonator. It is also not clear if this optimal gap is frequency-dependent (resonant wavelength) or volume-dependent (outer radius, height, inner radius, etc). As PCB technology is pushed to K/Ka band or even W band, the resonator Q-factor becomes an issue [117]. How to optimize the filter for Q-factor should be studied carefully.

An ideal FSL has an attenuation range from 0 dB for all-pass and infinity for isolation. Unlike the absorptive response, the all-pass insertion loss is limited by the resonator Q-factor. It is possible to improve the insertion loss by increasing the design bandwidth, but it is not very useful. One of the approach is to implement a negative resistance in parallel with the "inductance" of the cavity. This can be achieved by a bipolar transistor whose emitter is grounded by a section of transmission line. The concept has been demonstrated in [118]. This can yield zero insertion loss in the all-pass response.

If the resistance of the transistor can be manipulated, the FSL will not only be able to attenuate or pass, but also be able to amplifier the signal. This is particularly helpful in a wide-band receiver system where all the signals are desired. In this case, an ideal FSL is channelized. Each channel is able to attenuate, pass, or amplify with no distortions. All the channels are connected in series to cover the full band. The concept is illustrated in Fig. 7.1. Each filter parks at a fixed channel and one tuning elements is required to switch the filter to form attenuation, pass, or amplification.

The Buttrworth bandstop response has relatively poor selectivity compared to the Chebyshev response. Unfortunately, the absorptive response results in Butterworth response. In other words, the condition to achieve absorptive response is the Butterworth condition. If the negative resistance concept is successfully implemented, the absorptive response is not necessary. The triplet filter can be designed to yield Chebyshev response. To further improve the selectivity, higher-order Chebyshev fil-
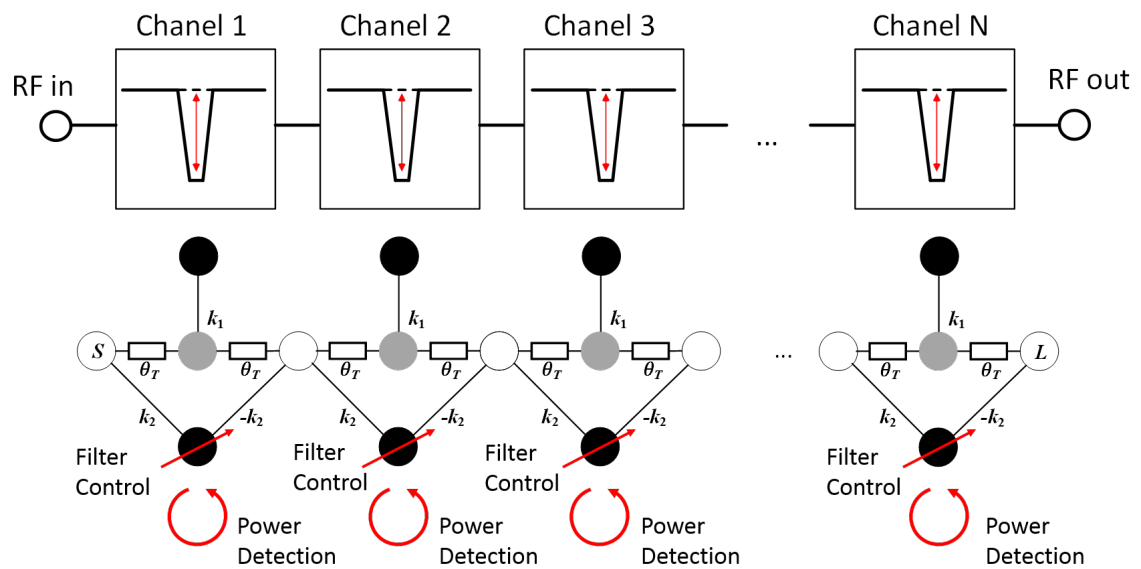
Fig. 7.1. Circuit diagram of a channelized FSL. Each filter parks at a channel and one tuning elements is required to switch the filter response among bandstop, all-pass, and amplification.

ters can be implemented. An example to derive the coupling matrix for a fourth-order triplet filter topology is shown in Appendix C. Higher-order syntheses of the triplet filter topology for Chebyshev response can be found in [119].

The channelized FSLs will be useful in the radar warning receivers, one of the electronic warefare (EW) technologies that will quickly detect, locate, and identify emitters of RF signals. In such a system, every signal in the spectrum is of interest, and making every signal equal power is important to increase the sensitivity and dynamic range of the receiver systems.

REFERENCES

REFERENCES

[1] R. Cameron and C. Kudsia, *Microwave Filter for Communication Systems: Fundamentals, Design and Applications*. Wiley, 2007.

[2] I. Hunter, R. Ranson, A. Guyette, and A. Abunjaileh, "Microwave filter design from a systems perspective," *IEEE Microw. Mag.*, vol. 8, no. 5, pp. 7177, Oct. 2007.

[3] L. Young, G. L. Matthaei and E. M. T. Jones, "Microwave Bandstop Filters with Narrow Stop Bands," *PGMTT National Symposium Digest*, Washington, DC, USA, 1962, pp. 46-51.

[4] B. Perlman, J. Laskar and K. Lim, "Fine-tuning commercial and military radio design," in *IEEE Microwave Magazine*, vol. 9, no. 4, pp. 95-106, Aug. 2008.

[5] K. L. Kotzebue, "Frequency-Selective Limiting," in *IRE Transactions on Microwave Theory and Techniques*, vol. 10, no. 6, pp. 516-520, November 1962.

[6] H. Suhl, "The Nonlinear Behavior of Ferrites at High Microwave Signal Levels," in *Proceedings of the IRE*, vol. 44, no. 10, pp. 1270-1284, Oct. 1956.

[7] N. J. Brown, "Design concepts for high-power PIN diode limiting," *IEEE Trans. Microw. Theory Techn.*, vol. MTT-15, no. 12, pp. 732742, Dec. 1967.

[8] A. L. Ward, R. J. Tan, and R. Kaul, "Spike leakage of thin Si PIN limiters," *IEEE Trans. Microw. Theory Techn.*, vol. 42, no. 10, pp. 18791885, Oct. 1994.

[9] M. van Wanum and F. E. van Vliet, "A 58-dBm S-band limiter in standard 0.25-m BiCMOS technology," *IEEE Trans. Microw. Theory Techn.*, vol. 61, no. 8, pp. 30343042, Aug. 2013.

[10] S. Hori, M. Kuroda, K. Kanema, and S. Okano, "High-power MIC diode limiters for S- and X-band RADARs," in *IEEE MTT-S Int. Microw. Symp. Dig.*, Apr./May 1979, pp. 329331.

[11] D. J. Seymour, D. D. Heston, R. E. Lehmann, and D. Zych, "X-band monolithic GaAs PIN diode variable attenuation limiter," in *IEEE MTT-S Int. Microw. Symp. Dig.*, vol. 2. May 1990, pp. 841844.

[12] D. G. Smith, D. D. Heston, and D. L. Allen, "Designing high-power limiter circuits with GaAs PIN diodes," in *IEEE MTT-S Int. Microw. Symp. Dig.*, vol. 1. Jun. 1999, pp. 329332.

[13] J. Givernaud et al., "Microwave power limiting devices based on the semiconductormetal transition in vanadiumdioxide thin films," *IEEE Trans. Microw. Theory Techn.*, vol. 58, no. 9, pp. 23522361, Sep. 2010.

[14] A. Crunteanu et al., "Pulsed power operation of power limiters integrating a phase transition material," in *IEEE MTT-S Int. Microw. Symp. Dig.*, Jun. 2013, pp. 14.

[15] R. H. Caverly and M. J. Quinn, "Time domain modeling of PIN control and limiter diodes," in *IEEE MTT-S Int. Microw. Symp. Dig.*, vol. 2. Jun. 1999, pp. 719722.

[16] T. Lee, Synthesis for Microwave and Acoustic Wave Resonator Filters for Wireless Communication Systems, Ph.D. dissertation, School Electr. Comput. Eng., Purdue Univ., West Lafayette, IN, USA, August 2014

[17] H. W. Bode, *US. Patent 2,035,258*, March 24, 1936.

[18] H. W.Bode, *U.S. Putent2,002,216*,May21,1935.

[19] D. R. Jachowski, "Passive enhancement of resonator Q in microwave notch filters," in *IEEE MTT-S Int. Microw. Symp. Dig.*, Fort Worth, TX, USA, 2004, pp. 1315-1318 Vol.3.

[20] D. R. Jachowski, "Compact, frequency-agile, absorptive bandstop filters," in *IEEE MTT-S Int. Microw. Symp. Dig.*, 2005, Long Beach, CA, 2005, pp. 4 pp.-.

[21] T. Lee, J. Lee, E. J. Naglich and D. Peroulis, "Octave tunable lumped-element notch filter with resonator-Q-independent zero reflection coefficient," in *IEEE MTT-S Int. Microw. Symp. Dig.*, Tampa, FL, 2014, pp. 1-4.

[22] D. Psychogiou, R. Gmez-Garca and D. Peroulis, "RF-design of narrowband absorptive bandstop filters for UHF applications," *2015 IEEE 16th Annual Wireless and Microwave Technology Conference (WAMICON)*, Cocoa Beach, FL, 2015, pp. 1-4.

[23] M. D. Hickle and D. Peroulis, "Tunable absorptive bandstop filter with an ultra-broad upper passband," in *IEEE MTT-S Int. Microw. Symp. Dig.*, Honololu, HI, 2017, pp. 733-736.

[24] M. D. Hickle and D. Peroulis, "Theory and Design of Frequency-Tunable Absorptive Bandstop Filters," in *IEEE Transactions on Circuits and Systems I: Regular Papers*, vol. 65, no. 6, pp. 1862-1874, June 2018.

[25] E. J. Naglich, J. Lee, D. Peroulis and W. J. Chappell, "Switchless Tunable Bandstop-to-All-Pass Reconfigurable Filter," in *IEEE Transactions on Microwave Theory and Techniques*, vol. 60, no. 5, pp. 1258-1265, May 2012.

[26] E. J. Naglich, A. C. Guyette and D. Peroulis, "High-Q intrinsically-switched quasi-absorptive tunable bandstop filter with electrically-short resonators," *IEEE MTT-S Int. Microw. Symp. Dig.*, Tampa, FL, 2014, pp. 1-4.

[27] M. D. Hickle, M. D. Sinanis and D. Peroulis, "Design and implementation of an intrinsically-switched 2243 GHz tunable bandstop filter," *2016 IEEE 17th Annual Wireless and Microwave Technology Conference (WAMICON)*, Clearwater, FL, 2016, pp. 1-3.

[28] M. Hickle, M. Sinani, and D. Peroulis, "Tunable High-Isolation W-Band Bandstop Filters," in *IEEE MTT-S Int. Microw. Symp. Dig.*, Phoenix, AZ, 2015, pp. 1-4.

[29] M. D. Hickle and D. Peroulis, "Octave-tunable constant absolute bandwidth bandstop filter utilizing a novel passively-compensated coupling method," *IEEE MTT-S Int. Microw. Symp. Dig.*, San Francisco, CA, 2016, pp. 1-4.

[30] A. C. Guyette, E. J. Naglich and S. Shin, "RF-Power-Activated and Signal-Tracking Tunable Bandstop Filters," in *IEEE Transactions on Microwave Theory and Techniques*, vol. 65, no. 5, pp. 1534-1544, May 2017.

[31] G. Matthaei, L. Young, and E. M. Jones, in *Microwave Filters, Impedance Matching Networks, and Coupling Structures*. Norwoor, MA: Artech House, 1980.

[32] T. Lee, J. Lee and D. Peroulis, "Dynamic Bandpass Filter Shape and Interference Cancellation Control Utilizing BandpassBandstop Filter Cascade," in *IEEE Transactions on Microwave Theory and Techniques*, vol. 63, no. 8, pp. 2526-2539, Aug. 2015.

[33] E. J. Naglich and A. C. Guyette, "Reflection-Mode Bandstop Filters With Minimum Through-Line Length," in *IEEE Transactions on Microwave Theory and Techniques*, vol. 63, no. 10, pp. 3479-3486, Oct. 2015.

[34] E. J. Naglich, J. Lee, D. Peroulis and W. J. Chappell, "Extended Passband Bandstop Filter Cascade With Continuous 0.856.6-GHz Coverage," in *IEEE Transactions on Microwave Theory and Techniques*, vol. 60, no. 1, pp. 21-30, Jan. 2012.

[35] W. Yang, M. D. Hickle, D. Psychogiou and D. Peroulis, "L-band high-Q tunable quasi-absorptive bandstop-to-all-pass filter," *IEEE MTT-S Int. Microw. Symp. Dig.*, Honololu, HI, 2017, pp. 271-273.

[36] K. L. Kotzebue, "Frequency-selective limiting," *IEEE Trans. Microw. Theory Tech.*, vol. MTT-10, no. 6, pp. 516520, Nov. 1962.

[37] A. J. Giarola, "A review of the theory, characteristics, and operation of frequency selective limiters," *Proceedings of the IEEE*, vol. 67, no. 10, pp. 13801396, Oct. 1979.

[38] D. R. Jackson and R. W. Orth, "A frequency-selective limiter using nuclear magnetic resonance," *Proceedings of the IEEE*, vol. 55, no. 1, pp. 3645, Jan. 1967.

[39] A. Berman, "Multiple-carrier behavior of a frequency-selective ferrite limiter," *IEEE Transactions on Communications Systems*, vol. COM-12, no. 2, pp. 138150, Jun. 1964.

[40] S. N. Stitzer and H. Goldie, "A multi-octave frequency selective limiter," *IEEE MTT-S Int. Microw. Symp. Dig.*, Boston, MA, USA, 1983, pp. 326-328.

[41] J. D. Adam and S. N. Stitzer, "Frequency selective limiters for high dynamic range microwave receivers," *IEEE Trans. Microw. Theory Tech.*, vol. 41, no. 12, pp. 22272231, Dec. 1993.

[42] S. N. Stitzer, "Spike leakage and suppression in frequency selective limiters," *IEEE MTT-S Int. Microw. Symp. Dig.*, Boston, MA, USA, 2000, pp. 901-904 vol.2.

[43] J. D. Adam and S. N. Stitzer, "MSW frequency selective limiters at UHF," *IEEE Transactions on Magnetics*, vol. 40, no. 4, pt. 2, pp. 28442846, Jul. 2004.

[44] J. D. Adam and F. Winter, Magnetostatic wave frequency selective limiters, *IEEE Trans. Microw. Theory Tech.*, vol. 49, no. 3, pp. 956962, Mar. 2013.

[45] T. R. Billeter, "EPR frequency-selective limiter," *Proceedings of the IEEE*, vol. 56, no. 3, pp. 370371, Mar. 1968.

[46] F. Ramirez, R. Melville, A. Suarez, and J. S. Kenney, "Nonlinear analysis and design of frequency selective limiters based on parametric circuits," *IEEE MTT-S Int. Microw. Symp. Dig.*, Atlanta, GA, USA, 2008, pp. 947-950.

[47] A. Wolf and J. Pippin, "A passive parametric limiter," *1960 IEEE International Solid-State Circuits Conference. Digest of Technical Papers*, vol. 3. Feb. 1960, pp. 9091.

[48] P. Phudpong and I. C. Hunter, "Nonlinear Matched Reflection Mode Bandstop Filters for Frequency Selective Limiting Applications," *IEEE MTT-S Int. Microw. Symp. Dig.*, Honolulu, HI, 2007, pp. 1043-1046.

[49] P. Phudpong and I. C. Hunter, "Non Linear Bandstop Filters A New Method of Frequency Selective Limiting," *2006 European Microwave Conference*, Manchester, 2006, pp. 204-207.

[50] P. Phudpong and I. C. Hunter, "Frequency-Selective Limiters Using Nonlinear Bandstop Filters," *IEEE Trans. Microw. Theory Tech.*, vol. 57, no. 1, pp. 157-164, Jan. 2009.

[51] D. Lopez et al., "Ka Band power limiter for satellite channel amplifier," *2009 SBMO/IEEE MTT-S International Microwave and Optoelectronics Conference (IMOC)*, Belem, 2009, pp. 200-203.

[52] A. Hueltes et al., "Three-Port Frequency-Selective Absorptive Limiter," *IEEE Microwave and Wireless Components Letters*, vol. 27, no. 5, pp. 479-481, May 2017.

[53] E. J. Naglich and A. C. Guyette, "Frequency-Selective Limiters Utilizing Contiguous-Channel Double Multiplexer Topology," *IEEE Trans. Microw. Theory Tech.*, vol. 64, no. 9, pp. 2871-2882, Sept. 2016.

[54] X. Liu, L. P. B. Katehi, W. J. Chappell and D. Peroulis, "High-Q Tunable Microwave Cavity Resonators and Filters Using SOI-Based RF MEMS Tuners," in *Journal of Microelectromechanical Systems*, vol. 19, no. 4, pp. 774-784, Aug. 2010.

[55] M. A. Khater, Y. C. Wu and D. Peroulis, "Tunable Cavity-Based Diplexer With Spectrum-Aware Automatic Tuning," in *IEEE Trans. Microw. Theory Tech.*, vol. 65, no. 3, pp. 934-944, March 2017.

[56] M. A. Khater and D. Peroulis, "Pulse injection for real-time monitoring of tunable high-Q filters," in *Microw. Opt. Techn. Lett.*, vol. 56, no. 3, pp. 761764, Mar. 2014.

[57] M. Abu Khater and D. Peroulis, "Real-Time Feedback Control System for Tuning Evanescent-Mode Cavity Filters," in *IEEE Trans. Microw. Theory Tech.*, vol. 64, no. 9, pp. 2804-2813, Sept. 2016.

[58] X. Liu, L. P. B. Katehi, W. J. Chappell and D. Peroulis, "High- Q Tunable Microwave Cavity Resonators and Filters Using SOI-Based RF MEMS Tuners," in *Journal of Microelectromechanical Systems*, vol. 19, no. 4, pp. 774-784, Aug. 2010.

[59] W. J. Chappell, E. J. Naglich, C. Maxey and A. C. Guyette, "Putting the Radio in Software-Defined Radio: Hardware Developments for Adaptable RF Systems," in *Proceedings of the IEEE*, vol. 102, no. 3, pp. 307-320, March 2014.

[60] D. Peroulis, E. Naglich, M. Sinani and M. Hickle, "Tuned to Resonance: Transfer-Function-Adaptive Filters in Evanescent-Mode Cavity-Resonator Technology," in *IEEE Microwave Magazine*, vol. 15, no. 5, pp. 55-69, July-Aug. 2014.

[61] M. S. Arif and D. Peroulis, "A 6 to 24 GHz continuously tunable, microfabricated, high-Q cavity resonator with electrostatic MEMS actuation," in *IEEE MTT-S Int. Microw. Symp. Dig.*, 2012 IEEE MTT-S International, 2012, pp. 13.

[62] Z. Yang and D. Peroulis, "A 23-35 GHz MEMS Tunable All-Silicon Cavity Filter with Stability Characterization up to 140 Million Cycles," *IEEE MTT-S Int. Microw. Symp. Dig.*, 2014 IEEE MTT-S International, 2014.

[63] S. Saeedi, J. Lee, and H. Sigmarsson, "Broadband implementation of tunable, substrate-integrated, evanescent-mode, cavity bandpass filters," in *Microwave Conference (EuMC)*, 2014 44th European, 2014, pp. 849852.

[64] D. Psychogiou and D. Peroulis, "Tunable VHF Miniaturized Helical Filters," *IEEE Trans. Microw. Theory Tech.*, vol. 62, no. 2, pp. 282289, Feb. 2014.

[65] M. Abu Khater and D. Peroulis, "Vibration mitigation for evanescent-mode cavity filters," in *IEEE MTT-S Int. Microw. Symp. Dig.*, Tampa, FL, 2014, pp. 14.

[66] M. S. Arif and D. Peroulis, "All-Silicon Technology for High- Evanescent Mode Cavity Tunable Resonators and Filters," *J. Microelectromechanical Syst.*, vol. 23, no. 3, pp. 727739, Jun. 2014.

[67] E. J. Naglich, D. Peroulis, and W. J. Chappell, "Wide spurious free range positive-to-negative inter-resonator coupling structure for reconfigurable filters," in *IEEE MTT-S Int. Microw. Symp. Dig.*, Seattle, WA, 2013, pp. 1-4.

[68] E. J. Naglich, J. Lee, H. H. Sigmarsson, D. Peroulis, and W. J. Chappell, "Intersecting Parallel-Plate Waveguide Loaded Cavities for Dual-Mode and Dual-Band Filters," *IEEE Trans. Microw. Theory Tech.*, vol. 61, no. 5, pp. 18291838, May 2013.

[69] K. Chen, J. Lee, W. J. Chappell, and D. Peroulis, "Co-Design of Highly Efficient Power Amplifier and High- Output Bandpass Filter," *IEEE Trans. Microw. Theory Tech.*, vol. 61, no. 11, pp. 39403950, Nov. 2013.

[70] J. Small, M. S. Arif, A. Fruehling, and D. Peroulis, "A Tunable Miniaturized RF MEMS Resonator With Simultaneous High QU (500-735) and Fast Response Speed," *J. Microelectromechanical Syst.*, vol. 22, no. 2, pp. 395405, Apr. 2013.

[71] K. Chen, X. Liu, W. J. Chappell, and D. Peroulis, "Co-design of power amplifier and narrowband filter using high-Q evanescent-mode cavity resonator as the output matching network," in *IEEE MTT-S Int. Microw. Symp. Dig.*, 2011 IEEE MTT-S International, 2011, pp. 14.

[72] J. Lee, E. J. Naglich, H. H. Sigmarsson, D. Peroulis, and W. J. Chappell, "New Bandstop Filter Circuit Topology and Its Application to Design of a Bandstop-to-Bandpass Switchable Filter," *IEEE Trans. Microw. Theory Tech.*, vol. 61, no. 3, pp. 11141123, Mar. 2013.

[73] E. J. Naglich, D. Peroulis, and W. J. Chappell, "Low-Order Filter Response Enhancement in Reconfigurable Resonator Arrays," *IEEE Trans. Microw. Theory Tech.*, vol. 61, no. 12, pp. 43874395, Dec. 2013.

[74] T. Snow, J. Lee, and W. J. Chappell, "Tunable high quality-factor absorptive bandstop filter design," in *IEEE MTT-S Int. Microw. Symp. Dig.*, Montreal, QC, 2012, pp. 1-3.

[75] J. Small, W. Irshad, and D. Peroulis, "A fast high-Q X-band RF-MEMS reconfigurable evanescent-mode cavity resonator," in *IEEE MTT-S Int. Microw. Symp. Dig.*, Montreal, QC, 2012, pp. 1-3.

[76] E. J. Naglich, J. Lee, D. Peroulis, and W. J. Chappell, "Extended Passband Bandstop Filter Cascade With Continuous 0.85-6.6-GHz Coverage," *IEEE Trans. Microw. Theory Tech.*, vol. 60, no. 1, pp. 2130, Jan. 2012.

[77] E. J. Naglich, J. Lee, and D. Peroulis, "Tunable bandstop filter with a 17-to-1 upper passband," in *IEEE MTT-S Int. Microw. Symp. Dig.*, Montreal, QC, 2012, pp. 1-3.

[78] H. H. Sigmarsson, E. Naglich, J. Lee, D. Peroulis, and W. Chappell, "Tunable bandpass and bandstop filter cascade for dynamic pole allocation," in *2012 IEEE Antennas and Propagation Society International Symposium (APSURSI)*, 2012, pp. 12.

[79] X. Liu, E. Naglich, and D. Peroulis, "Non-linear effects in MEMS tunable bandstop filters," in *IEEE MTT-S Int. Microw. Symp. Dig.*, Montreal, QC, 2012, pp. 1-3.

[80] K. Chen, H. H. Sigmarsson, and D. Peroulis, "Power handling of high-Q evanescent-mode tunable filter with integrated piezoelectric actuators," in *IEEE MTT-S Int. Microw. Symp. Dig.*, Montreal, QC, 2012, pp. 1-3.

[81] X. Liu, L. P. B. Katehi, W. J. Chappell, and D. Peroulis, "Power Handling of Electrostatic MEMS Evanescent-Mode (EVA) Tunable Bandpass Filters," *IEEE Trans. Microw. Theory Tech.*, vol. 60, no. 2, pp. 270283, Feb. 2012.

[82] E. J. Naglich, J. Lee, D. Peroulis, and W. J. Chappell, "High-Q tunable bandstop filters with adaptable bandwidth and pole allocation," in *IEEE MTT-S Int. Microw. Symp. Dig.*, 2011 IEEE MTT-S International, 2011, pp. 14.

[83] J. Lee, E. J. Naglich, H. H. Sigmarsson, D. Peroulis, and W. J. Chappell, "Frequency-agile field-programmable filter array (FPFA) with multiple functionalities," in *IEEE MTT-S Int. Microw. Symp. Dig.*, Baltimore, MD, 2011, pp. 1-4.

[84] X. Liu, K. Chen, L. P. B. Katehi, W. J. Chappell, and D. Peroulis, "System-level characterization of bias noise effects on electrostatic RF MEMS tunable filters," in *2011 IEEE 24th International Conference on Micro Electro Mechanical Systems (MEMS)*, 2011, pp. 797800.

[85] X. Liu, J. Small, D. Berdy, L. P. B. Katehi, W. J. Chappell, and D. Peroulis, "Impact of Mechanical Vibration on the Performance of RF MEMS Evanescent-Mode Tunable Resonators," *IEEE Microw. Wirel. Compon. Lett.*, vol. 21, no. 8, pp. 406 408, Aug. 2011.

[86] M. S. Arif, W. Irshad, X. Liu, W. J. Chappell, and D. Peroulis, "A high-Q magnetostatically-tunable all-silicon evanescent cavity resonator," in *IEEE MTT-S Int. Microw. Symp. Dig.*, Baltimore, MD, 2011, pp. 1-4.

[87] J. Lee, E. J. Naglich, H. H. Sigmarsson, D. Peroulis, and W. J. Chappell, "Tunable Inter-Resonator Coupling Structure With Positive and Negative Values and Its Application to the Field-Programmable Filter Array (FPFA)," *IEEE Trans. Microw. Theory Tech.*, vol. 59, no. 12, pp. 33893400, Dec. 2011.

[88] W. Irshad and D. Peroulis, "A 12-18 GHz electrostatically tunable liquid metal RF MEMS resonator with quality factor of 1400-1840," in *IEEE MTT-S Int. Microw. Symp. Dig.*, Baltimore, MD, 2011, pp. 1-4.

[89] E. E. Hoppenjans and W. J. Chappell, "A vertically integrated tunable UHF filter," in *IEEE MTT-S Int. Microw. Symp. Dig.*, Anaheim, CA, 2010, pp. 1380-1383.

[90] H. H. Sigmarsson, J. Lee, D. Peroulis, and W. J. Chappell, "Reconfigurable-order bandpass filter for frequency agile systems," in *IEEE MTT-S Int. Microw. Symp. Dig.*, Anaheim, CA, 2010, pp. 1380-1383.

[91] S. Moon, H. H. Sigmarsson, H. Joshi, and W. J. Chappell, "Substrate Integrated Evanescent-Mode Cavity Filter With a 3.5 to 1 Tuning Ratio," *IEEE Microw. Wirel. Compon. Lett.*, vol. 20, no. 8, pp. 450452, Aug. 2010.

[92] X. Liu, L. P. B. Katehi, W. J. Chappell, and D. Peroulis, "High- Tunable Microwave Cavity Resonators and Filters Using SOI-Based RF MEMS Tuners," *J. Microelectromechanical Syst.*, vol. 19, no. 4, pp. 774784, Aug. 2010.

[93] E. J. Naglich, J. Lee, D. Peroulis, and W. J. Chappell, "Tunable, substrate integrated, high Q filter cascade for high isolation," in *IEEE MTT-S Int. Microw. Symp. Dig.*, Anaheim, CA, 2010, pp. 1380-1383.

[94] J. Lee, E. J. Naglich, and W. J. Chappell, "Frequency Response Control in Frequency-Tunable Bandstop Filters," *IEEE Microw. Wirel. Compon. Lett.*, vol. 20, no. 12, pp. 669671, Dec. 2010.

[95] E. J. Naglich, J. Lee, D. Peroulis, and W. J. Chappell, "A Tunable Bandpass-to- Bandstop Reconfigurable Filter With Independent Bandwidths and Tunable Response Shape," *IEEE Trans. Microw. Theory Tech.*, vol. 58, no. 12, pp. 3770 3779, Dec. 2010.

[96] H. Joshi, H. H. Sigmarsson, S. Moon, D. Peroulis, and W. J. Chappell, "Tunable high Q narrow-band triplexer," in *IEEE MTT-S Int. Microw. Symp. Dig.*, 2009. Boston, MA, 2009, pp. 1477-1480.

[97] H. Joshi, H. H. Sigmarsson, S. Moon, D. Peroulis, and W. J. Chappell, "High-Fully Reconfigurable Tunable Bandpass Filters," *IEEE Trans. Microw. Theory Tech.*, vol. 57, no. 12, pp. 35253533, Dec. 2009.

[98] H. H. Sigmarsson, A. Christianson, H. Joshi, S. Moon, D. Peroulis, and W. J. Chappell, "In-situ control of tunable evanescent-mode cavity filters using differential mode monitoring," in *IEEE MTT-S Int. Microw. Symp. Dig.*, 2009. Boston, MA, 2009, pp. 633636.

[99] X. Liu, L. P. B. Katehi, W. J. Chappell, and D. Peroulis, "Power handling capability of High-Q evanescent-mode RF MEMS resonators with flexible diaphragm," in *Microwave Conference*, 2009. APMC 2009. Asia Pacific, 2009, pp. 194197.

[100] X. Liu, L. P. B. Katehi, W. J. Chappell, and D. Peroulis, "A 3.4-6.2 GHz Continuously Tunable Electrostatic MEMS resonator with quality factor of $460-530$," in *IEEE MTT-S Int. Microw. Symp. Dig.*, 2009. Boston, MA, 2009, pp. 11491152.

[101] H. Joshi, H. H. Sigmarsson, D. Peroulis, and W. J. Chappell, "Highly Loaded Evanescent Cavities for Widely Tunable High-Q Filters," in *IEEE MTT-S Int. Microw. Symp. Dig.*, Honolulu, HI, 2007, pp. 2133-2136.

[102] E. J. Naglich, M. Sinani, S. Moon, and D. Peroulis, "High-Q MEMS-tunable W-band bandstop resonators," in *IEEE MTT-S Int. Microw. Symp. Dig.*, Tampa, FL, 2014, pp. 1-3.

[103] M. D. Hickle and D. Peroulis, "A widely-tunable substrate-integrated balun filter," *IEEE MTT-S Int. Microw. Symp. Dig.*, Honololu, HI, 2017, pp. 274-277.

[104] M. Abdelfattah, M. Hickle, M. D. Sinanis, Y. Wu and D. Peroulis, "A 1220 GHz Passively-compensated Tunable Bandstop Filter with 40-dB Notch Level," *IEEE MTT-S Int. Microw. Symp. Dig.*, Philadelphia, PA, 2018, pp. 571-574.

[105] W. Yang, M. A. Khater, E. J. Naglich, D. Psychogiou, D. Peroulis, "Frequency-Selective Limiters using Triple-Mode Filters" *IEEE Trans. Microw. Theory Tech.*, submitted.

[106] A. Semnani, M. Abu Khater, Y. Wu and D. Peroulis, "An Electronically Tunable High-Power Impedance Tuner With Integrated Closed-Loop Control," in *IEEE Microwave and Wireless Components Letters*, vol. 27, no. 8, pp. 754-756, Aug. 2017.

[107] X. Gong, A. Margomenos, B. Liu, S. Hajela, L. P. B. Katehi, and W. J. Chappell, "High-Q evanescent-mode filters using silicon micromachining and polymer stereolithography (SL) processing," *IEEE Transactions on Microwave Theory and Techniques*, vol. 52, no. 11, pp. 25572566, 2004.

[108] E. Kemppinen and S. Leppvuori, "Coaxial Resonator Method to Determine Dielectric Properties of High Dielectric Constant Microwave Ceramics," *Int. J. High Technol. Ceram.*, 2, 143-55 (1986).

[109] G. J. Slogget, N. G. Barton, and S. J. Spencer, "Fringing fields in disc capacitors," *J. Phys. A, Math. General*, vol. 19, no. 14, pp. 27252736, 1986.

[110] M. Abdelfattah and D. Peroulis, "A Novel Independently-Tunable Dual-Mode SIW Resonator with a Reconfigurable Bandpass Filter Application," *IEEE MTT-S Int. Microw. Symp. Dig.*, Philadelphia, PA, 2018, pp. 1091-1094.

[111] F. Tefiku and E. Yamashita, "Capacitance characterization method for thick-conductor multiple planar ring structures on multiple substrate layers," in *IEEE Transactions on Microwave Theory and Techniques*, vol. 40, no. 10, pp. 1894-1902, Oct. 1992.

[112] M. Abdelfattah and D. Peroulis, "High-Q Tunable Evanescent-Mode Cavity SIW Resonators and Filters with Contactless Tuners," *IEEE Trans. Microw. Theory Tech.*, submitted.

[113] S. Saeedi, J. Lee and H. Sigmarsson, "Prediction of power handling in tunable, high-Q, substrate-integrated, evanescent-mode cavity bandpass filters," in *Electronics Letters*, vol. 52, no. 10, pp. 846-848, 12 5 2016.

[114] K. Chen, A. Semnani and D. Peroulis, "High-power microwave gas discharge in high-Q evanescent-mode cavity resonators and its instantaneous/long-term effects," *IEEE MTT-S Int. Microw. Symp. Dig.*, Seattle, WA, 2013, pp. 1-4.

[115] M. Abu Khater and D. Peroulis, "Vibration mitigation for evanescent-mode cavity filters," *IEEE MTT-S Int. Microw. Symp. Dig.*, Tampa, FL, 2014, pp. 1-4.

[116] "Micro Linear Actuator," *New Scale Technologies.* [Online]. Available: https://www.newscaletech.com/micro-motion-modules/m3-l-linear-smart-actuators/. [Accessed: 10-Feb-2019].

[117] P. Adhikari, W. Yang, Y. Wu and D. Peroulis, "A PCB Technology-Based 2242-GHz Quasi-Absorptive Bandstop Filter," in *IEEE Microwave and Wireless Components Letters*, vol. 28, no. 11, pp. 975-977, Nov. 2018.

[118] S. Saeedi, S. Atash-bahar and H. H. Sigmarsson, "Active tunable substrate integrated evanescent-mode cavity resonator using negative resistance," *2016 IEEE Radio and Wireless Symposium (RWS)*, Austin, TX, 2016, pp. 87-90.

[119] E. J. Naglich and A. C. Guyette, "Reflection-Mode Bandstop Filters With Minimum Through-Line Length," in *IEEE Trans. Microw. Theory Tech.*, vol. 63, no. 10, pp. 3479-3486, Oct. 2015.

[120] A. Atia, and A. Williams, "Nonminimum-Phase Optimum-Amplitude Bandpass Waveguide Filters," in *Microwave Theory and Techniques, IEEE Transactions on* , vol.22, no.4, pp.425-431, April 1974.

[121] A. Atia and A. Williams, "Narrow-Bandpass Waveguide Filters," in *Microwave Theory and Techniques*, IEEE Transactions on , vol.20, no.4, pp.258-265, April 1972.

[122] R. J. Cameron, "General coupling matrix synthesis methods for Chebyshev filtering functions," in *Microwave Theory and Techniques, IEEE Transactions on*, vol.47, no.4, pp.433-442, April. 1999.

[123] R. J. Cameron, "Advanced coupling matrix synthesis techniques for microwave filters," in *Microwave Theory and Techniques, IEEE Transactions on*, vol.51, no.1, pp.1-10, January 2003.

[124] T. -C. Lee, J. Lee, and D. Peroulis, "Dynamic Bandpass Filter Shape and Interference Cancellation Control Utilizing BandpassBandstop Filter Cascade," in *Microwave Theory and Techniques, IEEE Transactions on* , vol.63, no.8, pp.2526-2539, August 2015.

[125] E. J. Naglich, J. Lee, D. Peroulis and W. J. Chappell, "Switchless Tunable Bandstop-to-All-Pass Reconfigurable Filter," in *IEEE Transactions on Microwave Theory and Techniques*, vol.60, pp.1258-1265, May 2012.

APPENDICES

A. COUPLING DIAGRAMS

The coupling diagram is used to visualize the resonator-based filter. It is also a diagram representation of the filter synthesized by coupling matrix. The nodes of the filter are the ports, resonators, and non-resonant nodes of the circuit. An example of a coupling-routing diagram for a conventional 4-pole series-coupled bandstop filter topology is shown in Fig. A.1. The ports of the filter network are represented by white circles. Here, S is the source port and L is the load port. Resonators are represented by black circles and are numbers. Couplings between ports and resonators and between resonators are represented by solid black lines. Couplings can also be transmission lines. The basic operation of the circuit can be intuitively understood from the coupling diagram.
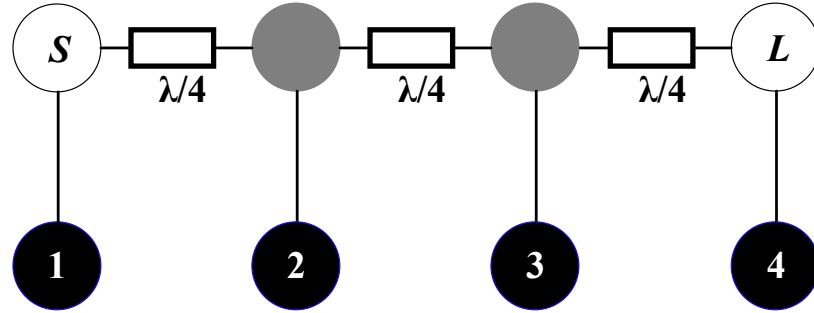
Fig. A.1. Coupling diagram for a conventional 4-pole series-coupled bandstop filter topology.

B. COUPLING MATRIX SYNTHESIS

The coupling matrix synthesis is used to synthesize resonator-based filters, and pro-
vides a one-to-one correspondence between its coefficients and the physical resonators
and coupling structures. The coupling matrix synthesis is explained in detail in this
Appendix. The content of this Appendix is reference to the author's Master's thesis.

B.1   Polynomials
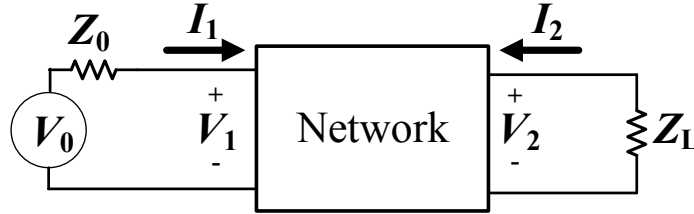
Fig. B.1. Circuit of a lossless two-port network.

A lossless two-port network is shown in Fig. B.1 with a resistor termination of Z_L
and a source resistance of Z_0. The maximum available power P_{max} from the voltage
source is $V_0^2/4Z_0$. If P_L is defined as the output power, which should be equal to or
smaller than P_{max}, a transducer function $H(s)$ can be defined as

$$|H(S)|_{(S=j\Omega)^2} = P_{max}/P_L, \tag{B.1}$$

where $S = j\Omega$ is the normalized complex frequency and $j^2 = -1$.

If assumed that the system is linear, lumped and time-invariant, the transfer function can be rewritten as a ratio of the input and output voltage, or a rational polynomial functions

$$H(S) = \frac{V_1}{V_2} = \frac{b_n S^n + b_{n-1} S^{n-1} + ... + b_1 S^1 + b_0}{a_m S^m + a_{m-1} S^{m-1} + ... + a_1 S^1 + a_0}, \tag{B.2}$$

where $S = \sigma + j\Omega$ is a complex frequency variable and $t(S)$ is defined as the transmission coefficient. For a lossless passive network, $\sigma = 0$ and thus $S = j\Omega$.

For a given transfer function (B.2), the insertion loss of the filter can be given in decibels (dB) as

$$L_A(\Omega) = 10 \, log_{10} \frac{1}{|t(j\Omega)|^2}, \tag{B.3}$$

or in terms of transfer function as

$$L_A(\Omega) = 10 \, log_{10} |H(j\Omega)|. \tag{B.4}$$

In filter design, it is usually assumed that there is no insertion loss in the pass-band of the filter. Therefore, the input-to-output transfer function is unity in the pass-band

$$H(S) = 1. \tag{B.5}$$

This constant term can be eliminated by redefine the transfer function as

$$H(S)H(-S) = 1 + K(S)K(-S). \tag{B.6}$$

Since $H(S)$ and $K(S)$ are rational functions with same denominators, if the transfer function is expressed as

$$H(S) = \frac{E(S)}{P(S)}, \tag{B.7}$$

where $E(S)$ and $P(S)$ are polynomials, then the characteristic function is expressed as

$$K(S) = \frac{F(S)}{P(S)}. \tag{B.8}$$

Inserting (B.7) and (B.8) into (B.6), it is obtained that

$$E(S)E(-S) = P(S)P(-S) + F(S)F(-S). \tag{B.9}$$

Inserting (B.6) into (B.4), the insertion loss can be expressed as

$$L_A(\Omega) = 10 \ log_{10}|K(j\Omega)|^2. \tag{B.10}$$

The zeroes of $K(j\Omega)$ are reflection zeroes.

In transmission line theory, the reflection coefficient $\rho(S)$ is defined as the ratio of the reflection wave to the incident wave at a specified location in the system. The transmission coefficient is defined as the ratio of the transmitted wave to the incident wave. They are given by

$$\rho(S) = \frac{reflectedwave}{incidentwave} = \frac{F(S)}{E(S)}, \tag{B.11}$$

$$t(S) = \frac{transmittedwave}{incidentwave} = \frac{P(S)}{E(S)}. \tag{B.12}$$

In a lossless system, the reflection and transmission coefficient satisfy the following condition

$$|\rho(S)|^2 + |t(S)|^2 = 1, \tag{B.13}$$

and the insertion loss and the return loss are related by

$$L_A(\Omega) = -10 \log\left(1 - 10^{-L_R(\Omega)/10}\right) \tag{B.14}$$

$$L_R(\Omega) = -10 \log\left(1 - 10^{-L_A(\Omega)/10}\right), \tag{B.15}$$

where $L_A(\Omega)$ is the insertion loss, and $L_R(\Omega)$ is the return loss.

B.1.1   Characteristics of Polynomials

The values of S at which the numerator of the polynomial function $H(S)$ becomes zero are the transmission zeros, or attenuation poles; the values of S for which the denominator of the polynomial function $H(S)$ becomes zero are the transmission poles, or reflection zeros. Therefore, the zeros of $t(S)$ are the roots of the numerator $P(S)$ and the poles of $t(S)$ are the roots of denominator $E(S)$. To have a stable filter system, transmission poles must lie in the left half of the phase-plane, or on the

imaginary axis. Hence, $E(S)$ is a Hurwitz polynomial with degree N. Based on filter design specifications, the roots of $F(S)$ lie on the imaginary axis of where the degree is N, and the roots of $P(S)$ lie on the imaginary axis. With $F(S)$ and $P(S)$, the polynomial $E(S)$ can be calculated by (B.9).

B.1.2 Normalization of Polynomials

The transfer function and the characteristic function are related according to (B.6) as

$$|H(S)|^2 = 1 + |K(S)|^2. \tag{B.16}$$

To generalize the transfer function, a constant factor ε is introduced as a ripple factor and the relationship in (B.16) becomes

$$|H(S)|^2 = 1 + \varepsilon^2 |K(S)|^2. \tag{B.17}$$

In a filter synthesis procedure, the highest coefficient of the polynomials, $F(S)$ and $P(S)$, are normalized to unity. The ratio of the extracted highest coefficients of these two polynomials is defined as the ripple factor, or ε. Ripple factor describes the maximum attenuation of the filter response. From (B.17), the transmitted power can be updated as

$$|t(S)|^2 = \frac{1}{\varepsilon^2} \frac{|P(S)|^2}{|E(S)|^2} = \frac{1}{1 + \varepsilon^2 |K(S)|^2}, \tag{B.18}$$

where

$$|E(S)|^2 = \frac{|P(S)|^2}{\varepsilon^2} + |F(S)|^2. \tag{B.19}$$

From (B.18) and (B.19), the transmission and reflection coefficients are given by

$$t(S) = \frac{1}{\varepsilon} \frac{|P(S)|}{|E(S)|}, \rho(S) = \frac{1}{\varepsilon} \frac{|F(S)|}{|E(S)|}. \tag{B.20}$$

In different types of filters, ε indicates different aspects. For a Chebyshev filter, ε determines the magnitude of the ripple in the passband. For a Butterworth filter, ε determines the maximum permissible ripple. For example, if the filter is designed to

have a maximum ripple of A_1 dB, or return loss R_1 dB at the edge of the passband at its unity cutoff frequency Ω_1, then

$$|t(j\Omega)|^2 = \frac{1}{1 + \varepsilon^2 |K(j\Omega)|^2} = 10^{-A_1/10}. \tag{B.21}$$

Therefore, in terms of maximum ripple, the ripple constant is

$$\varepsilon = \sqrt{\frac{10^{A_1/10} - 1}{|K(j\Omega)|^2}}. \tag{B.22}$$

B.2 Low-pass Filter Prototype

The low-pass filter prototype is created in a normalized frequency domain in classic filter synthesis. The ideal filtering function in the frequency spectrum is shown in Fig. B.2, where in the interested frequency regime, the passband is flat and outside the regime the isolation is infinite. In reality, it is very hard to achieve a vertical cutoff. Instead, transfer functions that are approximate to the ideal response are calculated. In this section, an approach for obtaining such transfer functions are explained in detail. Several known formulas are presented.
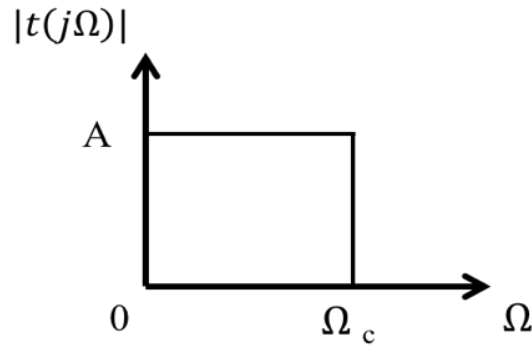

Fig. B.2. Ideal frequency response of a low-pass filter.

B.2.1 All-Pole Filters

All-pole filters are the most fundamental type of filters. These filters have all of their transmission zeros at infinity. Thus, the transfer function can be simplified as

$$t(S) = \frac{P(S)}{E(S)} = \frac{1}{E(S)}. \tag{B.23}$$

There, the frequency response of the filter is determined by the polynomial $F(S)$. The characteristic function (B.8) can be simplified as

$$K(S) = F(S). \tag{B.24}$$

When all the roots of polynomial $F(S)$ are located at the origin, this type of frequency response is a maximally-flat response, and it is named the Butterworth response. For an Nth-order Butterworth filter response, the characteristic function is given by

$$K(S) = S^N, \tag{B.25}$$

and the transmitted power is given by

$$|t(S)|^2 = \frac{1}{1 + S^{2N}}, \tag{B.26}$$

For a Butterworth filter, its $2N$ zeros S_k are located on the unit circle, and their positions are given by

$$S_k = \begin{cases} exp[\frac{j\pi}{2N}(2k-1)], & \text{if n is even,} \\ exp[\frac{j\pi}{2N}(2k)], & \text{if n is odd.} \end{cases} \tag{B.27}$$

To maintain a stable response, the zeros only located on the left side of the S-plane are chosen. For a Butterworth filter response, half of the power is transmitted at the cutoff frequency. The frequency responses of normalized 2nd-, 3rd-, and 4th-order Butterworth filters are plotted in Fig. B.3.

When the roots of polynomial $F(S)$ are positioned in such that the frequency response in the passband is equi-ripple, then this response is known as a Chebyshev response. For a Chebyshev filter, the characteristic function becomes

$$T_n(\omega) = \begin{cases} cos(ncos^{-1}\omega), & 0 \le |\omega| \le 1 \\ cosh(ncosh^{-1}\omega), & 1 < |\omega|. \end{cases} \tag{B.28}$$
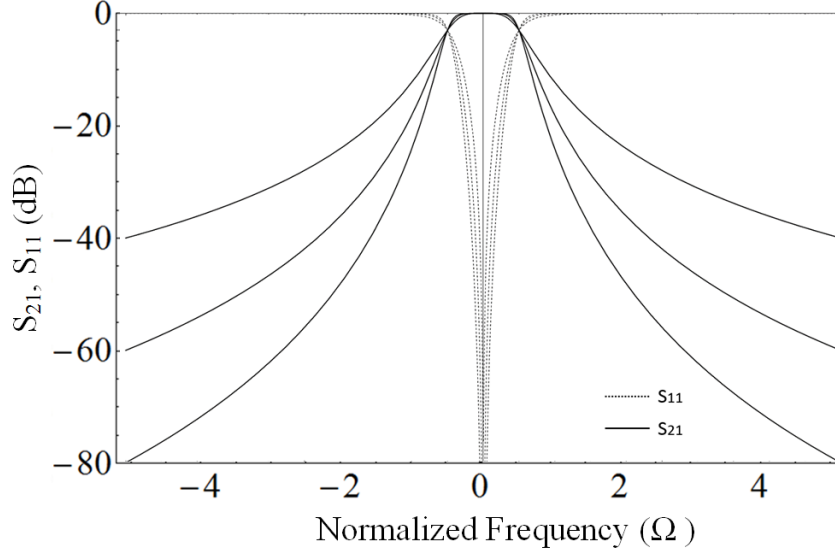
Fig. B.3. Butterworth responses for 2nd-, 3rd-, and 4th-order lowpass filter.

And the transmitted power is given by

$$|t(S)|^2 = \frac{1}{1 + \varepsilon^2 T_n^2}. \tag{B.29}$$

The pole locations of a Chebyshev filter are

$$S_k = \pm sinh(y)sin(x_k) \pm jcosh(y)cos(x_k), \tag{B.30}$$

where

$$x_k = \frac{\pi}{2}\frac{2k-1}{N}, y = \frac{1}{N}sinh^{-1}\frac{1}{\varepsilon}. \tag{B.31}$$

Figure B.4 shows the low-pass response of a 4th-order Chebyshev filter with 20 dB equi-ripple return loss. The poles in Fig. B.4 are located at S=j0.9239 and S=j0.3827. The ripple constant is calculated from B.22 as $\varepsilon = 0.80425$.

B.2.2 Filters with Transmission Zeros

The characteristic function of the filters with transmission zeros is given by

$$K(S) = \frac{F(S)}{P(S)} = \frac{(S - S_{z1})(S - S_{z2})...(S - S_{zn})}{(S - S_{p1})(S - S_{p2})...(S - S_{pm})}, \tag{B.32}$$
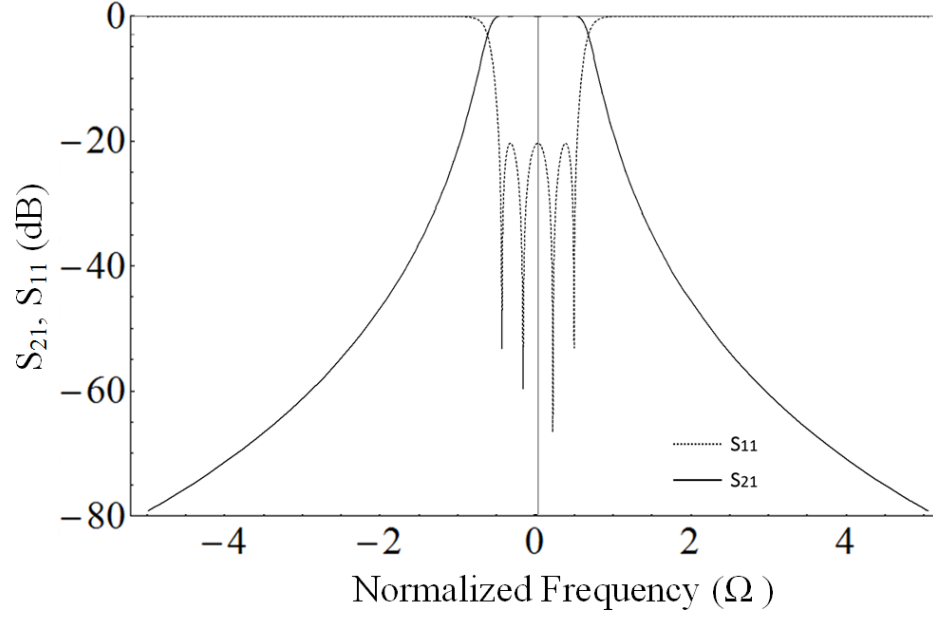
Fig. B.4. Chebyshev response of 4th-order low-pass filter.

where m represents the number of transmission zeros at finite frequency. m should be equal to or less than n. Filters can be designed with equi-ripple response in either passband, stopband, or both. A filter with equi-ripple in both passband and stopband is known as an elliptic filter. In practice, filters are usually designed with non-equi-ripple response in stopband for better near-band rejection and selectivity.

Figure B.5 shows a 4th-order Chebyshev filter with four transmission zeros at $S_p = \pm 2.5$ and ± 6. The reflection zeros for equi-ripple response in the passband remain the same as in conventional 4th-order Chebyshev filter response.

In general, filters with transmission zeros have higher selectivity near the passband than the all-pole filters. However, the all-pole filters have better wide-band selectivity.

B.3 Coupling Matrix

In 1974, Williams and Atia introduced the coupling matrix concept and applied it to dual-mode, narrow-band, waveguide, bandpass filters [120] [121]. Modeling
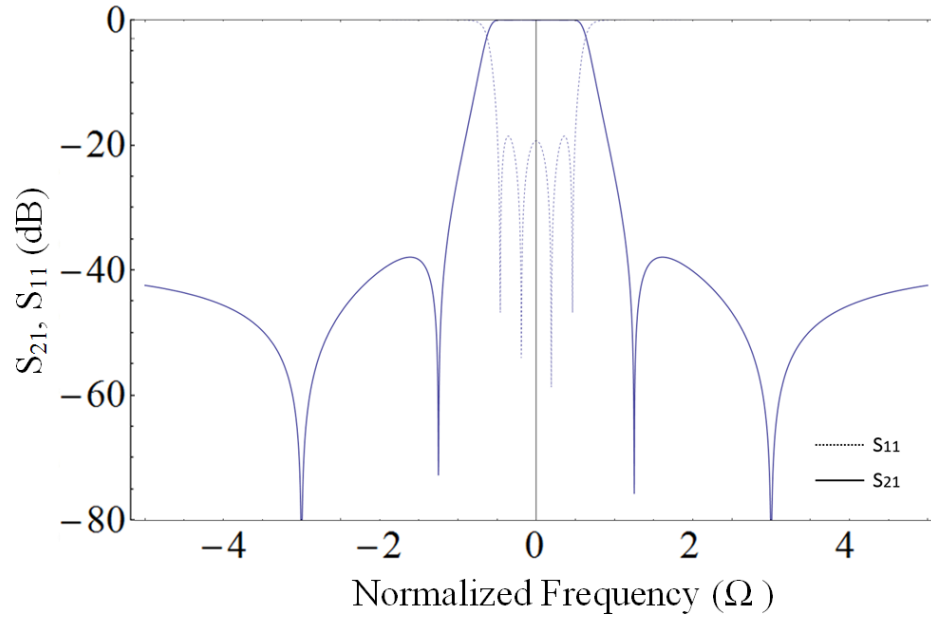
Fig. B.5. Generalized Chebyshev response of the 4th-order low-pass filter with transmission zeros at $Sp = \pm 2.5$ and ± 6.

the circuit in matrix form benefits from matrix operations properties. The coupling matrix provides a one-to-one correspondence among its elements. This is a significant advancement because it allows for direct modeling of not only the resonators but also their couplings. This enables faster synthesis for advanced filtering transfer functions. Cameron later developed general techniques to synthesize and generate the coupling matrix in an efficient fashion. The synthesis is performed in the low-pass domain, where different topologies may be conveniently obtained using similarity transformations [122,123]. This section will discuss the coupling matrix filter synthesis in detail.

B.3.1 Circuit Model

A coupling matrix can be extracted from the voltage-current relationship of the equivalent circuit model. Such an equivalent circuit is shown in Fig. B.6. The circuit

Fig. B.6. Equivalent circuit model of a multi-coupled network.

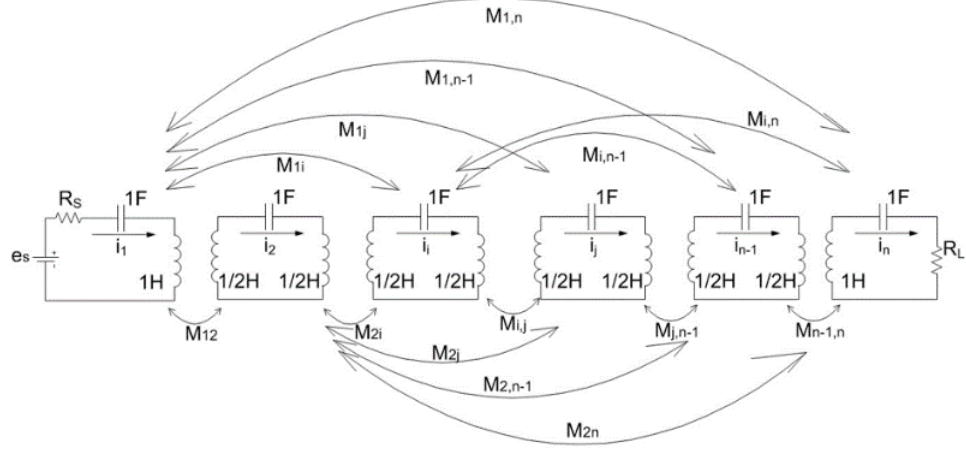is driven by an open-circuit voltage source e_s with an internal resistance of R_s and terminated by a load resistance R_L.

Individual resonators are composed of 1 Henry (H) inductors and 1 Farad (F) capacitors, producing a normalized resonant frequency of 1 radian/second (rad/s). The current in each resonator is labeled as i_n. Couplings between each two resonators are denoted as $M_{(i,j)}$, where i and j denote resonator numbers. The bandwidth of the filter is frequency independent and normalized to 1 rad/s. The voltage-current relationship in the network can be expressed in matrix form as

$$
\begin{bmatrix} e_s \\ 0 \\ 0 \\ \vdots \\ 0 \end{bmatrix} = \begin{bmatrix} R_s + s & jM_{1,2} & \cdots & jM_{1,n-1} & jM_{1,n} \\ jM_{2,1} & s & \cdots & jM_{2,n-1} & jM_{2,n} \\ \vdots & \vdots & \ddots & \vdots & \vdots \\ jM_{n-1,1} & jM_{n-1,2} & \cdots & s & jM_{1,n} \\ jM_{n,1} & jM_{n,2} & \cdots & jM_{n,n-1} & R_L + s \end{bmatrix} \begin{bmatrix} i_1 \\ i_2 \\ i_3 \\ \vdots \\ i_n \end{bmatrix} \tag{B.33}
$$

The voltage-current relationship in B.33 can be written in simplified form as

$$
E = ZI = (sU + R + jM)I, \tag{B.34}
$$

where U is the extended N by N identity matrix, R represents source and load, and M is the coupling matrix. And they are

$$U = \begin{bmatrix} 0 & 0 & \cdots & 0 & 0 \\ 0 & 1 & \cdots & 0 & 0 \\ \vdots & \vdots & \ddots & \vdots & \vdots \\ 0 & 0 & \cdots & 1 & 0 \\ 0 & 0 & \cdots & 0 & 0 \end{bmatrix} \tag{B.35}$$

$$R = \begin{bmatrix} R_s & 0 & \cdots & 0 & 0 \\ 0 & 0 & \cdots & 0 & 0 \\ \vdots & \vdots & \ddots & \vdots & \vdots \\ 0 & 0 & \cdots & 0 & 0 \\ 0 & 0 & \cdots & 0 & R_L \end{bmatrix} \tag{B.36}$$

$$M = \begin{bmatrix} 0 & M_{1,2} & \cdots & M_{1,n-1} & M_{1,n} \\ M_{2,1} & 0 & \cdots & M_{2,n-1} & M_{2,n} \\ \vdots & \vdots & \ddots & \vdots & \vdots \\ M_{n-1,1} & M_{n-1,2} & \cdots & 0 & M_{1,n} \\ M_{n,1} & M_{n,2} & \cdots & M_{n,n-1} & 0 \end{bmatrix} \tag{B.37}$$

Since all series resonators have the same resonant frequency, this filter is synchronously tuned. Also, all the resonators have the same quality factor, coupling structures, and characteristic impedance.

B.3.2   Coupling Matrix to Scattering Parameter

The overall circuit including the source impedance R_s and load impedance R_L is represented by a Z-matrix. This matrix includes an impedance matrix that represents a purely-reactive network between source and load. The equation B.34 can be rewritten as

$$I = Z^{-1}E, \tag{B.38}$$

where Z^{-1} is the reverse impedance matrix. The current in the first loop and the last loop is given by

$$i_1 = Z_{11}^{-1} e_s \tag{B.39}$$

$$i_n = Z_{n1}^{-1} e_s. \tag{B.40}$$

The transmission coefficient S_{21} is described as

$$S_{21} = 2\sqrt{\frac{R_s}{R_L}} \frac{V_n}{e_s} = 2\sqrt{\frac{R_s}{R_L}} R_L Z_{n1}^{-1} = 2\sqrt{R_s R_L} Z_{n1}^{-1}. \tag{B.41}$$

The reflection coefficient S_{11} is defined as

$$S_{11} = \frac{Z_{11} - R_s}{Z_{11} + R_s} = 1 - \frac{2R_s}{Z_{11} + R_s}, \tag{B.42}$$

where Z_{11} is the impedance looking in at the input port. Z_{11} is the ratio of V_1 and i_1 in the first loop. Therefore Z_{11} can be written as

$$Z_{11} = \frac{V_1}{i_1} = \frac{e_s Z_{11}}{Z_{11} + R_s} \frac{1}{Z_{11}^{-1} e_s}. \tag{B.43}$$

From B.43, it can be found that

$$Z_{11}^{-1} = \frac{1}{Z_{11} + R_s}. \tag{B.44}$$

Substituting B.44 into B.42, the reflection coefficient is obtained as

$$S_{11} = 1 - 2R_s Z_{11}^{-1}. \tag{B.45}$$

Filter synthesizing procedure starts with the characteristic function. Characteristic polynomials are derived from the characteristic function. The coupling coefficients are obtained by mapping the calculated transmission and reflection coefficients from the coupling matrix to the characteristic polynomials. Both analytic or optimization methods can be used. For optimization methods, a cost function can be used for filter synthesis [?]. The following sections introduce some advanced coupling matrix techniques which are helpful in the filter topologies synthesized in this dissertation.

B.3.3 Finite Resonator Quality Factors

The basic coupling matrix is defined with lossless resonators. In reality, resonators have finite unloaded quality factors (Q), which results in insertion loss for bandpass filters and less notch attenuation level for bandstop filters. Some filter topologies incorporates Q as a design parameter to optimize overall performance, such as absorptive bandstop filter topologies [**?**]. Therefore it is useful to introduce Q to the coupling matrix. It should be noted that bandwidth and Q have a combined effect on insertion loss. So new terms are added to the coupling matrix that depend on both Q and the fractional bandwidth. The new coupling matrix is described as

$$
M = \begin{bmatrix}
0 & M_{1,2} & \cdots & M_{1,n-1} & M_{1,n} \\
M_{2,1} & \frac{-j}{Q\Delta} & \cdots & M_{2,n-1} & M_{2,n} \\
\vdots & \vdots & \ddots & \vdots & \vdots \\
M_{n-1,1} & M_{n-1,2} & \cdots & \frac{-j}{Q\Delta} & M_{1,n} \\
M_{n,1} & M_{n,2} & \cdots & M_{n,n-1} & 0
\end{bmatrix}
\tag{B.46}
$$

where Q is the quality factor, and Δ is the fractional bandwidth of designed filter.

B.3.4 Asynchronous Resonator Frequency Tuning

The coupling matrix is defined based on the assumption that all the resonators have the same resonant frequency. Recent development in tunable bandpass-bandstop filter cascade [124], tunable bandstop-to-all-pass filter [125], and other advanced tunable filter topologies required asynchronous resonator tunings. Thus it is desired to add asynchronous tuning capability in the coupling matrix. The asynchronous tuning is approximated as a self-coupling terms $M_{n,n}$ in the coupling matrix. It should be noted that this self-coupling term is a real number used to tune a specific resonator away from the normalized center frequency. An imaginary number denotes loss in a

particular resonator as described in the previous section. With self-coupling term, the new coupling matrix is described as

$$M = \begin{bmatrix} 0 & M_{1,2} & \cdots & M_{1,n-1} & M_{1,n} \\ M_{2,1} & M_{2,2} & \cdots & M_{2,n-1} & M_{2,n} \\ \vdots & \vdots & \ddots & \vdots & \vdots \\ M_{n-1,1} & M_{n-1,2} & \cdots & M_{n-1,n-1} & \\ M_{n,1} & M_{n,2} & \cdots & M_{n,n-1} & 0 \end{bmatrix} \quad (B.47)$$

The self-coupling terms can have both a real and imaginary part to model both finite Q and asynchronous tuning at the same time.

B.3.5 Non-Resonating Nodes

The coupling matrix filter synthesis method is based on narrow-band approximation, and all the coupling values have a phase shift of $\pm$ 90 degrees. To synthesis higher-order bandstop filters, non-resonating nodes (NRNs) are used, as shown in Fig. B.7. The NRN can also be used to model transmission lines that have a phase shift of multiple $\pm$ 90 degrees. The NRN is implemented in U matrix as 0 rather than 1.
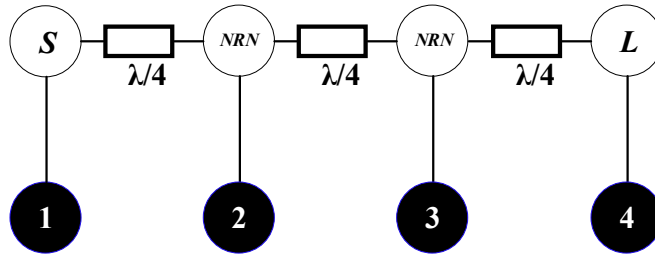

Fig. B.7. Filter topology of the 4th-order bandstop filter with two NRNs.

C. COUPLING MATRIX SYNTHESIS OF THE HIGHER-ORDER TRIPLET TOPOLOGIES

In Chapter 2 the coupling matrix synthesis of a second-order absorptive bandstop-to-all-pass filter is introduced. The advanced coupling matrix techniques enable syntheses of filters with arbitrary coupling phases. The extension of the theoretical work is to synthesize the high-order bandstop-to-all-pass filters. In order to achieve better selectivity or wider bandwidth, higher order approaches are desired. With the absorptive response, the second-order filter can provide very high isolation level with very narrow bandwidth. With Chebyshev response, the second-order filter can give wider bandwidth while sacrificing the isolation level at the center frequency. If both bandwidth and isolation level are demanded, a fourth-order or higher-order filter can satisfy both of the criteria. However, the trade-off is that the all-pass in-band insertion loss will be slightly increased. The following analysis is original work by the author.

A way to increase the order of the triplet topology to achieve both the bandstop and the all-pass responses is shown in Fig. C.1. Since this is a bandstop topology, it is relatively easier to synthesize the bandstop response. Therefore, the all-pass response is synthesize first, and the conditions are used to synthesize the bandstop response.
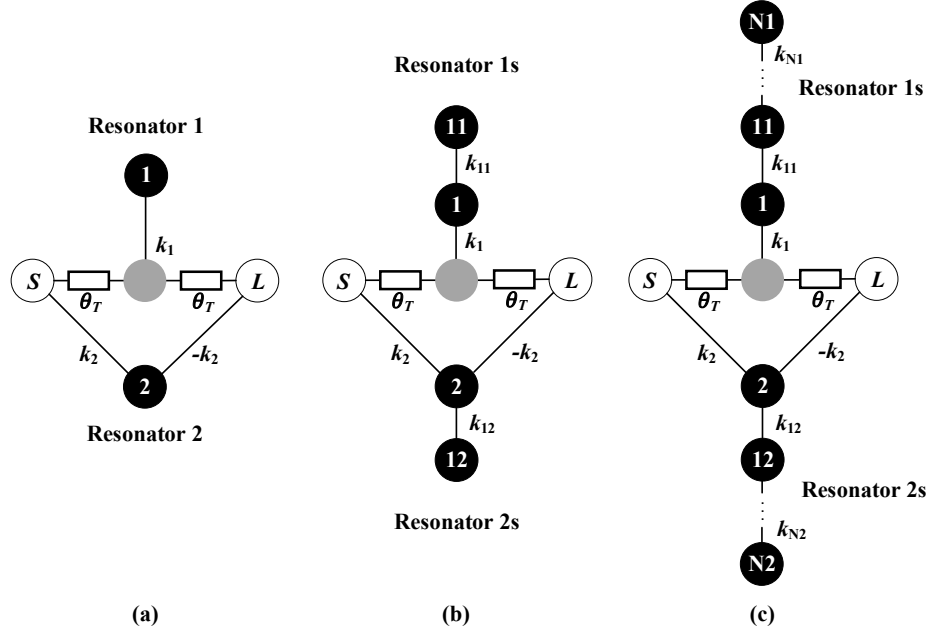
Fig. C.1. Coupling diagram of the absorptive bandstop-to-all-pass topology of (a) second order and (b) fourth order.

C.1 All-Pass Synthesis

The coupling matrix of the fourth-order triplet topology with θ_T equal to 90 degree and ideal resonators is given by

$$
M = \begin{bmatrix}
0 & 0 & 1 & k_2 & 0 & 0 & 0 \\
0 & B_1 & k_1 & 0 & k_{11} & 0 & 0 \\
1 & k_1 & 0 & 0 & 0 & 0 & 1 \\
k_2 & 0 & 0 & B_2 & 0 & k_{22} & -k_2 \\
0 & k_{11} & 0 & 0 & B_{11} & 0 & 0 \\
0 & 0 & 0 & k_{22} & 0 & B_{22} & 0 \\
0 & 0 & 1 & -k_2 & 0 & 0 & 0
\end{bmatrix}
\tag{C.1}
$$

The transmission and reflection coefficients are given by

$$
S_{21} = -\frac{s^4 + (k_{11}^2 + k22^2 - k_1^2 k_2^2)}{[s^2 + 2k_2^2 s + k22^2][s^2 + 0.5k_1^2 s + k11^2]},
\tag{C.2}
$$

and

$$S_{11} = \frac{(k_1^2 + 4k_2^2)s^3 + (4k_{11}^2 k_2^2 - k_1^2 k_{22}^2)s}{[s^2 + 2k_2^2 s + k22^2][s^2 + 0.5k_1^2 s + k11^2]}. \tag{C.3}$$

The conditions to achieve all-pass response is solved and are given by

$$k_2 = \frac{k_1}{2}, \tag{C.4}$$

$$k_{22} = k_{11}, \tag{C.5}$$

and

$$B_1 = B_2 = B_{11} = B_{22} = 0. \tag{C.6}$$

Inserting the conditions into (C.2) and (C.3), the transmission and reflection coefficients become

$$S_{21} = -\frac{s^2 + k_1^2 s + 2k_{11}^2}{s^2 - k_1^2 s + 2k_{11}^2}, \tag{C.7}$$

and

$$S_{11} = 0. \tag{C.8}$$

This is a second-order all-pass filter response.

The coupling matrix of a six-order triplet topology with θ_T equal to 90 degree and ideal resonators is given by

$$M = \begin{bmatrix} 0 & 0 & 1 & k_2 & 0 & 0 & 0 & 0 & 0 \\ 0 & B_1 & k_1 & 0 & k_{11} & 0 & 0 & 0 & 0 \\ 1 & k_1 & 0 & 0 & 0 & 0 & 0 & 0 & 1 \\ k_2 & 0 & 0 & B_2 & 0 & 0 & 0 & k_{22} & -k_2 \\ 0 & k_{11} & 0 & 0 & B_{11} & k_{21} & 0 & 0 & 0 \\ 0 & 0 & 0 & 0 & k_{21} & B_{21} & 0 & 0 & 0 \\ 0 & 0 & 0 & 0 & 0 & 0 & B_{22} & k_{12} & 0 \\ 0 & 0 & 0 & k_{12} & 0 & 0 & k_{22} & B_{12} & 0 \\ 0 & 0 & 1 & -k_2 & 0 & 0 & 0 & 0 & 0 \end{bmatrix} \tag{C.9}$$

The conditions to achieve all-pass response is solved and are given by

$$k_2 = \frac{k_1}{2}, \tag{C.10}$$

$$k_{12} = k_{11}, \tag{C.11}$$

$$k_{22} = k_{21}, \tag{C.12}$$

and

$$B_1 = B_2 = B_{11} = B_{12} = B_{21} = B_{22} = 0. \tag{C.13}$$

Inserting the conditions, the transmission and reflection coefficients become

$$S_{21} = -\frac{2s^3 - k_1^2 s^2 + (k_{11}^2 + k_{21}^2)s - k_1^2 k_{21}^2}{2s^3 + k_1^2 s^2 + (k_{11}^2 + k_{21}^2)s + k_1^2 k_{21}^2}, \tag{C.14}$$

and

$$S_{11} = 0. \tag{C.15}$$

This is a third-order all-pass filter response.

The conditions to achieve an all-pass response for an $(2Nth + 2)$-order triplet topology are given by

$$k_2 = \frac{k_1}{2}, k_{12} = k_{11}, k_{22} = k_{21}, ..., k_{N2} = k_{N1}, \tag{C.16}$$

and

$$B_1 = B_2 = B_{11} = B_{12} = B_{21} = B_{22} = ... = B_{N1} = B_{N2} = 0. \tag{C.17}$$

The all-pass response for several orders are calculated for validation

$$S_{21,2} = \frac{k_1^2 - 2s}{k_1^2 + 2s} \tag{C.18}$$

$$S_{21,4} = \frac{-2k_{11}^2 + (A_-)s}{+2k_{11}^2 + (A_+)s} \tag{C.19}$$

$$S_{21,6} = \frac{k_1^2 k_{21}^2 + (-2(k_{11}^2 + k_{21}^2) + (A_-)s)s}{k_1^2 k_{21}^2 + (+2(k_{11}^2 + k_{21}^2) + (A_+)s)s} \tag{C.20}$$

$$S_{21,8} = \frac{-2k_{11}^2 k_{31}^2 + (k_1^2(A_{23}) + (-2(A_{13}) + (A_-)s)s)s}{+2k_{11}^2 k_{31}^2 + (k_1^2(A_{23}) + (+2(A_{13}) + (A_+)s)s)s} \tag{C.21}$$

$$S_{21,10} = \frac{k_1^2 k_{21}^2 k_{41}^2 + (-2(C_{14}) + (k_1^2(A_{24}) + (-2(A_{14}) + (A_-)s)s)s)s}{k_1^2 k_{21}^2 k_{41}^2 + (+2(C_{14}) + (k_1^2(A_{24}) + (+2(A_{14}) + (A_+)s)s)s)s} \tag{C.22}$$

$$S_{21,12} = \frac{-2k_{11}^2 k_{31}^2 k_{51}^2 + (k_1^2(C_{25}) + (-2(C_{15}) + (k_1^2(A_{25}) + (-2(A_{15} + (A_-)s)s)s)s)s)s}{+2k_{11}^2 k_{31}^2 k_{51}^2 + (k_1^2(C_{25}) + (+2(C_{15}) + (k_1^2(A_{25}) + (+2(A_{15} + (A_-)s)s)s)s)s)s} \tag{C.23}$$

where

$$A_- = k_1^2 - 2s \qquad (C.24)$$

$$A_+ = k_1^2 + 2s \qquad (C.25)$$

$$A_{MN} = k_{M1}^2 + k_{(M+1)1}^2 + ... + k_{N1}^2 \qquad (C.26)$$

$$C_{MN} = k_{M1}^2 k_{(M+2)1}^2 + k_{M1}^2 k_{(M+3)1}^2 + ... + k_{M1}^2 k_{(N)1}^2 + k_{(M+1)1}^2 k_{(M+3)1}^2 + ... + k_{(N-2)1}^2 k_{N1}^2 \qquad (C.27)$$

The all-pass response with non-90 degree θ_T has not been derived.
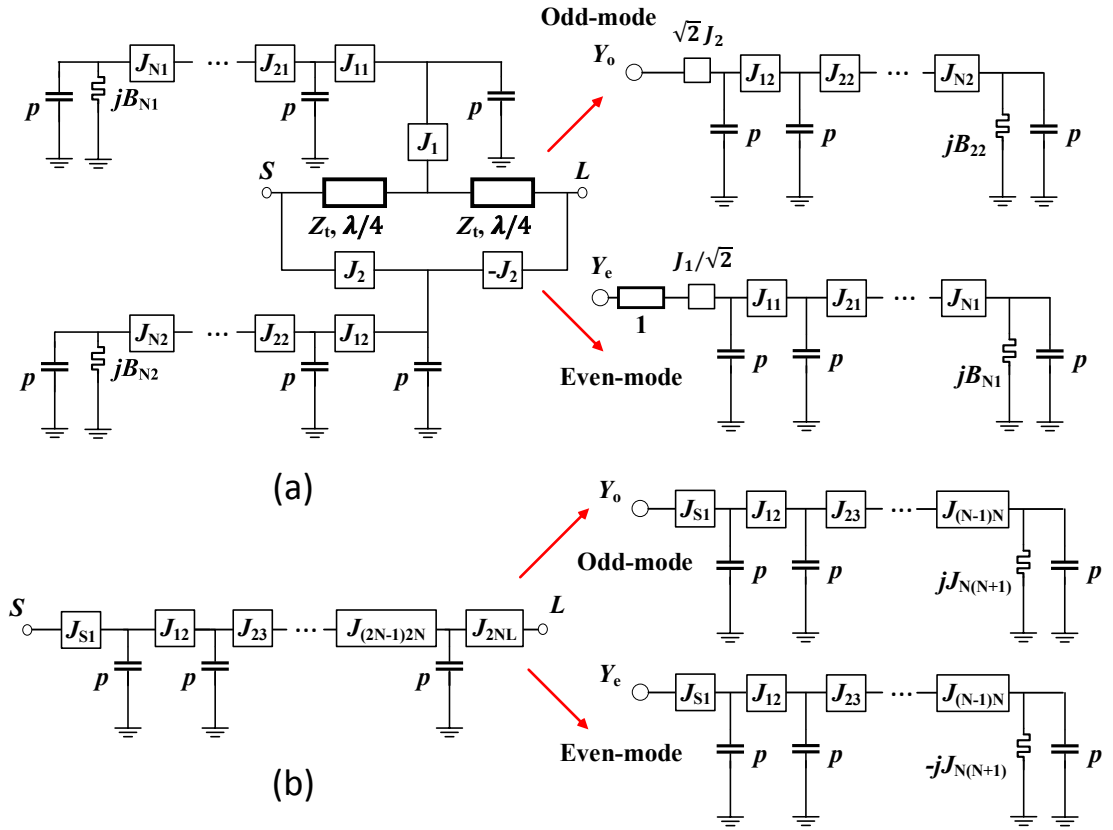

Fig. C.2. Coupling diagram of (a) the triplet absorptive bandstop-to-all-pass topology and (b) conventional bandpass topology. The even and odd modes of these two topologies are shown on the right.

C.2 Bandstop Synthesis

The conditions to achieve bandstop response with the same 90-degree θ_T is derived. In order to design a bandstop-to-all-pass filter, the conditions in (C.16 for all-pass response will apply in solving the bandstop response. It is easier to solve the bandstop response with the even- and odd-mode analysis because the topology naturally separates its even and odd modes (upper and lower branch). The even and odd modes for an arbitrary-order triplet topology are shown in Fig. C.2(a). The coefficients can be matched to obtain the reverted response of the bandpass topology [119]. The bandpass topology can be synthesized mathematically.

C.3 Fourth-Order Synthesis Example

The fourth-order Chebyshev bandstop response with -45-dB ripple is synthesized as an example. The synthesis stats with derivation of the transfer function. The ripple factor ε can be calculated with equation (B.22). Following that, the transmission coefficient square $(t(S)^2)$ can be calculated with equation (B.18). The roots in the left half of the phase-plane are used to configure the transmission coefficient $(t(S))$. The coupling coefficients are solved and summarized in Table. C.1.

Table C.1.
Summary of the coupling coefficients

Coupling	k_1	k_2	k_{11}	k_{22}	B_1	B_2	B_{11}	B_{22}
Bansdtop	2.3179	1.15895	1.82831	1.82831	0	0	1.2372	-1.2373
All-Pass	2.3179	1.15895	1.82831	1.82831	0	0	0	0

The all-pass response with finite Q_u of 300 and fractional bandwidth of 6% is plotted and shown in Fig. C.3.
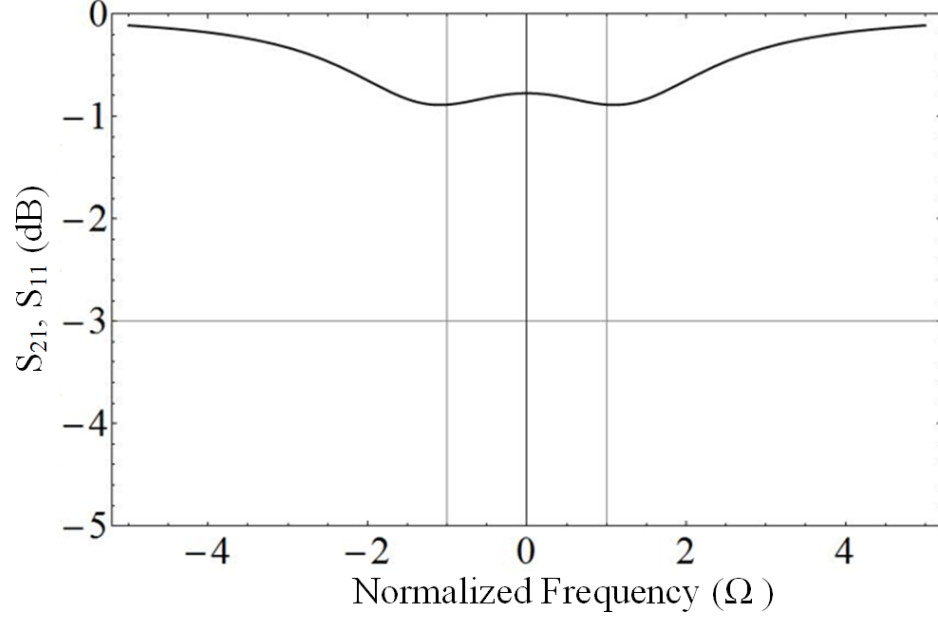
Fig. C.3. All-pass response of the bandstop-to-all-pass filter topology with finite Q-factor of 300 and fractional bandwidth of 6%.

The bandstop response of the filter with ideal resonators is plotted in Fig. C.4 from the synthesis. It is a fourth-order Chebyshev filter response with ripples at -45 dB.

Incorporating Q_u of 300 and fractional bandwidth of 6% into the coupling matrix, the insertion loss is simulated. The simulated bandstop response is shown in Fig. C.5. The insertion loss of the filter is less than 0.5 dB.
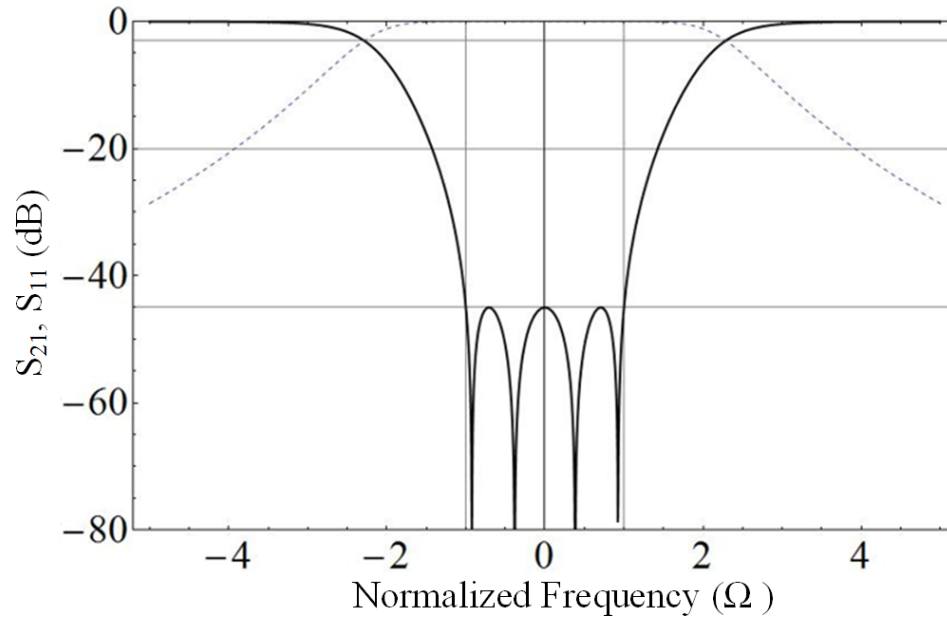
Fig. C.4. Chebyshev bandstop response of the fourth-order bandstop-to-all-pass filter topology.
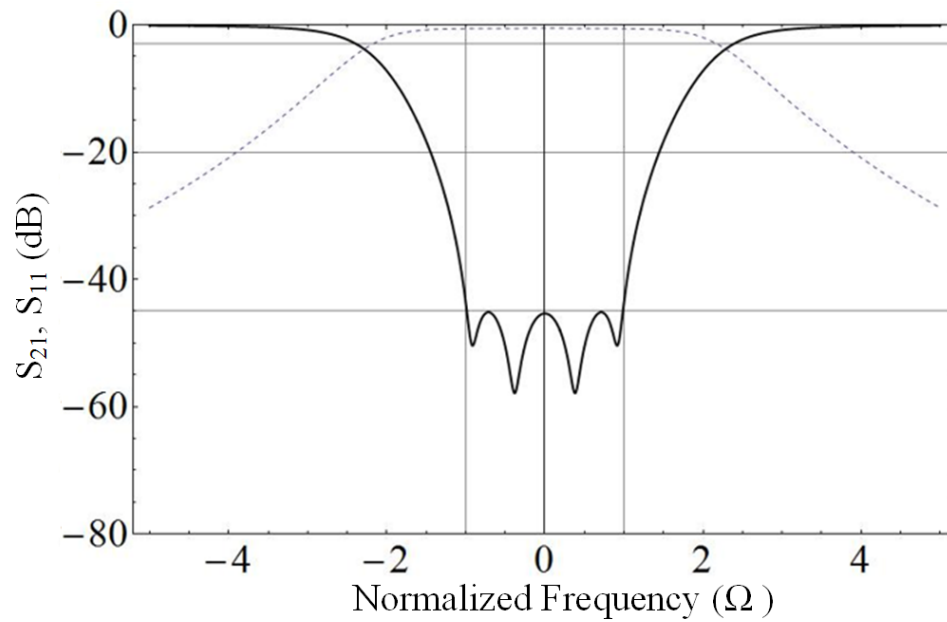

Fig. C.5. Chebyshev bandstop response of the fourth-order bandstop-to-all-pass filter topology with finite Q-factor of 300 and fractional bandwidth of 6%.

VITA

VITA

Wei Yang received the B.S.E.E degree from Purdue University, West Lafayette, in 2013, and is currently in pursue of the Ph.D. degree in electrical and computer engineering at Purdue University under the direction of Prof. Dimitrios Peroulis.

His research focuses are synthesis and control of highly-reconfigurable microwave and RF filters, with a special focus in absorptive bandstop filters.

Wei was the recipient of the third place awards in the tunable filter student design competition at the 2018 IEEE International Microwave Symposium.